Radionuclide Imaging of Angiogenesis

Neel Patel

St Hilda's College, University of Oxford



Hilary Term 2013

Submission for the degree of Doctor of Philosophy

ABSTRACT

Radionuclide Imaging of Angiogenesis
Neel Patel, St Hilda's College
Submitted for degree of DPhil, 2013

Angiogenesis is a fundamental process in the survival, growth and spread of cancers. In recent years several therapies have been developed to interfere with this process. Despite initial optimism these agents have rarely provided durable clinical responses. Methods capable of assessing angiogenesis are required to help develop effective anti-angiogenic approaches. Radionuclide imaging is one potential method of assessing angiogenesis. VEGF and integrin expression are two key factors in regulation of angiogenesis in tumours and provide potential targets for radionuclide imaging of angiogenesis. This thesis investigates whether targeting of VEGF and integrins can be performed to image angiogenesis and if treatment with antiangiogenic therapy can be detected viasuch imaging.

VEGF imaging was successfully performed by radiolabelling bevacizumab, a monoclonal antibody directed against all isoforms of VEGF, with ^{111}Indium for SPECT imaging. This agent was validated *in vitro* and *in vivo* mouse xenograft models, and appears to bind to matrix and cell membrane associated VEGF within tumours.

Integrin imaging was attempted using ^{99m}Tc-maraciclatide, another SPECT imaging agent. This is a commercial agent based on the RGD tripeptide sequence and binds primarily to $\alpha_v\beta_3$ and $\alpha_v\beta_5$ integrins. It was assessed in a clinical trial and compared with histological markers of angiogenesis in patients with colorectal, renal and breast tumours. There was an inverse relationship between 99mTc-maraciclatide uptake and β3 vascular density but no correlation with other angiogenic markers.

Both tracers were investigated in a preclinical xenograft model with antiangiogenic therapies. Rapamycin, an mTOR inhibitor, increased uptake of ^{111}In-bnDTPA-bevacizumab and decreased uptake of ^{99m}Tc-maraciclatide. These responses corresponded with an increase in VEGF and decrease in β_3 integrin levels in the tumours. Rapamycin therapy was also associated with reduction in blood vessel number and changes in perfusion as demonstrated by DCE-MRI. The effect of bevacizumab therapy on ^{99m}Tc-maraciclatide uptake was also investigated. Bevacizumab had no significant effect on either ^{99m}Tc-maraciclatide uptake or β_3 integrin levels.

These preliminary results demonstrate that both radiotracers have potential for imaging angiogenesis and detecting response to angiogenic therapies. They also highlight the complex nature of the angiogenic process and that further work is necessary to determine the clinical usefulness of these agents.

ACKNOWLEDGEMENTS

I am indebted to my supervisors, Fergus Gleeson, Adrian Harris and Katherine Vallis, for their mentorship, wisdom, encouragement and support. I am extremely grateful to them for giving me the opportunity to study for a DPhil and the pleasure of working with them. I would also like to thank Gillies McKenna for participating in my thesis committee and helping providing direction for the thesis.

The members of the Vallis lab are appreciated for their entertaining company and intellectual discourse. In particular, I would like to thank Sarah Able for her tireless work in optimising and performing the immunohistochemistry and western blots. Bart Cornelissen for his advice on radiolabelling techniques and statistics, and providing assistance with the ^{99m}Tc-maraciclatide preclinical experiments. Philip Waghorn was also instrumental in developing and performing the radio-HPLC for the project.

I am also grateful to the imaging core for their support in the preclinical imaging experiments. Danny Allen was invaluable in developing analytical techniques for the preclinical scans. He performed the automated vessel analysis and extracted the parameters from the DCE-MRI images. Stavros Meleminidis was a collaborator in the ^{99m}Tc-maraciclatide imaging study and helped perform and contour the DCE-MRI scans. Manos Fokas also helped in the preclinical experiments by assisting with confocal microscopy of tumour specimens.

Other members of the Gray Institute involved in the progression of this thesis were Michael Stratford, who helped optimise the preparation of rapamycin; and Kamila Hussien, who provided great support at the beginning and helped lay the ground work for the preclinical experiments.

I am also grateful to the members of the Harris lab who welcomed me and patiently taught me techniques required for my research. I am especially thankful for the guidance received from Helen Sheldon.

The ^{99m}Tc-maraciclatide clinical study protocol was originally written by Jo Brady and Richard Graham, and subsequently amended by me. For help in the study I would like to thank Carole Duncan and the other nuclear medicine radiographers for performing the scans. Naseer Khan and Carl Hopgood in the radiopharmacy prepared and provided quality assurance for the ^{99m}Tc-maraciclatide tracer. Joy Winter and members of the Oxford Research Biobank provided support by retrieving the tumour specimens and sectioning them for histological analysis. Michael Koukourakis and Alexandra Giatromanolaki at the University of Alexandria, Greece, optimised and undertook the histological analysis of the tumour samples. I would also like to acknowledge the help of the consultants and the research nurses in the colorectal, breast and urology teams in identifying patients for the study.

This research was supported by funding from the Oxford Cancer Imaging Centre (OCIC) grant, which is collaboration between Cancer Research UK (CRUK) and the Engineering and Physical Sciences Research Council (EPSRC).

CONTENTS

Abstract ii

Acknowledgements iii

Contents 1

Figures 4

Tables 6

Abbreviations 7

1 Introduction 11

1.1 Overview 12

1.2 Angiogenesis 12

1.2.1 Pathology and molecular processes 12

1.2.2 Response to therapy 14

1.2.3 Rationale for imaging angiogenesis 15

1.3 Targeted imaging methods 16

1.3.1 Modalities 16

1.3.2 Molecular Targets 17

1.4 Functional methods 23

1.4.1 Dynamic contrast enhanced-MRI 23

1.4.2 Positron Emission Tomography 26

1.5 Summary 27

1.6 Aim and hypotheses 27

2 Imaging of VEGF 28

2.1 Introduction 29

2.1.1 VEGF 29

2.1.2 Imaging VEGF 31

2.2 Aims 34

2.3 Materials and Methods 35

2.3.1 Synthesis of ^{111}In-labelled bevacizumab 35

2.3.2 Cell culture 38

2.3.3 *In vitro* experiments 39

2.3.4 *In-vivo* experiments 40

2.3.5 Tumour analysis 42

2.3.6 Statistics 45

2.4 Results 46

2.4.1 Synthesis 46
2.4.2 *In vitro* specificity 50
2.4.3 *In vivo* characteristics 51
2.5 Discussion 58
2.6 Conclusion 60
3 Clinical Validation of Integrin Imaging 61
3.1 Introduction 62
3.1.1 Integrins in Angiogenesis 62
3.1.2 RGD-based imaging agents 62
3.1.3 ^{99m}Tc-Maraciclatide (GE Healthcare) 64
3.2 Aims 67
3.3 Materials and Methods 68
3.3.1 Regulatory Approval 68
3.3.2 Recruitment Criteria 68
3.3.3 Patient Recruitment and Enrolment 68
3.3.4 Trial procedures 69
3.3.5 Surgery and histological analysis 70
3.3.6 Image Analysis 74
3.3.7 Statistics 76
3.4 Results 77
3.4.1 Patient demographics 77
3.4.2 Histology 77
3.4.3 Imaging characteristics 78
3.4.4 Tumour specific uptake 82
3.4.5 Comparison with angiogenic markers 83
3.5 Discussion 89
3.5.1 Imaging Characteristics 89
3.5.2 Correlation with angiogenic markers 91
3.6 Conclusion 93
4 Imaging Response to Antiangiogenic Therapy 94
4.1 Introduction 95
4.1.1 Imaging to predict response 95
4.1.2 Assessing antiangiogenic therapies 96
4.1.3 Summary 102

4.2 Aims 102
4.3 Materials and Methods 103
4.3.1 Cell culture and animal husbandry 103
4.3.2 Synthesis of ^{111}In-bnDTPA Bevacizumab 103
4.3.3 ^{99m}Tc-Maraciclatide preparation 103
4.3.4 Rapamycin preparation 104
4.3.5 ^{111}In-bnDTPA-Bevacizumab *in vivo* studies 104
4.3.6 ^{99m}Tc-maraciclatide *in vivo* studies 105
4.3.7 Tumour analysis 106
4.3.8 Statistics 110
4.4 Results 111
4.4.1 ^{111}In-bnDTPA-bevacizumab studies 111
4.4.2 ^{99m}Tc-maraciclatide studies 119
4.5 Discussion 124
4.5.2 Conclusion 128
5 Discussion 129
5.1 Introduction 130
5.2 Validation of Imaging Agents 131
5.2.1 ^{111}In-BnDTPA-Bevacizumab 131
5.2.2 ^{99m}Tc-maraciclatide 135
5.2.3 PET versus SPECT 137
5.3 Therapeutic response assessment 138
5.3.1 Future work 139
5.4 Summary 141
5.4.1 Conclusion 141
Appendix A: References 142
Appendix B: Clinical Trials 156
5.5 Maraciclatide Trial Protocol 156
5.6 VEGF Imaging with ^{111}In-bnDTPA-Bevacizumab 157
5.7 Fluciclatide, Pre and Post Therapy Study 159

FIGURES

Figure 1: Morphology of vessels from a normal organ vascular bed and tumour vessels 14
Figure 2: VEGF pathway receptors and ligands.. 18
Figure 3: Schematic of the members of the integrin family. 20
Figure 4: Integrin imaging.. 22
Figure 5: A 2 compartment model for DCE-MRI. 24
Figure 6: Chemical structures of cDTPA and bnDTPA 35
Figure 7: Spectrophotometer calibration. 36
Figure 8: Synthesis of ^{111}In-bnDTPA-bevacizumab 46
Figure 9: Stoichiometry of bnDTPA conjugation.. 47
Figure 10: Protein concentrations of G50 column eluates.. 47
Figure 11: HPLC demonstrating UV absorption characteristics at 280nm of components of ^{111}In-bnDTPA-bevacizumab manufacture 49
Figure 12: Radio-HPLC of ^{111}In-bnDTPA-bevacizumab.. 49
Figure 13: *In vitro* specificity of ^{111}In-BnDTPA-bevacizumab 50
Figure 14: Kinetics of uptake of ^{111}In-bnDTPA-bevacizumab. 51
Figure 15: Distribution of ^{111}In-bnDTPA-bevacizumab 52
Figure 16: Comparison of autoradiographs with IHC of bevacizumab. 53
Figure 17: Comparison of weight of tumour against uptake of ^{111}In-bnDTPA-bevacizumab 53
Figure 18: *In vivo* specificity of uptake of ^{111}In-bnDTPA-bevacizumab. 54
Figure 19: SPECT-CT of FaDu xenograft bearing mice injected with either ^{111}In-bnDTPA-bevacizumab or ^{111}In-bnDTPA-IgG1κ. 55
Figure 20: VEGF levels in xenografts 56
Figure 21: Comparison of VEGF levels with uptake of ^{111}In-bnDTPA-bevacizumab 57
Figure 22: Comparison of the distribution of VEGF, bevacizumab and ^{111}In in a FaDu xenograft section.. 57
Figure 23: Chemical structure of maraciclatide. 65
Figure 24: Distribution of ^{99m}Tc-maraciclatide with an excess of unlabelled maraciclatide.. 65
Figure 25: Process of calculating vascular survival ability (VSA) 73
Figure 26: Comparison of different methods of assessing ^{99m}Tc-maraciclatide uptake within tumours 74
Figure 27: Comparison of mean number of counts in muscle and fat with ^{99m}Tc-maraciclatide imaging 75
Figure 28: Examples of tumours imaged with ^{99m}Tc-maraciclatide. 79

Figure 29: Exemplar scans of patients with renal tumours imaged with ^{99m}Tc-maraciclatide. 80
Figure 30: Comparison of uptake of ^{99m}Tc-maraciclatide with tumour volume. 81
Figure 31: Uptake of ^{99m}Tc-maraciclatide in different tumour types. 81
Figure 32: Comparison of uptake of ^{99m}Tc-maraciclatide in tumours of different stage and grade.. 82
Figure 33: CD31 immunohistochemistry of colorectal tumours. 83
Figure 34: Comparison of ^{99m}Tc-maraciclatide uptake with CD31 vessel density (VD). 84
Figure 35: Comparison of VSA (**A**) and "Edvin" score (**B**) with uptake of ^{99m}Tc-maraciclatide. 84
Figure 36: Examples of pKDR staining of tumour sections. 85
Figure 37: Comparison of pKDR staining with ^{99m}Tc-maraciclatide uptake in tumours. 85
Figure 38: Examples of β_3 integrin staining in tumour sections. 86
Figure 39: Comparison of β3 integrin and CD31 VD. 87
Figure 40: Comparison of standard VD of β3 integrin and CD31 with pKDR. 87
Figure 41: Comparison of ^{99m}Tc-maraciclatide uptake with β3 integrin VD. 88
Figure 42 DCE-CT parameter maps showing response to therapy in a patient with a colorectal cancer. 98
Figure 43 An example of vessel analysis from CD31 immunohistochemistry images. 107
Figure 44 Growth curves of FaDu xenografts in mice treated with daily intraperitoneal rapamycin at different doses.. 111
Figure 45 Effects of rapamycin therapy on tumour vasculature.. 112
Figure 46: Changes of uptake of ^{111}In-bnDTPA-bevacizumab with increasing doses of rapamycin in FaDu xenografts.. 112
Figure 47: VEGF concentrations within tumours. 113
Figure 48: Western blots of VEGF isoforms in FaDu xenografts from mice treated with different doses of rapamycin. 113
Figure 49: Quantitative analysis of western blots of VEGF isoforms in FaDu xenografts from rapamycin treated mice.. 114
Figure 50: Growth rate of FaDu xenografts in mice treated with rapamycin. 114
Figure 51: Effect of rapamycin therapy on FaDu xenografts.. 115
Figure 52: Uptake changes of ^{111}In-bnDTPA-bevacizumab and ^{111}In-bnDTPA-IgGκ in FaDu xenografts treated with rapamycin 116
Figure 53: Changes in VEGF levels in FaDu xenografts with rapamycin therapy. 116
Figure 54: Changes in VEGF isoforms in FaDu tumours from mice treated with rapamycin.. 117
Figure 55: Quantitative analysis of western blots for VEGF isoforms. 118

Figure 56: Vessel changes of FaDu xenografts with rapamycin therapy. 118
Figure 57: Characteristics of ^{99m}Tc-maraciclatide uptake in FaDu xenografts 119
Figure 58: Vascular changes with antiangiogenic therapy. 120
Figure 59: Changes in uptake of ^{99m}Tc-maraciclatide in FaDu xenografts with either rapamycin or bevacizumab therapy 120
Figure 60: Changes in β3 integrin levels with antiangiogenic treatment. 121
Figure 61: ^{99m}Tc-maraciclatide in a FaDu xenograft bearing mouse. 122
Figure 62: DCE-MRI of FaDu xenografts 123
Figure 63 Rapamycin and inhibition of angiogenesis.. 124
Figure 64: Schematic of different antibody derived imaging agents 133
Figure 65: Spatial comparison between imaging and histology. 137
Figure 66: Fluciclatide trial. 140

TABLES

Table 1: Potential applications for angiogenesis imaging 15
Table 2: Calculation of “Edvin” score.....73
Table 3: Patients with colorectal cancer.....77
Table 4: Patients with breast cancer.....78
Table 5: Patients with renal tumours.....78

Abbreviations

ACTREC	Advanced Centre for Treatment, Research and Education in Cancer
AIF	arterial input function
AKT	protein kinase B
ANOVA	analysis of variance
APAAP	alkaline phosphatase/anti-alkaline phosphatase
ARSAC	Administration of Radioactive Substances Advisory Committee
ASPA	Animals Scientific Procedures Act
ATCC	American Type Culture Collection
AUC	area under curve
BF	blood flow
bFGF	basic fibroblast growth factor
Bis-Tris	[Bis (2-hydroxyethyl) imino-tris (hydroxymethyl) methane-HCl]
Bn-DTPA	2-(4-isothiocyanatobenzyl) DTPA
BSA	bovine serum albumin
BV	blood volume
ccRCC	clear cell renal cell carcinoma
cDTPA	cyclic DTPA anhydride
CPM	counts per minute
CRC	colorectal cancer
CRF	case report form
CT	computed tomography
CTA	clinical trials authorisation
CTIMP	clinical TIMP
DAB	diaminobenzidine
DARPin	designed ankyrin repeat protein
DCE-CT	dynamic contrast-enhanced CT
DCE-MRI	dynamic contrast-enhanced MRI
DCE-US	dynamic contrast-enhance US
DCIS	ductal carcinoma in-situ
DLL	delta-like ligand
DMEM	Dulbecco's minimum essential medium
DMSO	dimethyl sulfoxide
DSC-MRI	dynamic susceptibility contrast-enhanced MRI
DTPA	diethylene triamine pentaacetic acid
DTT	dithiothreitol
ECG	electrocardiogram
ECM	extracellular matrix
ECOG	eastern cooperative oncology group
EDTA	ethylenediaminetetraacetic acid
EDVIN	edge vs inner
EGF	epidermal growth factor
ELISA	enzyme-linked immunosorbent assay
EORTC	European Organisation for Research and Treatment of Cancer
FBS	foetal bovine serum
FCS	foetal calf serum
FDA	Food and Drug Administration
FDG	fluorodeoxyglucose
FFPE	formalin-fixed, paraffin-embedded
FGF	fibroblast growth factor

FKBP	FK506 binding protein
FLK	fetal liver kinase
FLT	fms like tyrosine kinase
FMS	feline McDonough sarcoma
FOV	field of view
GBM	glioblastoma multiforme
GCP	good clinical practice
GE	General Electric
GFR	glomelular filtration rate
GIST	gastrointestinal stromal tumour
GMP	good manufacturing practice
GUI	graphical user interface
HEPES	4-(2-hydroxyethyl)-1-piperazineethanesulfonic acid
HIF	hypoxia inducible factor
HRP	horseradish peroxidase
HPLC	high-performance liquid chromatography
HSP	heat shock protein
IAUGC	initial area under the gadolinium curve
IC_{50}	half maximal inhibitory concentration
IgG	immunoglobulin G
IHC	immunohistochemistry
IMP	investigational medicinal product
IP	intraperitoneal
ISH	in-situ hybridisation
ITLC	instant thin layer chromatography
IV	intravenous
IVC	individually ventilated cage
KDR	kinase insert domain protein receptor
K^{trans}	transfer coefficient
K_i	extraction fraction
LEHR	low energy high resolution
MDT	multidisciplinary team
MHRA	Medicines and Health Products Regulatory Agency
Min	minute
MIP	maximum intensity projection
MMP	matrix metalloproteinase
MOPS	4-morpholinepropanesulphonic acid
MRI	magnetic resonance imaging
mTOR	mammalian target of rapamycin
MVD	microvessel density
NCI	National Cancer Institute
NET	neuroendocrine tumour
NHS	National Health Service
NIfTI	Neuroimaging Informatics Technology Initiative
NIR	near infrared
NRP	neuropilin
NSCLC	non-small cell lung cancer
OCHRe	Oxford Centre for Histopathology Research
OCT	optimum cutting temperature
ORB	Oxford Research Biobank
ORH	Oxford Radcliffe Hospitals

OSEM	ordered subsets expectation maximisation
OUH	Oxford University Hospitals
pCT	perfusion CT
PBS	phosphate buffered saline
PD	pharmacodynamics
PDGF	platelet derived growth factor
PE	phycoerythrin
PECAM	platelet/endothelial cell adhesion molecule
PEG	polyethylene glycol
PET	positron emission tomography
PI3K	phosphoinositide 3-kinase
PK	pharmacokinetics
pKDR	phosphor KDR
PI	post-injection
PlGF	Placental growth factor
PS	permeability surface area product
PSMA	prostate specific membrane antigen
R&D	research and development
RECIST	response evaluation criteria in solid tumours
RCC	renal cell cancer
RGD	arginine-glycine-aspartate amino acid residues
RIPA	radio-immunoprecipitation assay
ROI	region of interest
RTK	receptor tyrosine kinase
RTP	room temperature and pressure
SD	standard deviation
SDS	sodium dodecyl sulphate
SOP	standard operating procedure
SPECT	single photon emission computed tomography
SUV	standardised uptake values
sVD	standard VD
T:B	tumour to background
TBS	tris buffered saline
TBST	TBS + 0.1% Tween
TBV	tissue blood volume
TE	echo time
T:F	tumour:fat
TGF	transforming growth factor
TIE	tyrosine kinase with immunoglobulin-like and EGF-like domains
TIFF	tagged image file format
TIMP	trial of IMP
TKI	tyrosine kinase inhibitor
T:M	tumour to muscle
TR	repetition time
Tris	tris(hydroxymethyl)aminomethane
TTP	time to peak
ULN	upper limit of normal
US	ultrasound
USA	United States of America
UV	ultraviolet
VD	vascular density

V_e	extracellular and extravascular space
VEGF	vascular endothelial growth factor
VEGFR	VEGF receptor
VOI	volume of interest
VPF	vascular permeability factor
VSA	vascular survival ability

1 Introduction

1.1 Overview

Angiogenesis is an integral part of tumour growth and invasion. This has led to the emergence of several antiangiogenic therapies and stimulated efforts to accurately evaluate the extent of angiogenesis before and in response to anticancer treatment. The most commonly used approach has been the assessment of new vessel formation in histological samples. However, it is becoming apparent that this is insufficient for a full understanding of tumour physiology and for *in vivo* guidance of cancer management. Imaging has the potential to provide non-invasive and repeatable assessment of the angiogenic process. Imaging approaches use a variety of modalities and are aimed at either assessment of the functional integrity of tumour vasculature or the molecular pathways involved in its regulation and response to therapy.

1.2 Angiogenesis

1.2.1 Pathology and molecular processes

Angiogenesis, the formation of new blood vessels from pre-existing blood vessels, is a fundamental aspect of the growth and spread of nearly all tumours. This process is distinct from vasculogenesis which generates blood vessels *de novo* and occurs primarily during embryogenesis [4]. Without angiogenesis most tumours would be unable to grow beyond a few millimetres in diameter, as they would exceed their nutritional needs. As the tumour grows, angiogenesis is initiated by microenvironmental stimuli such as hypoxia, which lead to a shift in the balance between pro and antiangiogenic factors [5]. This drive towards a pro-angiogenic environment is termed the "angiogenic switch" and is characterised by activation of blood vessel growth within the tumour. The switch, which may occur at any time within the natural history of a tumour, depends on numerous factors including tumour type and local environment.

Several determinants of the angiogenic process, after the switch has been triggered have been identified. The most intensely investigated are members of the vascular endothelial growth factor

(VEGF) family of receptors and growth factors. The interaction of VEGF (or $VEGF_A$) and the receptor, VEGFR-2, is particularly important as it leads to stimulation of endothelial cells, promoting their migration and proliferation [6]. In addition, VEGF (also known as vascular permeability factor (VPF)) has a direct effect on vessel permeability leading to leakage of macromolecules and raised interstitial pressures [7]. The level of VEGF expression has been shown to have prognostic significance in several tumour types [8]. Other molecular components of angiogenesis include integrins, which are involved in cell migration and invasion [9]; the notch-delta like ligand 4 (DLL4) pathway, which antagonises VEGF signalling; the fibroblast growth factor (FGF) family; platelet derived growth factor (PDGF); transforming growth factor-β (TGF-β); matrix metalloproteinases (MMPs); chemokines; and angiopoietins and TIE receptors [10]. These molecules are coordinated during the stages of angiogenesis from endothelial cell activation to degradation of the basement membrane, endothelial cell migration, vessel formation and remodelling.

Vessels formed as a result of angiogenesis are architecturally distinct from normal organ vessels. They lack the normal hierarchy of structure and are disorganised in shape (FIGURE 1). They display arteriovenous shunting, marked tortuosity and highly heterogeneous vascular density [11]. This heterogeneity is seen at all levels, from within individual tumour deposits to between different types of tumour. The vessels do not function normally, being fragile and leaky with inconsistent blood flow. These differences allow distinction between malignant and benign processes and can sometimes be exploited for imaging.

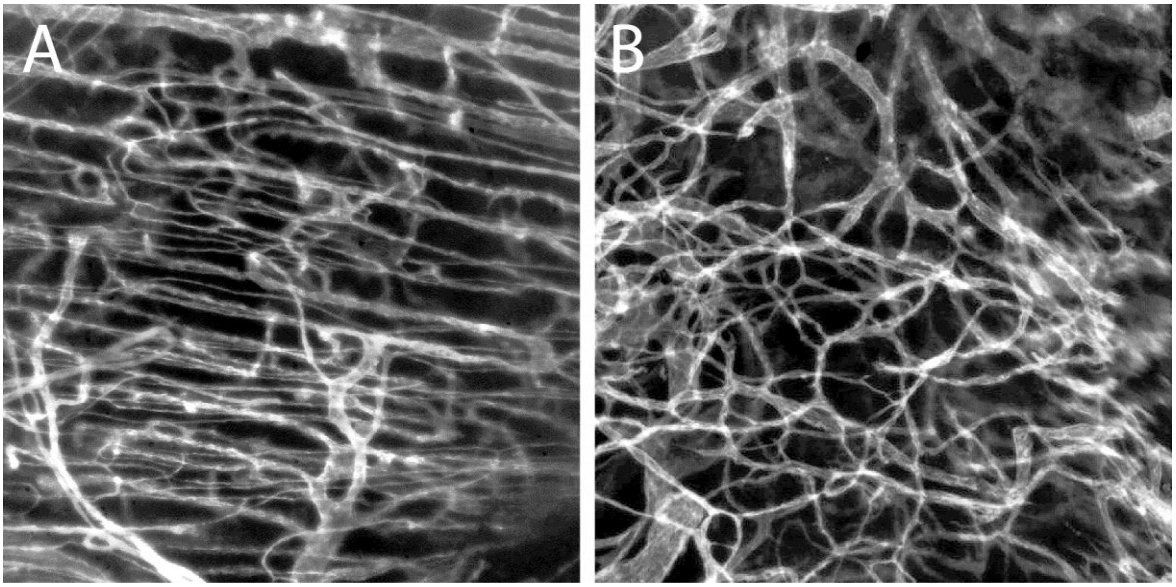


Figure 1: Morphology of vessels from a normal organ vascular bed (A) and tumour vessels (B), produced by confocal stacked images of CD31 immunohistochemistry. Tumour vessels are chaotic and disorganised

1.2.2 Response to therapy

As angiogenesis is so critical in tumour biology, much effort has been directed at developing treatments designed to perturb the process. So far only a few antiangiogenic therapies have entered routine clinical practice. Examples include bevacizumab, a monoclonal antibody against VEGF-A, and sunitinib and sorafenib, tyrosine kinase inhibitors that target VEGFR-2. Despite initial optimism these agents have rarely provided a durable clinical response. This may be because, unlike chemotherapy and radiotherapy, they are more likely to be cytostatic than cytocidal. Also anti-angiogenic therapies can induce structural, functional and molecular changes in tumour vessels that actually improve blood flow or "normalise" it [12]. It is also well documented that tumours may develop resistance to antiangiogenic therapies. The molecular mechanisms of resistance include upregulation of pro-angiogenic stromal cells and pathways [13]. In addition, there is some evidence from preclinical studies that the use of anti-angiogenic therapies may promote a more aggressive tumour phenotype by inducing hypoxia and selecting for more resistant tumour cells, though this has not been supported in clinical trials [14, 15].

1.2.3 Rationale for imaging angiogenesis

Evidently angiogenesis in tumours is a complex process with many unanswered questions regarding how to combat it for therapeutic gain. The conventional understanding of separate vascular and tumour compartments has also been questioned with observations that there are hierarchies of vessels in tumours with some responsive to VEGF and others that are not [16]. This has ramifications for combination and monotherapy especially in the context of progressive disease [17]. Methods capable of monitoring or assessing angiogenesis are needed for the development of effective antiangiogenic approaches. At present, assessment of tumour vascularity is performed through histological assessment of microvessel density (MVD). This invasive technique carries the inherent problem of sampling error and inconsistencies resulting from different staining and counting techniques [18]. In addition, MVD may not reflect the full biology of angiogenesis especially in cases of vasculogenic mimicry where tumour cells form vascular channels that conduct blood in the absence of endothelial cells [19].

Imaging techniques provide entirely new approaches to the assessment of angiogenesis (Table 1). The main advantages of *in vivo* imaging are that it is non-invasive, repeatable and can assess whole tumours and for some techniques their metastases. Strategies for imaging angiogenesis fall into two main categories: "Targeted" which interrogate molecular expression profiles in vessels; and "Functional" which investigate the structural changes within the vessels.

Table 1: Potential applications for angiogenesis imaging

Potential uses for Angiogenesis Imaging
Dose optimisation of a therapeutic drug
Optimising timing and duration of antiangiogenic therapies
Assessment of relapse/recurrence and resistance to antiangiogenic therapies
Patient risk stratification and selection for therapies
Direct management of patients e.g. combining antiangiogenic with either chemotherapy or radiotherapy
Translational research

1.3 Targeted imaging methods

Targeted methods enable interrogation of the molecular processes that underlie angiogenesis. This is particularly pertinent to the development of new treatments that target specific processes in tumour vasculature. Assessment of the status of these processes through imaging may allow improved prediction of therapeutic response. The basic approach involves injecting a molecular probe intravenously and allowing it to interact with its target. This target is usually a component of a molecular process such as a receptor or its ligand. The probe must contain some inherent contrast to distinguish it from its surroundings. The most commonly used molecular imaging modalities include positron emission tomography (PET), single photon emission tomography (SPECT), magnetic resonance imaging (MRI) and ultrasound (US). Optical imaging is also possible and is being developed clinically for guiding intraoperative detection of lymph nodes and metastases [20], although it is used mainly in preclinical research at present [21].

1.3.1 Modalities

1.3.1.1 Radionuclide imaging

Radiotracers are commonly used for molecular imaging and many are already being investigated in clinical trials. Their main advantage is that they are highly sensitive, with PET scanners able to detect even picomolar amounts of tracer [22]. At such low levels these compounds have little or no biological effect and therefore can be used to characterise molecular processes without causing physiological perturbations themselves. The main drawback of radionuclide imaging is its poor spatial resolution in comparison to CT and MRI. In addition, the poor availability of some radioisotopes and the specific radiochemical syntheses needed for some tracers can pose an obstacle to widespread use.

1.3.1.2 Molecular MRI

There are two main approaches to generation of contrast using MRI techniques. One method is akin to radionuclide techniques insofar as it involves the detection of a specific nuclide (e.g. ^{19}F, ^{2}H

or ^{13}C) incorporated into the imaging agent. This is a relatively insensitive method, which can be improved by several orders of magnitude, at least for ^{13}C nuclei, by hyperpolarisation [23]. The alternative method for generating contrast is to use agents that directly affect the proton MRI signal. Paramagnetic agents usually incorporate gadolinium (Gd) to yield contrast on T1-weighted images whereas superparamagnetic iron oxide (SPIO) particles are commonly used to generate negative signal on T2 and particularly T2*-weighted contrast. Signal can be increased by using large particles such as nanoparticles, polymers, liposomes and micelles to deliver a larger gadolinium or iron oxide payload. Despite such signal-amplification techniques MRI has very poor sensitivity, being able to detect agents in the micromolar range only. This has restricted the use of MRI as a molecular imaging modality and limited its use to preclinical applications.

1.3.2 Molecular Targets

Molecular targets for imaging angiogenesis include markers on endothelial cells (e.g. members of the VEGF pathway, integrins and cell adhesion molecules), non-endothelial cells (e.g. inflammatory cells and stem cells), matrix metalloproteinases (MMPs) and extracellular matrix (ECM) proteins. These may be present in relatively low abundance and sometimes inaccessible from the circulation (e.g. targets within the brain when there is an intact blood brain barrier). Furthermore vessels may occupy only a small proportion of the total tumour volume which may affect tracer uptake within tissues due to dependence on perfusion. Therefore, imaging can be challenging and binding to the targets should be highly specific and efficient, with rapid removal of any unbound target, to generate sufficient signal-to-noise for acceptable image quality.

1.3.2.1 VEGF Pathway

There are several growth factor pathways that are important for angiogenesis in cancer. Amongst these the VEGF pathway is one of the most extensively studied. The ligands are proteins coded by a family of genes that include VEGF A-D and placental growth factors (PlGF) [24]. These ligands interact with tyrosine kinase receptors including VEGF receptor 1 (VEGFR1) (also known as feline

McDonough sarcoma oncogene (fms)-like tyrosine kinase (Flt-1)); VEGFR2 (also known as kinase insert domain protein receptor (KDR) or fetal liver kinase 1 (Flk-1)); and VEGFR3 (also known as Flt-4) (FIGURE 2). VEGFR1 is expressed mainly on endothelial cells, macrophages and monocytes, whilst VEGFR2 is predominantly expressed on endothelial cells and VEGFR3 in lymph vessels. Each of these receptors operates as a monomer which dimerises upon ligand binding leading to activation of tyrosine kinase. This can lead to homodimers or heterodimers forming such as VEGFR1/2 [25] and VEGFR2/3 [26]. The VEGFRs also interact with co-receptors on the surface of cells such as heparan sulphate, heparan sulphate proteoglycans [27], neuropilins (NRPs) [28] and integrins [29].

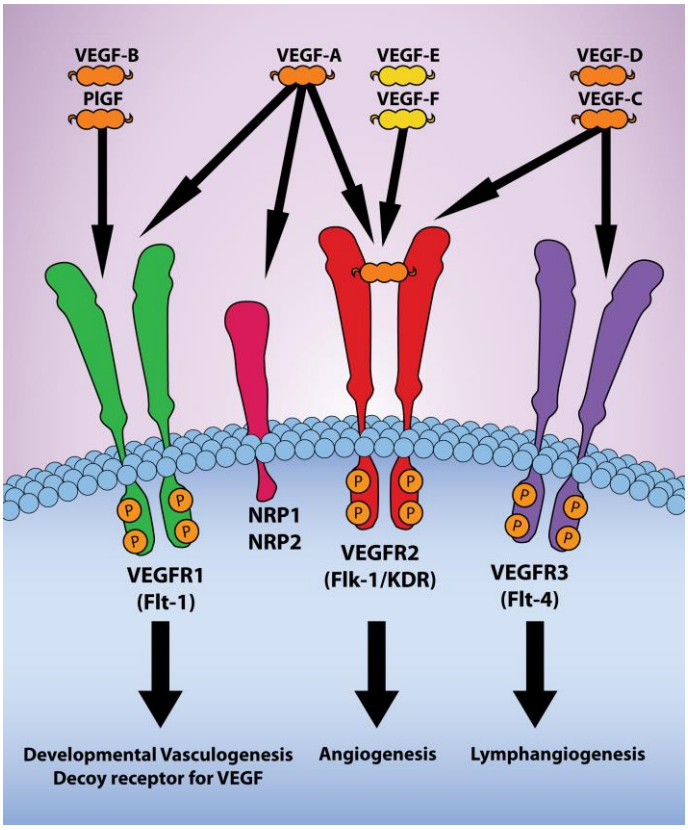


Figure 2: VEGF pathway receptors and ligands. Binding of ligand leads to homo or heterodimerisation of the receptor and phosphorylation of tyrosine residues in the intracellular domains. This leads to activation of several intracellular pathways. VEGFR1 and VEGFR2 are predominantly expressed on the surface of blood vessel endothelial cells, whereas VEGFR3 is mainly found on lymphatic endothelial cells. Neuropilin receptors (NRP 1 and 2) are co-receptors involved in enhancing VEGF binding to their receptors. VEGF-Es are derived from orf family paramyxoviruses and VEGF-Fs have been isolated from snake venoms.

VEGF (also known as VEGFA or vascular permeability factor (VPF)) plays a pivotal role in tumour angiogenesis. It binds to both VEGFR1 and VEGFR2 and their heterodimer, though has much

greater affinity for VEGFR1 in comparison with VEGFR2 [30]. Its action on VEGFR1 is to regulate a variety of physiological processes that are especially important in embryogenesis. VEGFR1 also has a soluble form (sVEGFR1) which antagonises the action of VEGF by sequestering it from binding to its receptors [31, 32]. VEGFR2 has a much more potent kinase activity than VEGFR1 [30] and is the major mediator of the angiogenic, mitogenic and vascular permeability enhancing effects of VEGF [33]. It is this pathway that is the main target for antiangiogenic therapies and therefore also a focus for angiogenesis imaging.

Approaches to imaging of the VEGF pathway can be divided into those that target VEGF itself and those that target its receptors. Numerous antibodies have been used to image VEGF. One of the earliest studies that demonstrated the feasibility of imaging VEGF within tumours used the VG76e antibody radiolabeled with ^{124}I and ^{125}I for PET and SPECT imaging respectively [34]. Since then a number of antibodies including bevacizumab have been investigated with both SPECT and PET radionuclides [35]. Further developments have included using tracers based on antibody fragments to improve the kinetics of uptake. One example is ^{89}Zr labelled ranibizumab (a Fab fragment of bevacizumab) which has been used to demonstrate response to sunitinib on PET imaging in a murine tumour xenograft model [36].

The most straightforward method for imaging VEGF receptors has been the use of radiolabelled VEGF. VEGF isoforms such as $VEGF_{121}$ and $VEGF_{165}$ have been used in this context. However $VEGF_{165}$ is considered less suitable because it is less soluble than $VEGF_{121}$ and is associated with non-specific binding due to its heparan-binding domains. VEGF-based tracers have incorporated several different PET and SPECT radionuclides and demonstrated specific uptake in xenograft models. They, however, do not differentiate between expression of VEGFR1 and VEGFR2. This is undesirable as VEGFR1 is significantly expressed within the kidney leading to high renal retention of the radiolabelled probe [37]. VEGFR1 is also considered less important for tumour angiogenesis than VEGFR2. Modification of the amino acid sequence of VEGF ($VEGF_{DEE}$) resulted in 20-fold

lower binding-affinity for VEGFR1 and only slight lowering of affinity for VEGFR2 [38]. Kidney uptake was significantly reduced when ^{64}Cu-VEGF$_{DEE}$ was compared to VEGF. Modifications to improve kinetics and binding affinity further have involved placement of the radiolabel at specific sites to prevent interference with binding [39] and the use of small peptides that bind VEGFR [40]. VEGFR has also been imaged by incorporation of targeting moieties into US contrast agents. For example, preclinical studies using VEGFR-targeted microbubbles to assess response to antiangiogenic therapies have shown promising results [41].

1.3.2.2 Integrins

Integrins are among the most extensively studied angiogenesis molecular targets. They are heterodimeric transmembrane receptors that play a role in cell migration, invasion and proliferation. They are expressed on tumour cells as well as associated host cells such as endothelial cells. They are composed of an α and a β subunit, combinations of which create 24 distinct sub-types (FIGURE 3). Of these $\alpha_v\beta_3$ is strongly expressed by tumour cells and on activated endothelial cells of angiogenic vessels but only weakly on mature blood vessels [42, 43]. $\alpha_v\beta_3$, together with several other integrins including $\alpha_v\beta_5$, recognises the tripeptide arginine-glycine-aspartate (RGD) which is present in several integrin binding partners in the ECM. This sequence forms the basis for imaging approaches that target integrins in angiogenesis.

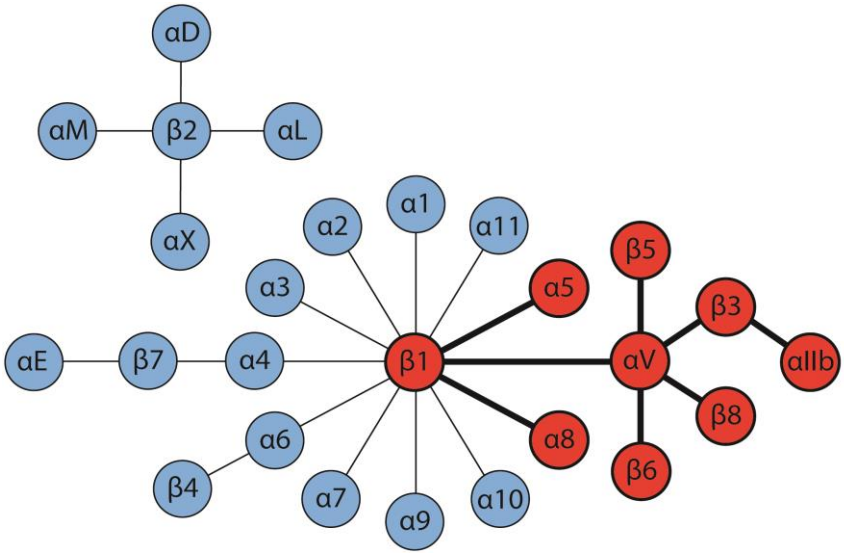


Figure 3: Schematic of the members of the integrin family. The RGD receptor subtypes are in red with thick lines

Early preclinical attempts to image integrins included the use of a monoclonal antibody (LM609) against $\alpha_v\beta_3$ that was conjugated to paramagnetic liposomes for MRI [44]. Despite good specificity, poor pharmacokinetics limited its subsequent use. More recent studies have used RGD peptide-based agents. Initially, radiolabelled cyclic peptide agents were used but hepatobiliary elimination led to high activity within the liver and bowel [45]. To remedy this several modifications have been tried such as conjugation with sugars (e.g. galactose or glucose), hydrophilic amino acids [46] and polyethylene glycol (PEG) [47]. Conjugation with sugars and amino acids shifts the elimination of the peptide to the kidneys. The effect of PEGylation on pharmacokinetics depends on the nature of the underlying structure and the size of the PEG chain but is improved overall. Further improvement in receptor binding affinity and pharmacokinetics have been achieved through the synthesis of multimeric RGD compounds, for which binding affinity increases with increasing number of monomeric subunits [48]. Another preclinical approach to integrin imaging is the use of nanoparticles that enable multimodality imaging [49].

So far only radionuclide RGD-based imaging agents have been investigated in clinical trials. The first and most extensively tested PET agent for angiogenesis detection is ^{18}[F]-galacto-RGD. It has been evaluated in several solid tumours providing good tumour-to-background ratios [50], showing uptake that correlates with MVD and intensity of immunohistochemical staining for $\alpha_v\beta_3$ [51]. Studies that compared ^{18}[F]-galacto-RGD to ^{18}[F]-FDG in non-small cell lung cancer (NSCLC) showed a lack of correlation between integrin expression and glucose metabolism [52]. These two tracers, therefore, yield different information regarding tumour physiology. Another PET agent in clinical trial is ^{18}[F]-fluciclatide (^{18}[F]-AH111585) (**FIGURE 4**) which has undergone preliminary safety testing [53] and is now in phase 2 trials. ^{18}[F]-fluciclatide is easier to synthesise than ^{18}[F]-galacto-RGD [54] and is commercially available (GE Healthcare). Other radionuclide-based imaging probes that have reached clinical trial include the SPECT agent ^{99m}[Tc]-

maraciclatide (^{99m}[Tc]-NC100692) [55]; and PET agents: ^{18}[F]-RGD-K5, an RGD molecule combined with plasminogen [56], and ^{18}[F]-FPPRGD2, a dimeric RGD molecule [57].

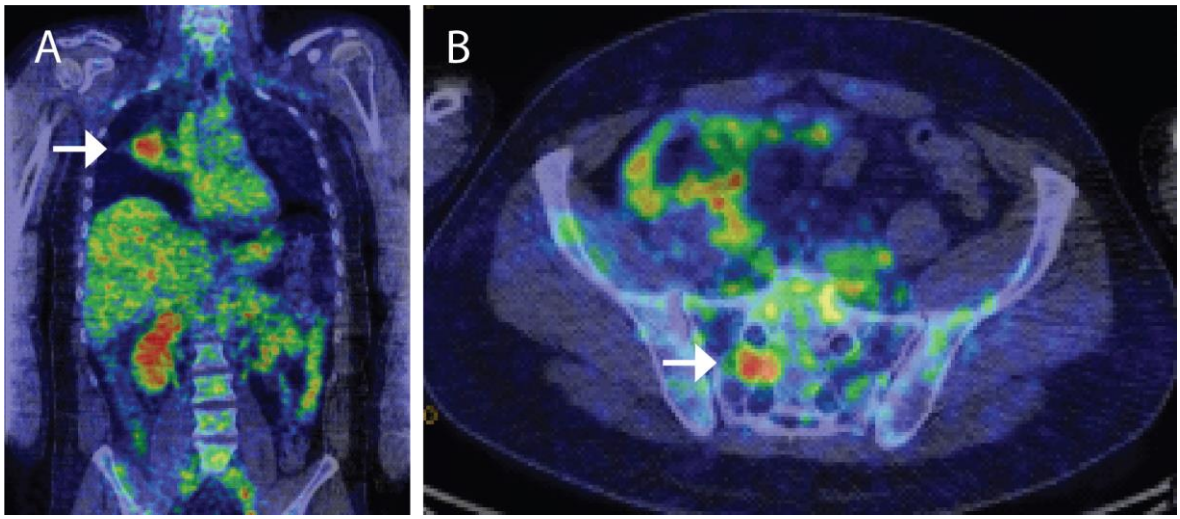


Figure 4: Integrin imaging. These are images of a patient with metastatic melanoma scanned with 18[F]-fluciclatide. Coronal PET-CT (**A**) demonstrating a right hilar metastasis. Another metastasis is also seen in the sacrum (**B**).

Much of the preclinical and clinical investigation of these SPECT and PET probes has involved validation of the tracers. Only recently have preclinical studies and clinical trials been undertaken to investigate the role that these agents might play in guiding management decisions. For example, in a recent report, ^{18}[F]-Fluciclatide was used to assess response to sunitinib in a glioblastoma xenograft tumour model. It was shown that uptake of tracer significantly decreased in the sunitinib treated group and that this was associated with decreased tumour MVD [58].

1.3.2.3 Other Targets

The VEGF pathway components and integrins represent only a few of the molecules involved in angiogenesis. Other potential biomarkers include: matrix metalloproteinases (MMPs), which promote tumour growth and angiogenesis by breaking down the physical barriers of the ECM and releasing proangiogenic factors such as VEGF and bFGF; ECM proteins such as fibronectins, which are expressed around the neovasculature of tumours and are almost undetectable in normal tissues; endoglin (CD105), a glycoprotein expressed on endothelial cells [59]; E-selectin, a cell adhesion molecule expressed on activated endothelial cells; Robo-4, a member of the

roundabout receptor family expressed on tumour endothelium; prostate specific membrane antigen (PSMA), a transmembrane protein expressed on the endothelium of most prostate tumours; angiopoietins/TIE receptors, which are involved in promoting maturation of new vessels; and CD276, which has been found to be overexpressed in tumour endothelium [60].

1.4 Functional methods

Functional imaging methods exploit the greater permeability and disorganisation of tumour versus normal blood vessels. Imaging techniques used to investigate angiogenesis generally use intravascular low molecular weight contrast agents. The extent and rate of leakage of these from tumour blood vessels depends on features of the tumour micro-environment including vascular permeability and surface area, blood flow and interstitial fluid pressure. For routine scanning performed to measure tumour size a single scan is sufficient. However, measuring the pharmacokinetic behaviour of the contrast agent through dynamic imaging may provide additional information. Unlike conventional imaging this involves scanning a region of interest (ROI) sequentially to record changes in contrast concentration over time. A curve of concentration versus time can be generated and from this, kinetic parameters that reflect different aspects of the vascular physiology can be extracted. Functional techniques can be performed by a variety of modalities including MRI, CT, ultrasound and PET. The most widely used is MRI which will be discussed below.

1.4.1 Dynamic contrast enhanced-MRI

MRI can be used to assess vascularity in several different ways. These include dynamic contrast-enhanced MRI (DCE-MRI), arterial spin-labelling (ASL) and dynamic susceptibility contrast enhanced MRI (DSC-MRI). Both DSC and DCE-MRI use gadolinium-based contrast agents. DSC-MRI uses T2* or susceptibility-based scanning which is more sensitive to the vascular phase of contrast delivery. DCE-MRI, on the other hand, uses T1-weighted imaging which is more sensitive

to contrast present within the extracellular space [61]. DCE-MRI has been extensively investigated for cancer imaging.

DCE-MRI is performed by injecting a gadolinium-based contrast agent intravenously and sequentially scanning the region of interest. The change in signal intensity on T1-weighted gradient-echo sequences is used to create a time versus enhancement curve. This can be analysed to extract parameters that are either semi-quantitative or quantitative. Quantitative parameters use a pharmacokinetic model for data-fitting. Most models used for DCE-MRI are a modification of the 2 compartment Toft's model [62] (FIGURE 5). This requires generation of a T1 map to enable calculation of the concentration of contrast agent within the ROI at each timepoint.

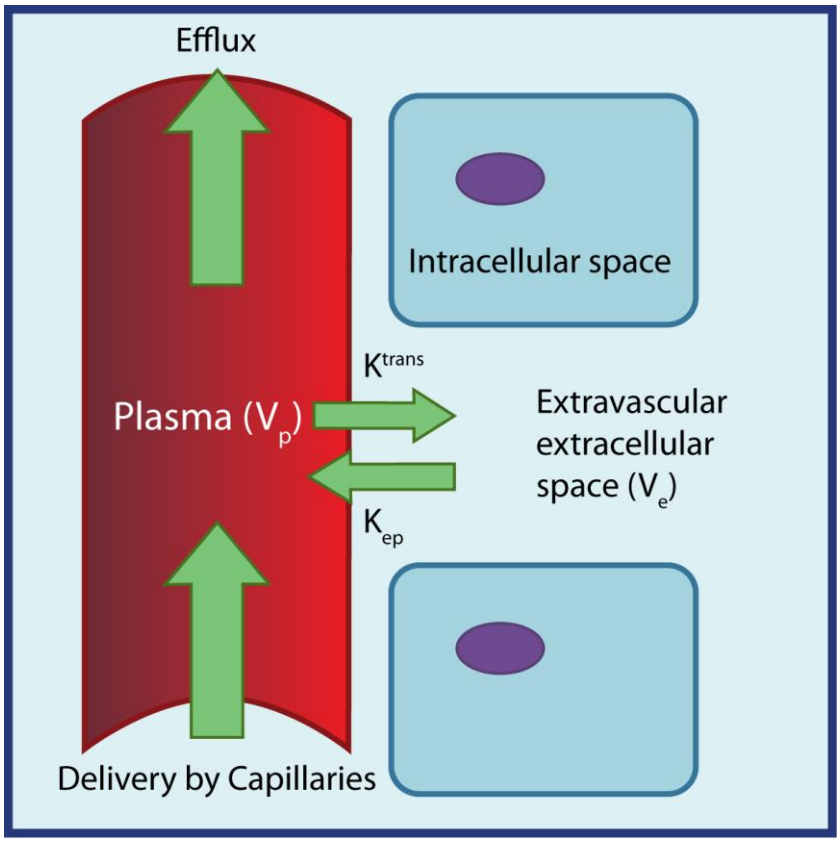


Figure 5: A 2 compartment model for DCE-MRI. Within an individual voxel contrast agent transfers from the plasma (V_p) in the capillaries into the extravascular extracellular compartment (V_e) at a rate described by the transfer constant K^{trans}. The rate of elimination from the compartment is described by K_{ep}. The contrast agents do not enter the intracellular compartment.

Parameters extracted from the models incorporate information on tissue blood flow, tissue (or tumour) blood volume (TBV), vessel permeability, extraction fraction and blood and interstitial volumes. K^{trans} is one of the most widely reported parameters in DCE-MRI and represents a combination of blood flow and vessel permeability. The relative contribution of each of these depends on which is the rate-limiting step. K^{trans} is also affected by the particular contrast medium used. For example, macromolecular contrast agents are associated with reduced leakage from vessels and decreased signal-to-noise ratio. This, however, is compensated for by an increased specificity for tumour vessels because of their larger pore size compared to vessels in other pathophysiological conditions [63].

Semi-quantitative parameters do not depend on the use of a model to describe the movement of contrast and are therefore straightforward to acquire. It is for these reasons that they are generally used in the non-research clinical setting. These parameters are a simple description of the shape of the enhancement curve and include slope of initial enhancement, time to peak (TTP), slope of the washout curve and initial area under the gadolinium contrast agent curve (IAUGC). Of these IAUGC, is the most useful and robust semi-quantitative parameter and has been shown to correlate well with K^{trans} to which it could be considered a practical alternative [64]. The disadvantage to most semi-quantitative methods is their marked dependence on scanning conditions such as injection rate and acquisition protocol. In addition, their output parameters do not directly reflect physiological processes.

DCE-MRI is already used in some clinical settings, particularly in aiding the detection of malignant tumours [65]. General clinical uses such as in breast, prostate and hepatocellular carcinoma tend to be semiquantitative and subjective in comparison to research settings where more quantitative measures are used. DCE-MRI has also been shown to predict response to therapy, with high K^{trans} values prior to therapy being predictive of clinical response [66].DCE-MRI has been widely used to monitor the effect of different treatments in several tumour types [67-69]. The

exception to this is radiotherapy where initially there are variable changes in enhancement parameters. DCE-MRI does, however, have a potential use in radiotherapy and that is to help guide treatment planning [70]. It has also been shown to have potential in guiding dosage and scheduling of antiangiogenic therapies. Reduction of IAUGC and K^{trans} has exhibited a linear dose-dependent relationship with drugs such as cediranib [71] and sorafenib [72].

1.4.2 Positron Emission Tomography

While PET is usually considered to be a molecular imaging tool, it can also be used for perfusion imaging. The two tracers relevant to tumour vascular imaging are $^{15}0$ water and ^{11}C carbon monoxide. $^{15}0$ water PET, is widely considered the gold standard for blood flow imaging [73], taking advantage of the free diffusibility of water to measure the perfusion of tumours. As the concentration of water has a linear relationship to the signal intensity, perfusion can be directly quantified. Analysis of the uptake curve can be performed either with Patlak analysis, which is a model-independent analysis technique, or with a 2-compartment model similar to DCE-MRI. ^{11}C carbon monoxide PET can be used to measure blood volume as CO binds to red blood cells in the circulation. This calculation requires knowledge of the subject's haematocrit.

Both tracers have been mainly validated in brain and cardiac imaging. They have been used in several clinical studies to evaluate response to cytotoxic and antiangiogenic therapies with inconsistent results [74, 75]. Both are very short-lived tracers so their use is limited to centres with an on-site cyclotron. ^{11}C carbon monoxide PET carries the additional complexity that it must be administered as a gas with associated logistical constraints.

1.5 Summary

Treatments directed against angiogenesis will play a key role in the future of cancer medicine. It follows that robust methods for real-time assessment of angiogenesis are required for effective clinical management and for the development of new antiangiogenic therapies.

Imaging of angiogenesis has been growing rapidly over the past few years. There are now multiple modalities with numerous techniques and imaging agents directed at accurately assessing angiogenesis. Of these, radionuclide imaging is likely to dominate as current MRI and US targeted agents lack sensitivity necessitating high administered doses and, therefore, further safety testing. Several PET and SPECT agents are already being tested in clinical trials. Of these the most promising are agents directed at imaging integrin and VEGF.

1.6 Aim and hypotheses

The aim of this project is to develop VEGF and integrin imaging agents that can be used to assess angiogenesis in tumours to ultimately guide patient management. The hypotheses for this project are:

1. VEGF specific imaging can be achieved using radiolabelled bevacizumab.
2. Integrin and VEGF radionuclide imaging are useful and correlate with other markers of angiogenesis.
3. Radionuclide angiogenesis imaging can be used to detect response to antiangiogenic therapy.

2 Imaging of VEGF

2.1 Introduction

One approach to investigate tumour angiogenesis is to assess the status of the VEGF pathway. This can be performed by measuring levels of VEGF pathway receptors (e.g. VEGFR2) or by measuring VEGF directly. This chapter examines the development of a radionuclide imaging probe to target VEGF and quantify its presence within tumour tissues.

2.1.1 VEGF

The major regulator of tumour angiogenesis is VEGF [76, 77], a homodimeric glycoprotein with a molecular weight of around 45kDa. It undergoes alternative splicing to produce several isoforms [78, 79]. The most prevalent are 121, 165, 189 and 206; defined by the number of amino acids they contain. $VEGF_{121}$ is acidic and freely diffusible, whereas the larger forms are more basic and bound to heparan and heparan proteoglycans on the surface of cells and ECM [80]. $VEGF_{165}$ is the predominant isoform and is found in both diffusible and bound forms. There is added complexity as each isoform may exhibit additional splice variation leading to a native and a "b" isoform, which antagonises the actions of the dominant form [81]. VEGF mediates most of its cancer angiogenic functions via VEGFR2 which is present on endothelial cells. It leads to endothelial cell activation, proliferation, survival, invasion and migration; and also markedly increases vascular permeability [77].

VEGF is regulated via a number of epigenetic factors such as hypoxia [82], low pH, inflammatory cytokines, sex hormones, chemokines and other growth factors. VEGF can also be upregulated due to loss of tumour suppressor genes (e.g. p53) and activation of oncogenes (e.g. Kras, Hras, Bcl-2) [83]. Of these, hypoxia is considered to be one of the most important. It mediates its effect via the hypoxia inducible factor (HIF) pathway, where activation of VEGF transcription is controlled by HIF-1 [84]. It has also been shown that hypoxia affects VEGF levels at a post-transcriptional level by increasing VEGF mRNA stability [85].

VEGF is involved in a number of pathological processes including neoplastic, ocular, inflammatory, vascular and ischaemic diseases. For tumour angiogenesis it is a central mediator stimulating growth of new blood vessels from nearby capillaries to supply tumours with nutrients. It protects the neovasculature of tumours by inhibiting apoptosis [86] and facilitates vessel growth by activating enzymes to degrade the ECM [87]. Its role in cancer extends beyond just angiogenesis. It has been shown to modulate the immune system to prevent efficient host anti-tumour response [88]. It also has a direct growth effect via paracrine and autocrine signals on tumour cells as they can express VEGFR1 and 2 [89-92]. In addition, VEGF may be involved in the systemic effects of cancers by directly impairing host organs such as the liver by causing hypoxia and increased vascular permeability [93].

VEGF is upregulated in many malignancies [94], with high levels in tumour tissue or the circulation associated with poor survival, and an elevated risk of recurrence and metastasis. This has been shown in several malignancies including gastric [95], colorectal [95, 96] and breast cancer [97]. Despite this, an elevated VEGF level in blood or tumour tissue does not generally predict response to treatment with drugs that target the VEGF pathway [98, 99], although it has been recently suggested that detection of the most diffusible isoform $VEGF_{121}$ may be helpful in this regard [100].

The role of VEGF within the pathogenesis of cancer is complex and there are many questions regarding its function that are still being investigated. It is currently unknown whether all metastases express the same level of VEGF; whether the VEGF levels in secondary tumours relates to that of the primary; whether different organs sites have variable levels of VEGF; and whether different tumour types have different levels of VEGF. In addition, it is not known whether inhibitors of VEGFR may paradoxically even induce VEGF through the induction of hypoxia, and thus cause resistance to treatment.

2.1.2 Imaging VEGF

Imaging VEGF provides a tool for non-invasively assessing the levels of VEGF within tumour deposits. It has the advantage over histological techniques in that it is not subject to sampling bias as it can visualise the whole tumour repeatedly over time. VEGF imaging has been attempted via several different approaches.

Indirect methods have focused on imaging the change in vascular permeability that VEGF confers. To investigate this, dynamic imaging modalities have been employed. DCE-MRI has provided conflicting results where kinetic parameters have been shown to correlate with VEGF expression in some tumours [98-100], but not in others [104, 105]. Similarly, pCT has led to inconsistent results, with varying correlation between perfusion parameters and VEGF expression [107-109].

Direct imaging of VEGF has predominantly involved targeted radionuclide techniques. Most approaches have used a radiolabelled antibody to bind to VEGF. One of the earliest studies that demonstrated the feasibility of imaging VEGF within tumours used the VG76e antibody radiolabelled with ^{124}I and ^{125}I for PET and SPECT imaging respectively [34]. Unfortunately iodination of the antibody interfered with its immunoreactivity, limiting its subsequent use. Another antibody previously used for VEGF imaging is HuMV833, a humanised version of the mouse monoclonal antibody MV833. A radioiodinated version (^{124}I) was used in a phase I clinical trial and demonstrated a wide range of PET uptake between tumour deposits in a variety of histological types [110].

Another anti-VEGF antibody previously used for imaging is sc507 (Santa Cruz). It has been used for optical imaging by conjugation with a fluorescent label (Alexa Fluor 488) [111] and MRI imaging by conjugation to dextran-coated iron oxide nanoparticles [112], to yield contrast on T2* and T2 weighted images within colorectal cancer xenografts. MRI has also been used with an anti-VEGF antibody bound to gadolinium-loaded nanoparticles to generate T1-weighted signal changes in a hepatocellular cancer xenograft model [113]. Furthermore, anti-VEGF magnetic

nanoparticles have been combined with a radionuclide (e.g. ^{131}I) to create a theranostic agent that can be used for both imaging and radioimmunotherapy to tumours [111].

2.1.2.1 Bevacizumab

The most popular antibody for imaging VEGF is bevacizumab (also known as rhuMAb-VEGF or Avastin (Roche)). It is a recombinant humanised [115] monoclonal immunoglobulin (IgG1κ) antibody (93% human and 7% murine) with a molecular weight of 149kDa. It binds to all isoforms of human VEGF with nanomolar affinity [116, 117] and inhibits the binding of VEGF to its receptors (VEGFR1 and VEGFR2). It has a 5 fold lower affinity for rabbit VEGF and no affinity for rat or mouse VEGF [118]. It is metabolised and eliminated via the reticuloendothelial system and has a biological half-life of 20 days (range 11-50 days) [119].

2.1.2.2 Therapeutic use

Bevacizumab is the first anti-VEGF monoclonal antibody to receive FDA approval (2004). It has displayed significant therapeutic activity in a broad range of tumour types *in vitro* and in xenograft models [120]. Subsequent phase I, II and III trials have demonstrated efficacy in several tumour types as either a monotherapy or in combination with chemotherapy [121-123]. Despite such results there are many questions to be answered regarding the use of bevacizumab especially with respect to its use in neoadjuvant and adjuvant settings; and dosing and duration of treatment. Furthermore, initial optimism has been tempered with significant side effects (e.g. hypertension, thromboembolic disease, gastrointestinal perforation, haemorrhage and congestive heart failure) demonstrated in phase III trials [124] and approval has been withdrawn by the FDA due to lack of evidence for improved survival in some tumour types, such as metastatic breast cancer [125].

2.1.2.3 Imaging with bevacizumab

Bevacizumab has been used as a VEGF imaging agent using a variety of modalities. It has been labelled with fluorophores for intraoperative near-infrared (NIR) imaging [126, 127] and has been

incorporated into multifunctional microbubbles for ultrasound imaging [125]. For PET imaging several radionuclides have been used, including ^{89}Zr [35, 126], ^{64}Cu [127], ^{86}Y [128] and ^{124}I [129]. One group has also created a dual modality agent which incorporates ^{64}Cu for PET imaging and a NIR fluorophore for optical imaging [133]. The majority of these imaging agents have thus far only been used in vitro and in murine xenograft models exhibiting varying degrees of uptake. At present there are only two bevacizumab-based imaging agent that have been used in clinical trials – 111In-bevacizumab, which will be discussed further, and 89Zr-bevacizumab which has been used in a recent clinical trial to investigate uptake in patients with breast cancer [134].

2.1.2.4 Indium

^{111}Indium (^{111}In) is a versatile radioactive metal that can be used as an iron analogue. It decays via electron capture releasing principally 173 and 247keV photons to form a daughter atom of ^{111}Cadmium. It has a half-life of 67 h which makes it practical for imaging multiple times over the course of a week, which is important for imaging antibodies which have long biological half-lives. ^{111}In is used in clinical SPECT imaging for a variety of indications. These include imaging of infection/inflammation using ^{111}In-oxine labelled leukocytes; imaging of neuroendocrine tumours (NETs) using labelled octreotide analogues; and detection of recurrent prostate cancer with a labelled antibody against prostate specific membrane antigen (PSMA) (capromab pentetide). As a result it is widely available and relatively inexpensive compared with other radionuclides.

2.1.2.5 Indium Bevacizumab

^{111}In bound to bevacizumab as a SPECT imaging agent was first reported in 2007, when it was compared to ^{89}Zr-bevacizumab in mice and shown to have similar uptake characteristics in normal organs and an implanted human ovarian tumour xenograft [35]. Subsequent studies have further investigated its pharmacokinetics, specificity and its relationship to VEGF expression and provided evidence for the specific binding of ^{111}In-bevacizumab to VEGF in both *in vitro* binding experiments and *in vivo* [135, 136]. ^{111}In-bevacizumab was first used in a clinical trial to image

liver metastases from colorectal cancer in 12 patients [137]. In the study, patients received intravenous ^{111}In-bevacizumab and imaging was performed after 7 days. The uptake in metastases was highly variable, ranging from none to very high. Unexpectedly, there was no correlation between uptake of tracer and the level of VEGF expressed in the tumours, measured using enzyme-linked immunosorbent assays (ELISAs) and in situ hybridisation (ISH). However, in a further study ^{111}In-bevacizumab was used to image 9 patients with stage III/IV melanoma [138]. This time a correlation was seen between uptake of the tracer in the tumours and IHC of VEGF in the resected tumour specimens. One possible explanation for these apparent inconsistencies may be that uptake of ^{111}In-bevacizumab is not influenced by secreted VEGF isoforms, such as $VEGF_{121}$. This was previously suggested by a study in which there was a lack of correlation between ^{111}In-bevacizumab uptake and $VEGF_{121}$ levels [136]

These reports highlight that VEGF imaging is in its infancy and needs to be developed to fully understand its implications and to further use it as a tool to investigate the biology of angiogenesis and to help guide patient management.

2.2 Aims

The aim of this study was to develop radiolabelled bevacizumab as a tool for imaging VEGF. The specific objectives covered within this chapter were:

1. To label bevacizumab with ^{111}Indium
2. To determine whether ^{111}Indium labelled bevacizumab binds to VEGF *in vitro*
3. To demonstrate radiolabelled bevacizumab has *in vivo* specificity for VEGF

2.3 Materials and Methods

Unless otherwise stated all chemicals were purchased from Sigma-Aldrich

2.3.1 Synthesis of ^{111}In-labelled bevacizumab

Bevacizumab (Roche) was radiolabelled by conjugation with diethylene triamine pentaacetic acid (DTPA). Two types of DTPA chelator were used: cyclic DTPA anhydride (cDTPA) and 2-(4-isothiocyanatobenzyl) DTPA (p-SCN-benzyl DTPA or bnDTPA) (Macrocyclics) (Figure 6). All procedures for conjugation were performed under strict metal-free conditions. This was achieved by using only glass or plastic equipment.

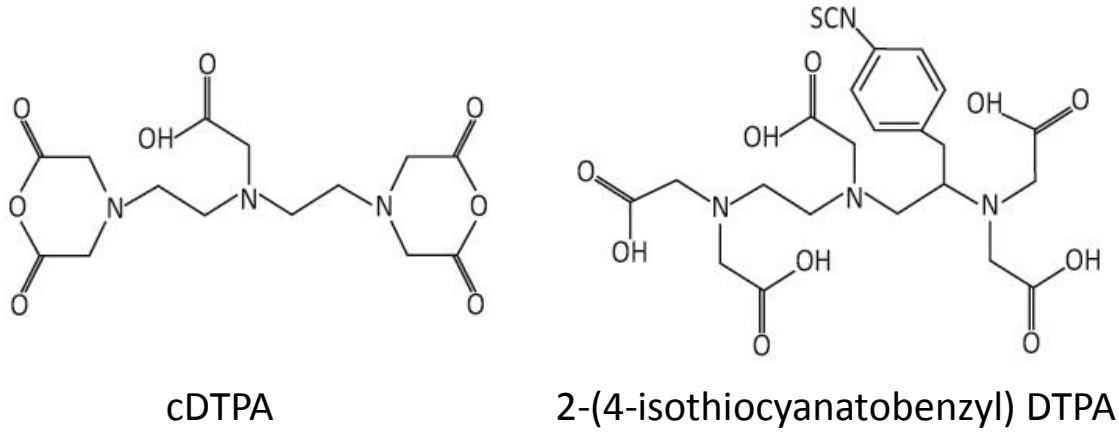


Figure 6: Chemical structures of cDTPA and bnDTPA

2.3.1.1 Bicarbonate buffer exchange

Stock bevacizumab was placed in a 30kD (YM30, Millipore) filter placed on top of a vial. Sodium bicarbonate ($NaHCO_3$; 0.1M, pH8.2) was added up to the brim and the vial was centrifuged at 13000g for 10min. The filter was then inverted and spun at 4000g for 4min to recover the bevacizumab.

2.3.1.2 DTPA conjugation

Dimethyl sulfoxide (DMSO; 3mls) was added to 3 mg of either cDTPA or bnDTPA (Macrocyclics) under dry conditions. An excess of the mixture was then added to bevacizumab and left for 45min at room temperature and pressure (RTP).

2.3.1.3 Protein purification

Purification of the DTPA-bevacizumab and free DTPA mixture was attempted by two purification techniques:

2.3.1.3.1 Gel-filtration chromatography

A pinch of glass wool was used to plug the tip of a glass Pasteur pipette. The column was then loaded with a Sephadex G-50 gel and irrigated with phosphate buffered saline (PBS), taking care not to get air bubbles trapped within the gel.

The conjugated DTPA-bevacizumab was loaded onto the Sephadex G-50 gel column. PBS (500 µl) was then added to the column and the eluate was discarded. PBS was added to the column in 50 µL amounts and the eluates were collected separately from the bottom of the column.

The amount of antibody in each aliquot was quantified by using a spectrophotometer (ND1000, Nanodrop). The spectrophotometer was first calibrated using a dilution series of standard protein (FIGURE 7). Sample concentrations were calculated by reading absorbance at 280 nm and using an absorbance coefficient of 1.5 mg/mL (slope of graph). The aliquot containing the peak concentration of antibody was identified and combined with all the aliquots preceding it, to produce the final solution of purified antibody.

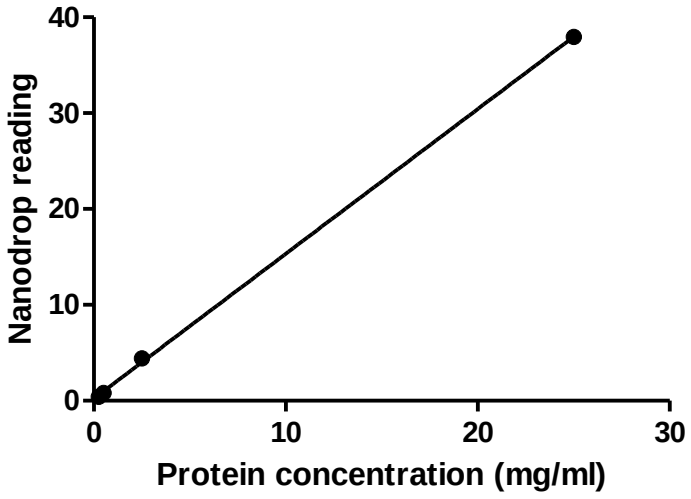


Figure 7: Spectrophotometer calibration. Slope of regression line=1.5, r^2=0.9998, P<0.0001

2.3.1.3.2 Protein A column purification

Purification of antibody was performed using a Pierce Chromatography Cartridge Protein A/G (Thermo scientific) and following the manufacturer's procedure for purification using a syringe. All components and buffers were equilibrated at room temperature. 5-10 column volumes of binding buffer (100 mM sodium phosphate, 150 mM sodium chloride, pH 7.2) were passed through the column. The DTPA-bevacizumab solution was then passed over the column after which the column was washed with the binding buffer. The antibody was then eluted with elution buffer (0.1 M glycine, pH 2-3). The eluate was adjusted to physiological pH by adding 100 µL TRIS (1 M, pH 7.5-9) to 1 mL of eluate.

The protein concentration of the eluate was measured using a spectrophotometer as described above.

2.3.1.4 Citrate buffer exchange

The purified DTPA-bevacizumab solution was buffer exchanged (as for the bicarbonate buffer exchange) using 0.1 M, pH 5.0 citrate.

2.3.1.5 Radiolabelling

10-20 MBq ^{111}indium chloride ($^{111}InCl_3$) (Perkin-Elmer) was added to the DTPA-bevacizumab solution and incubated at RTP.

2.3.1.6 Instant thin layer chromatography (ITLC)

The ^{111}In bevacizumab solution was diluted to 1000 nM with PBS. 1 µL was placed on a 5x100 mm strip of ITLC paper (Pall Lifesciences) 15 mm from one end. The ITLC paper was then placed in a 15 mL tube containing 0.8 mL 0.1M pH 5.0 citrate buffer. Once the liquid had risen to the top of the ITLC paper it was cut into half. Each half (designated as either 'top' or 'bottom') was placed into a separate gamma-counting tube. The strips were counted for 60 sec in an automated gamma-counter (Perkin-Elmer) using a protocol normalised for ^{111}In. Binding efficiency was calculated by using the following equation: $(Bottom)/(Top + Bottom) \times 100$.

ITLC was performed every time bevacizumab was labelled with ^{111}In to confirm the radiochemical purity of the tracer.

2.3.1.7 High-Performance Liquid Chromatography (HPLC)

HPLC was performed using a Waters 2695 Separation Module with a 2489 UV/Vis Detector and e-SAT/IN module. An isocratic run was performed for 30 minutes with 20 µL sample loaded on a Bio-Sep-SEC-C 2000 (300x7.8 mm) column at a flow rate of 0.7 mL/min in a buffer composed of 0.1 M Na_2SO_4 and 0.1M Na_2HPO_4 (pH 7.0). The wavelength of detection for the UV trace was set at 280 nm and 254 nm.

HPLC runs were performed by Philip Waghorn

2.3.2 Cell culture

2.3.2.1 Cell lines

MDA-MB-231 (human breast adenocarcinoma) cell lines were provided by Dr Helen Sheldon (Weatherall Institute of Molecular Imaging). The cell lines were selected from clones infected with a retrovirus to express VEGF: 2F11 (244.7 pg/mg protein as determined by ELISA) and IE3 (3.6 pg/mg protein).

FaDu (human head and neck squamous cell carcinoma), LS 174T (human colorectal adenocarcinoma) and 786-O (human renal adenocarcinoma) cell lines were obtained from the American Type Culture Collection (ATCC). These cell lines were chosen as they were known to have sufficient expression of VEGF for the experiments. The FaDu cell line was also picked for its consistent and steady growth rate *in vivo*.

2.3.2.2 Culture conditions

All cell lines were grown as a monolayer in Dulbecco's minimum essential medium (DMEM) supplemented with 10% heat-inactivated foetal bovine serum (FBS) (Gibco), L-glutamine (20 mM) penicillin G (100 u/mL) and streptomycin (100 mg/mL). They were cultured at 37^{o}C in a 5% CO_2

humidified atmosphere and grown to 80% confluence, after which, they were washed twice with PBS, covered with 4 mL 1% trypsin-EDTA (Gibco) and left in an incubator for 7 min. The trypsin was inactivated by the addition of 6 mL of growth medium and then the cells were triturated. The remaining cell solution was either split into culture flasks or spun (1000g for 5 min) and frozen down at -80^{o}C in cryovials with 10% DMSO and then transferred to liquid nitrogen storage after 24 hours.

2.3.2.3 Cell recovery

Cells frozen in cryovials were thawed in a water bath and transferred to a flask containing pre-warmed culture medium.

2.3.2.4 Cell counting

Cells were suspended in medium as described above. The number of cells within the solution was determined using an automated cell counter (Nucleocounter, ChemoMetec) as per the manufacturer's instructions.

2.3.3 *IN VITRO* EXPERIMENTS

2.3.3.1 Competitive binding assay

MDA-MB-231 2F11 cells (2 x 10^{5}) were seeded into each well of 24-well plates with DMEM and 10% FBS to give a final volume of 500 µL. The wells were left overnight and incubated at 37^{o}C. After 24 h the medium was removed and the wells were washed twice with 500 µL PBS. ^{111}In-BnDTPA-bevacizumab was prepared as described above and diluted to a final concentration of 1000 nM using PBS. Bevacizumab was added to each well in triplicate in a concentration range of 0.01 nM to 1000 nM plus 1 nM of ^{111}In-BnDTPA-bevacizumab. The plates were gently shaken to ensure complete mixing. They were then incubated in a fridge at 4^{o}C for 2 h. The supernatant was then removed from the wells followed by washing twice with 500 µL of PBS. Sodium hydroxide (250 µL, 0.1 M) was added to the wells and incubated for 30 min at RTP. Another 250 µL of PBS

was added to the wells and pipetted up and down once followed by removal of the lysed cells and transfer to 5 mL test-tubes. The wells were washed twice with PBS and the solutions were added to the same 5 mL test tubes. The test tubes were counted for 60 sec in an automated gamma-counter (Wizard, Perkin Elmer) using a protocol normalised for ^{111}Indium and corrected for decay.

2.3.4 *IN-VIVO* EXPERIMENTS

All *in vivo* experiments used a minimum of 4 mice per experimental group. BnDTPA-bevacizumab was conjugated the day before experiments, stored overnight at 4^{o}c, and radiolabelled on the morning of use.

2.3.4.1 Animal welfare

Animal studies were performed in accordance with the Animals Scientific Procedures Act (ASPA) of 1986 (UK). Female BALB/c nude mice (Charles Rivers) were used in all experiments as they lack a thymus gland which renders them immunodeficient, hence suitable for implantation of xenografts. They were housed in individually ventilated cages (IVCs) at 21^{o}c with 12 h light/dark cycles and food and water available *ad lib* during experiments. Mice were used in experiments when they were >15 g in weight and between 8-10 weeks old. All mice were monitored closely for any adverse effects during the course of an experiment and were euthanised if their condition became poor. All animals were euthanised after experiments by Schedule one methods.

2.3.4.2 Anaesthesia

Anaesthesia in the experiments was induced and maintained using a mixture of isofluorane (Baxter) and room air. Whilst under anaesthetic mice were monitored for respiration rate (maintained at 60-100 respirations/min) and temperature (maintained at 37^{o}c). After the experiment, mice were either euthanised or recovered in isolation and monitored for 20 min to ensure recovery from anaesthesia and experimental procedures.

2.3.4.3 Tumour inoculations

Tumour cells were put in suspension as described previously and centrifuged at 1000g for 5 minutes. They were then resuspended in DMEM (serum free) and counted and then further diluted in DMEM to give a final concentration appropriate for inoculation. For LS 174T and 786-O cells, 50 µL of cell suspension (4 x 10^6 cells) was mixed with 50 µL of Matrigel (BD Lifesciences) and constantly agitated to ensure no cell clumping occurred. For FaDu cells, 100 µL of suspended cells (1 million) were used. Mice were anaesthetised and the cell suspension was injected subcutaneously into the flank of each mouse.

2.3.4.4 Kinetics of uptake

Mice were inoculated with LS 174T tumours. Once the tumours reached 8 mm in diameter, ^{111}In-bnDTPA-bevacizumab (5 MBq of 3 µg) was administered to mice intravenously (IV) via a tail-vein. Mice were then euthanised on day 1, 3, 5 or 7 post-injection. Animals were euthanised and organs and tumour were harvested. The organs and tumour were weighed and radioactivity was measured using a gamma-counter. From this the presence of tracer within each tissue was calculated as a percentage of injected dose per gram of tissue (%ID/g) after correcting for radioactive decay:

$$\%ID/g = \frac{activity_{tissue}}{weight_{tissue} \times activity_{injected}} \times 100$$

2.3.4.5 Biodistribution

Mice were inoculated with LS 174T, 786-0 or FaDu cells. Once tumours grew to around 8 mm in diameter, the mice were injected via tail-vein injection with 5 MBq of 3 µg ^{111}In-bnDTPA-bevacizumab. On day 5 post-injection, the animals were euthanised and the distribution of tracer in the organs and tissues (blood, muscle, skin, stomach, bowel, fat, spleen, tail, liver, kidneys, heart and lungs) was determined as described above.

2.3.4.6 SPECT-CT imaging

SPECT-CT imaging was performed using a nanoSPECT/CT system (Bioscan) equipped with parallel pinhole collimators. Mice were anaesthetised and placed within a dedicated cradle within the scanner. SPECT was performed using 9x1 mm pinhole apertures; 100,000 counts/projection; 24 projections and a pitch of 1.5.

2.3.4.7 Specificity

Mice were inoculated with MDA-MB231, LS174T, 786-0 or FaDu cells. Once tumours grew up to around 8 mm in diameter, the mice were injected via tail-vein injection with 5 MBq of either 3 µg ^{111}In-bnDTPA-bevacizumab; or an isotype-matched, ^{111}Indium-labelled, non-specific antibody* (^{111}In-bnDTPA-IgG1κ (Southern Biotech)); or ^{111}In-bnDTPA-bevacizumab plus a hundred fold (300 µg) excess of cold bevacizumab. Animals were euthanised on day 5 with organs and tumour excised to determine uptake of tracer. After gamma counting the tumours were cut in half, frozen in liquid nitrogen and stored at -80^{o}c until further use. One half was saved for protein analysis and the other half was used for histological analysis.

*^{111}In-bnDTPA-IgG1κ was synthesised in exactly the same manner as ^{111}In-bnDTPA-bevacizumab as described above.

2.3.5 Tumour analysis

2.3.5.1 Sectioning

Tumours were embedded in optimum cutting temperature (OCT) (Tissue-Tek) compound and placed on a cryostat (OTF 5000, Bright) stage, sectioned (8 µm) and transferred onto a microscopy slide (Superfrost plus, VWR). Slides were stored at -80^{o}C.

2.3.5.2 Autoradiography

Autoradiography was performed on tumour sections the day after they had been excised. Slides of tumour sections were placed in an autoradiography cassette face up. High resolution

autoradiography film (Super resolution, Perkin Elmer) was placed on top of the slides with cling-film in between. The cassette was closed and left for 24 h in a freezer at -20°c. The film was then removed and scanned in a storage phosphor-imager (Cyclone Plus, Perkin Elmer) to generate autoradiographs of the tumour sections.

2.3.5.3 Immunohistochemistry (IHC)

Slides were removed from the freezer and allowed to equilibrate to room temperature. They were then fixed in ice-cold acetone for 10 min and dried for 20 min at room temperature. This was followed by washing in TRIS buffered saline (TBS) (50mM Tris, 150mM, pH7.6 NaCl) for 5 min and then TBS with 0.025% Triton for another 5 min. The slides were then blocked for 2 h at room temperature with a TBS, 1% BSA and 10% goat serum solution. Primary antibodies were diluted with TBS, 1% BSA then applied to the sections and left at 4°C and left in a humid chamber. Primary antibodies were either anti-VEGF (ab46154, Abcam) (1:30 dilution, 20 µg/mL) or Cy5 donkey anti-IgG (709-176-149, Jackson Laboratories) (1:500 dilution). After 24 h the slides were washed twice for 5 min in TBS, 0.025% Triton solution and then incubated with a secondary antibody (Alexa 488 goat anti-rabbit, Invitrogen) (1:500 dilution) for 1 h at room temperature in a humid chamber. They were then washed twice for 5 min in TBS and mounted in Vectashield containing DAPI (H-1200, Vector Laboratories). Negative controls were performed with omission of the primary antibody.

Slides were analysed using a confocal immunofluorescence microscope (LSM710, Zeiss). Whole tumour section images were performed using a x10 objective and tile-scan function on the microscope.

IHC and microscopy were performed by Sarah Able.

2.3.5.4 Tumour homogenisation

Tumour samples were crushed into a powder using a pestle and mortar filled with liquid nitrogen. The powder was then transferred to a 50 mL Falcon tube on ice. Homogenising buffer (EDTA 1.5

mM, HEPES 20 mM, one protease inhibitor tablet (complete mini, Roche) per 10 mL, pH 7.5) at 0.02 mL/mg was added to the powder. The solution was then homogenised using a tissue homogeniser at 5 sec bursts interspaced by 5 sec rests. The resultant suspension was centrifuged at 4^{o}c for 10 min at 3000g. The supernatant was pipetted off and then ultracentrifuged at 4^{o}c for 40 min at 225000g. The final supernatant was then pipetted off, split into aliquots and stored at -80^{o}c for further use.

2.3.5.5 Conditioned media preparation

Cells (3 x 10^{5}) were seeded into each well of a 6-well plate using the growth medium described above. After 24 h the medium was replaced with medium containing only 1% FCS. After 48 h the medium was drawn off and passed through a 0.22 µm filter (Millex, Millipore), then split into aliquots and stored at -80^{o}c for further use. For determining whether there is inhibition of binding of VEGF to ELISA plates in the 786-O cell line, equal volumes of LS 174T conditioned media and 786-O conditioned media were mixed together after thawing. A control was prepared by mixing equal volumes of LS 174T media and unconditioned media. The 2 mixtures were then used in the ELISA and protein assays described below.

2.3.5.6 Protein concentration

Protein concentration in the tumour samples was estimated following the manufacturer's protocol for the Biorad DC colorimetric assay. The assay involves adding 5 µL of tumour sample or standard protein solution (0-2 mg/mL) in triplicate to each well of a 96 well plate. 25 µL of a mixture of 1 mL of reagent A (alkaline copper tartrate solution) with 20 µL of reagent S was then added to each well. This was followed by adding 200 µL of reagent B (dilute Folin reagent) to each well. The plate was shaken for 30 min and the absorbance at 750 nm read in a microplate reader. The standard protein series was then plotted against absorbance and the best-fit line used to determine the protein concentrations in the tumour samples.

2.3.5.7 VEGF ELISA

Tumour VEGF levels were determined using the VEGF Quantikine kit (R&D systems) and by following the manufacturer's protocol. The plates were read using a microplate reader set to 450 nm with wavelength correction for 570 nm. VEGF levels for each sample were normalised for protein concentration.

2.3.6 Statistics

All statistical analyses were performed using Prism version 5.04 (GraphPad Software). Data points are expressed as means and bars are standard errors of the mean. Analyses performed to compare mean values of groups were either two-tailed t-tests or one-way analysis of variances (ANOVAs). A Bonferroni correction was performed on the data assessing specificity of ^{111}In-bnDTPA-bevacizumab due to multiple comparisons. All datasets were found to be normal, therefore only parametric statistical tests were performed. For best-fit lines a linear regression was used for linear data. For the competitive binding assay a one site-fit logIC_{50} curve was used described by: $y = bottom + (top - bottom)/(1 + 10^{(X - logIC50)})$, where top and bottom are plateaus in the units of Y-axis, and logIC_{50} is the log of the concentration of inhibitor that results in half-way binding between top and bottom. For saturable kinetics, a one-site, specific binding curve was used, expressed as: $y = Bmax.x/(Kd + x)$, where Bmax is the maximum specific binding and Kd is the equilibrium binding constant. *P*-values of <0.05 are considered statistically significant and denoted with a * on graphs. (*P*<0.01=**; *P*<0.001 =***; *P*<0.0001=****).

2.4 Results

2.4.1 Synthesis

Synthesis of the ^{111}Indium-labeled bevacizumab was performed as per the schema in (Figure 8).

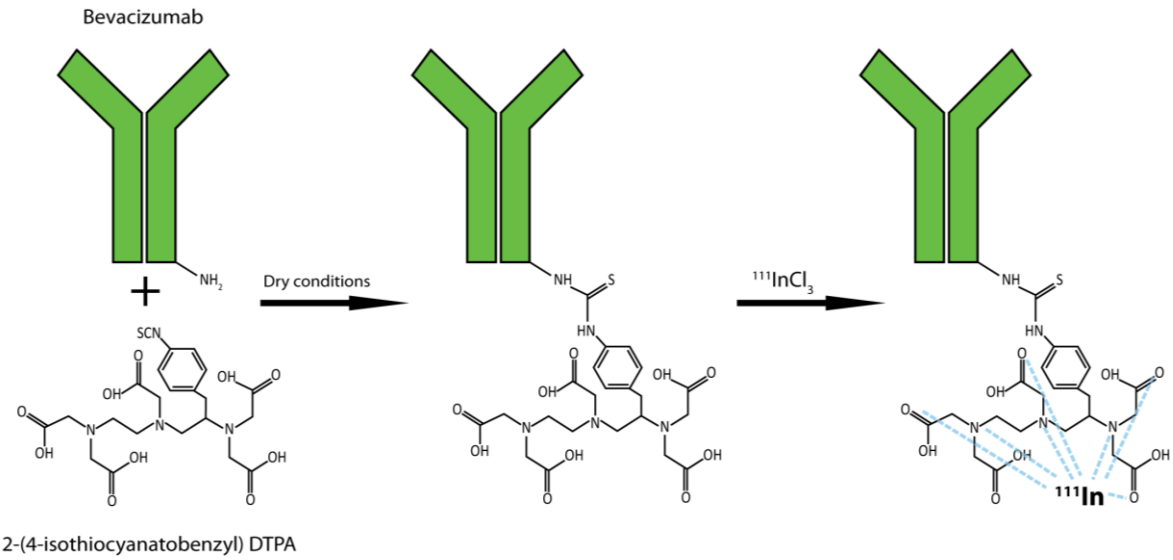


Figure 8: Synthesis of ^{111}In-bnDTPA-bevacizumab

2.4.1.1 Stoichiometry

Stoichiometry of bnDTPA binding to bevacizumab was determined by varying the molar excess of DMSO-bnDTPA solution added to bevacizumab (whilst keeping the absolute concentration of DMSO-bnDTPA constant) and performing HPLC after incubation. The ratio of bnDTPA molecules bound to each bevacizumab antibody was calculated by multiplying the percentage decrease in absorbance by the molar excess (Figure 9). The results show that a 4 molar excess of bnDTPA is required for a 1:1 conjugation ratio of bnDTPA to bevacizumab. For further manufacture of conjugated bnDTPA-bevacizumab a 6.6 molar excess was used, which yields on average 1.4 bnDTPA molecules per bevacizumab antibody.

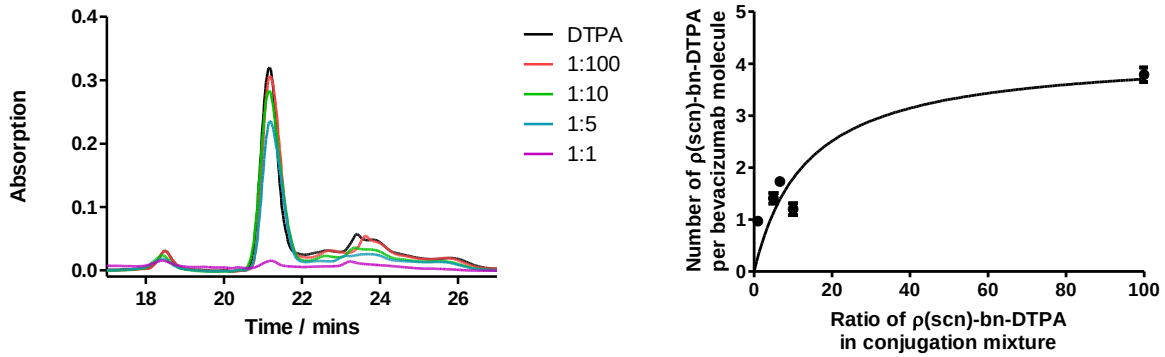


Figure 9: Stoichiometry of bnDTPA conjugation. **A**: changes in the UV absorbance peak of bnDTPA when varying the molar ratio used for conjugation with bevacizumab. **B**: number of molecules of bnDTPA conjugated to bevacizumab when using different molar ratios of bnDTPA.

2.4.1.2 Protein purification

The optimal method of purifying bnDTPA-bevacizumab from free bnDTPA was investigated. Antibody recovery was 10-20% using gel filtration chromatography compared to less than 1% when using a protein A column. Therefore, further experiments were performed using the G50 column for protein purification. The protein concentration of the G50 column eluates consistently peaked after 850 µL had been eluted (FIGURE 10). In order to minimise free DTPA and maximise the concentration of protein within the eluate, just 350 µL of eluate was used for reaction purposes after the first 500 µL of eluate had been discarded, i.e. the eluates up to the peak protein concentration were taken. The purity of the resulting eluates was confirmed by ITLC.

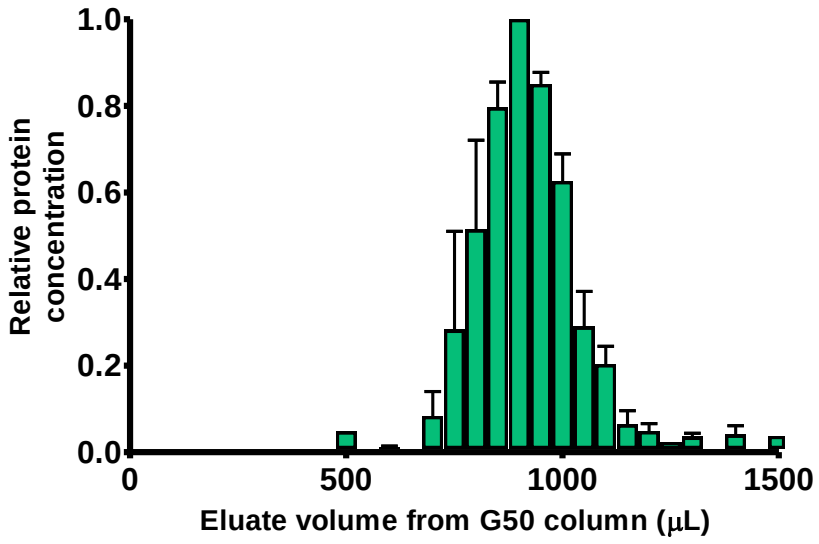


Figure 10: Protein concentrations of G50 column eluates. Bars are SEM.

2.4.1.3 Radiolabelling

Radiolabelling was confirmed by ITLC, which demonstrated radiochemical purity of >95% when using either cDTPA or bnDTPA for conjugation. This confirms that there is no significant difference in the conjugation characteristics between the two types of DTPA. However, bnDTPA is preferred over cDTPA as it confers several advantages. cDTPA has carboxylate groups at each end that can either accept a radionuclide metal ligand (such as ^{111}In) or ε-amino groups of lysine side chains found on the antibody. This means that it has the potential to cause cross-linking of the antibody either intra or intermolecularly [139]. Also the resulting complexes are known to be thermodynamically and kinetically unstable *in vivo* leading to release of ^{111}In into the blood [140]. BnDTPA avoids these problems as it is bifunctional and has a protein binding site (isothiocyanate group) that is independent of the metal (^{111}In) chelating group. Binding of the protein to the bnDTPA is via a thiourea bond leaving the remainder of the molecule intact thus ensuring stability of the metal-ligand complex [141]. This complex is also relatively stable in aqueous solution and can be stored for long periods without degradation. On the basis of these results only bnDTPA was used for *in vivo* experiments.

Analysis of the components and final radiolabelled product was performed by HPLC (FIGURE 11). This demonstrates 2 specific peaks in ultraviolet (UV) absorbance of ^{111}In-bnDTPA-bevacizumab. The first is at 12 min and represents the bevacizumab antibody, whilst a second peak at 18.4 minutes represents absorbance by the citrate buffer. The purified bnDTPA-bevacizumab and the radiolabelled version demonstrate no evidence of a free bnDTPA peak which would be expected after 21 min (FIGURE 9). Radioactivity of ^{111}In-bnDTPA-bevacizumab peaked at 12 min coinciding with the UV trace for bevacizumab, thus indicating ^{111}In bound to bevacizumab (FIGURE 12). A second peak on radio-HPLC was demonstrated at 19 min which is most likely to represent unbound ^{111}In. As the time of incubation of $^{111}InCl_3$ with the bnDTPA-bevacizumab was increased the amount of ^{111}In binding increased (FIGURE 12). After 90 min of incubation >95% of the ^{111}In had

bound to the bnDTPA-bevacizumab. Therefore, for optimal binding >90 min incubation times were used.

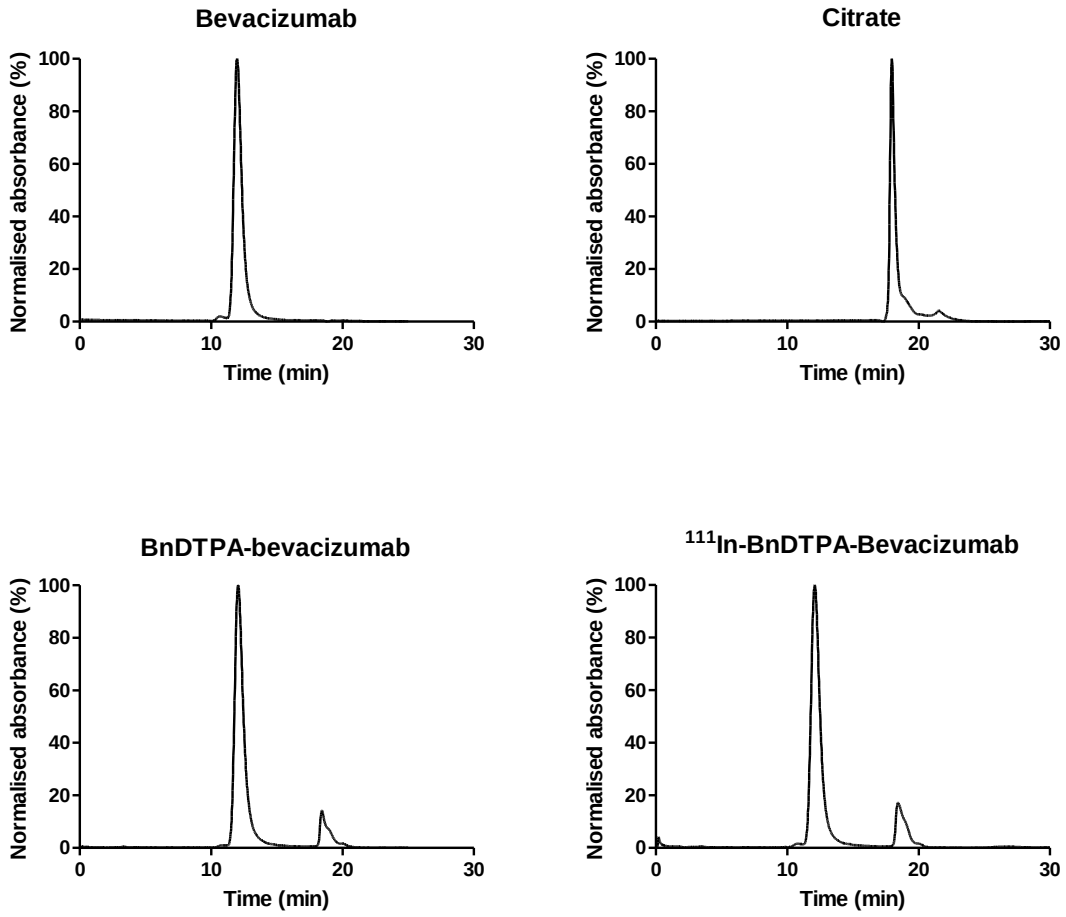


Figure 11: HPLC demonstrating UV absorption characteristics at 280 nm of components of ^{111}In-bnDTPA-bevacizumab manufacture

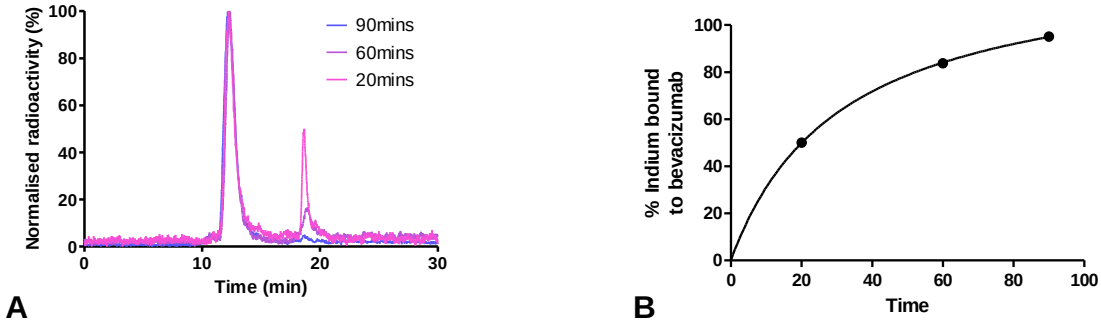


Figure 12: Radio-HPLC of ^{111}In-bnDTPA-bevacizumab. **A**: Radio-HPLC performed after incubation of $^{111}InCl_3$ with bnDTPA-bevacizumab for 20, 60 and 90 min. **B**: Amount of ^{111}In bound to bnDTPA-bevacizumab as time of incubation increases.

2.4.2 *IN VITRO* SPECIFICITY

To test whether radiolabelled bevacizumab retains a similar affinity for VEGF as the unmodified (or cold) bevacizumab, competitive binding assays were used. The assay competed 1 nM of radiolabelled bevacizumab for binding on VEGF expressing cells in the face of increasing amounts of cold bevacizumab. The half maximal inhibitory concentrations (IC_{50}) for ^{111}In-cDTPA-bevacizumab and ^{111}In-bnDTPA-bevacizumab (FIGURE 13) were 1.45 nM (standard deviation (SD)=1.12 nM) and 0.84 nM (standard deviation=0.45 nM) respectively. These results confirm that the radiolabelling process does not significantly alter the binding of bevacizumab for VEGF.

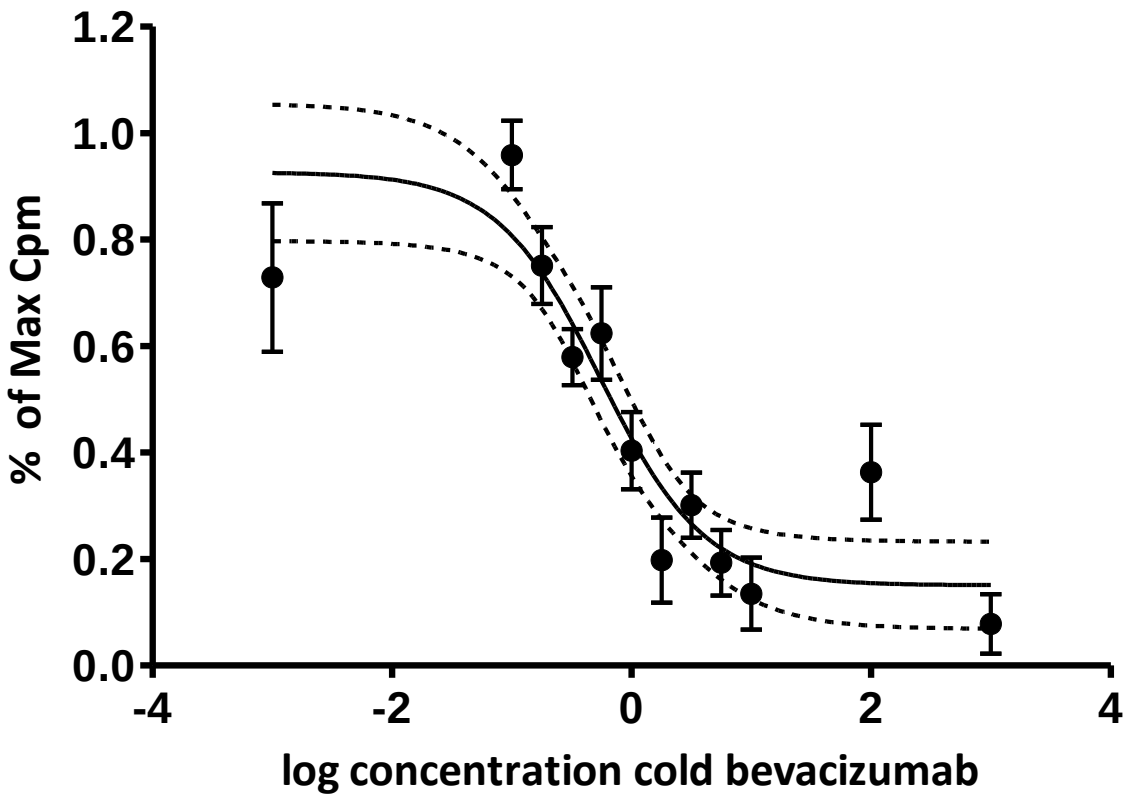


Figure 13: *In vitro* specificity of ^{111}In-BnDTPA-bevacizumab: Continuous line indicates the best fit for a one site competitive binding assay. The dotted lines represent the 95% confidence intervals. Error bars are SEM.

2.4.3 *IN VIVO* CHARACTERISTICS

2.4.3.1 Tracer kinetics

The kinetics of ^{111}In-bnDTPA-bevacizumab uptake in tumour and organs in a mouse model were determined by dissection of organs and tumour at different timepoints over the course of a week following intravenous administration of the radioimmunoconjugate. Tumour uptake was calculated as a percentage of the original injected dose and normalised for weight of specimen (%ID/g). Tumour uptake peaked on day 5 whilst organ uptake gradually decreased from day 1 (FIGURE 14A). The greatest signal to background as measured by calculating the ratio of uptake between the tumour and muscle (T:M ratio) was observed at 5 days post-injection (FIGURE 14B) though this was not statistically significant from day 7.

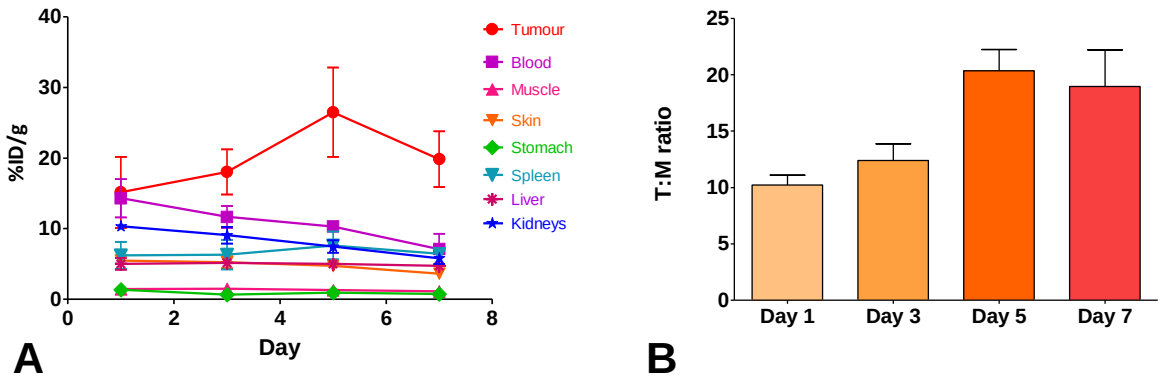


Figure 14: Kinetics of uptake of ^{111}In-bnDTPA-bevacizumab in LS174T xenografts and organs in female balb/c nude mice. **A** = uptake measured by %ID/g, error bars are standard deviations; **B**= uptake measured by tumour to muscle ratio, error bars are SEM ANOVAs of tumour demonstrated a statistically significant difference between the means of each day (%ID/g - *P*=0.03; T:M - *P*=0.01).

On the basis of these results subsequent experiments were performed using day 5 post-injection as optimal for uptake and visualisation of ^{111}In-bnDTPA-bevacizumab.

Tumour uptake values as measured by either %ID/g or T:M ratios correlated well with each other, with a Spearman's rank correlation coefficient of 0.74 (P<0.0001).

2.4.3.2 Biodistribution

Distribution of ^{111}In-bnDTPA-bevacizumab (FIGURE 15) was determined in different xenografts expressing VEGF (FaDu, LS 174T and 786-O). After 5 days uptake was higher in tumours compared to normal tissues for all cell lines tested. The next highest uptake was seen in the blood and less than 10%ID/g was seen in other organs.

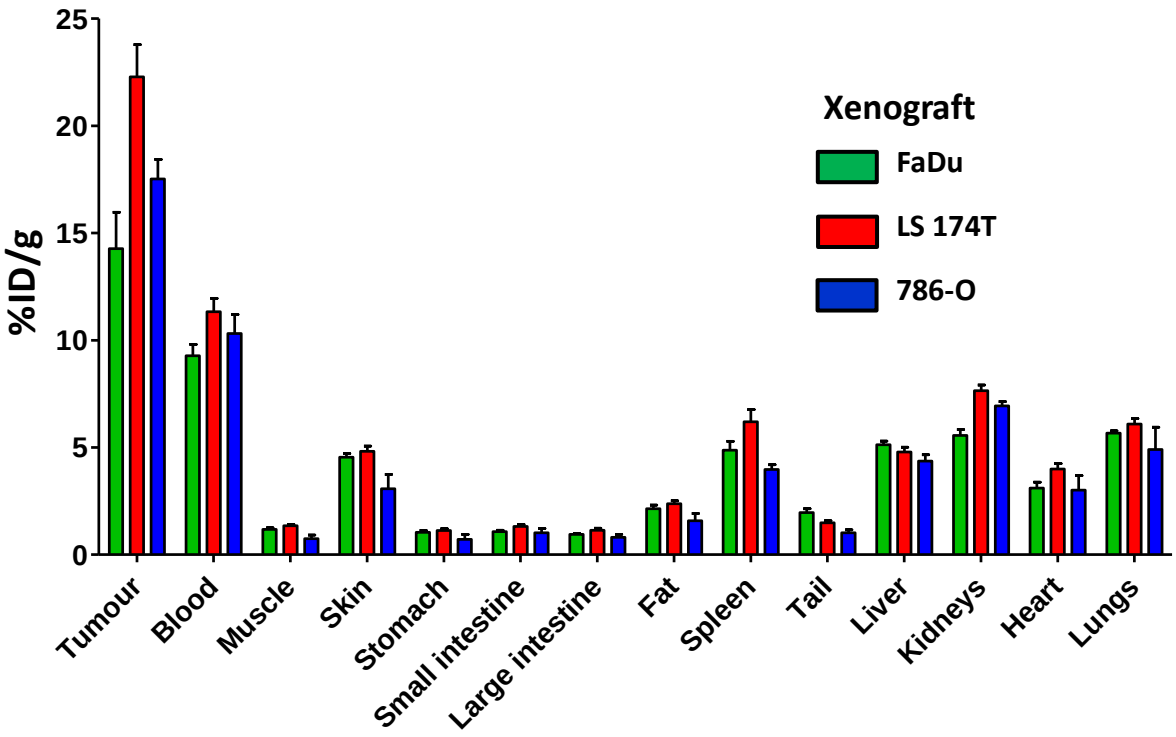


Figure 15: Distribution of ^{111}In-bnDTPA-bevacizumab after 5 days in mice bearing different tumour xenografts. Error bars are SEM.

Local distribution of ^{111}In within the tumours was visualised by autoradiography and was compared with distribution of bevacizumab as determined by IHC (FIGURE 16). This demonstrated good colocalisation of the radioactivity and antibody indicating that uptake within the tumours was predominantly with the intact antibody and radiolabel. This is supported by the low uptake in spleen and liver, which would have been higher if the tracer had dissociated *in vivo* and released free ^{111}In into the blood.

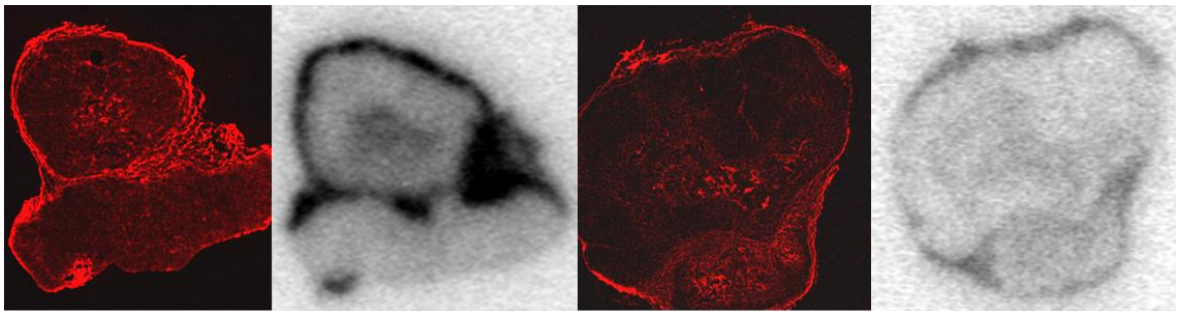


Figure 16: Comparison of autoradiographs with IHC of bevacizumab. These are images of whole sections of 2 different LS 174T xenografts injected with ^{111}In-bnDTPA-bevacizumab and an excess of cold bevacizumab at 5 days. The colour images are immunofluorescence staining for bevacizumab and the black and white images are the autoradiographs (blacker the image the higher the radioactivity) showing intratumourall ^{111}In. distribution. Immunofluorescence images provided by Sarah Able.

2.4.3.3 Dependence of radiotracer accumulation on tumour size

There is evidence that size of tumour may influence the uptake of radiotracers [142], with greatest effect in tumours less than 10 g in mass [143]. In these studies of the uptake of ^{111}In-bnDTPA-bevacizumab, there is no evidence of mass of tumour having an effect on uptake (FIGURE 17).

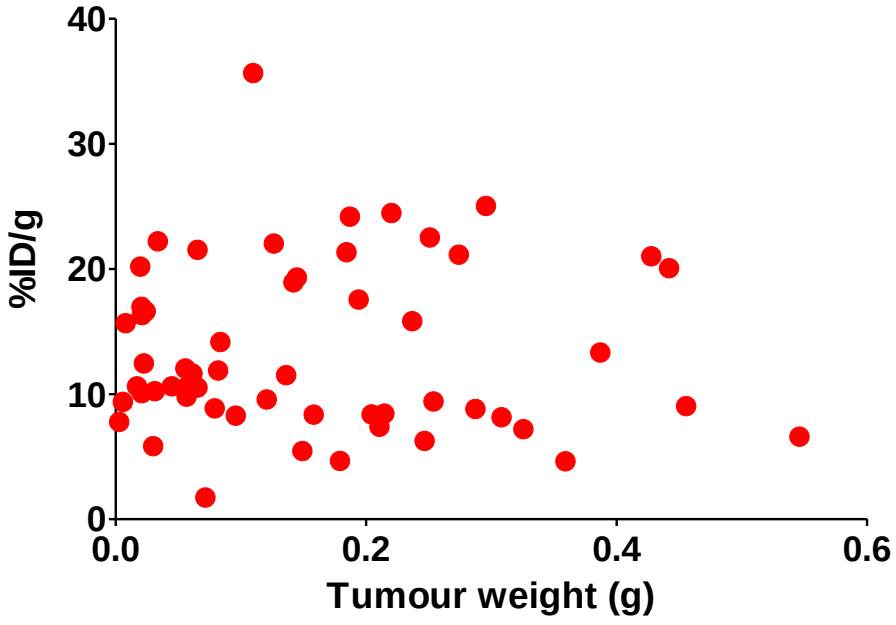


Figure 17: Comparison of weight of tumour (FaDu xenograft) against uptake of ^{111}In-bnDTPA-bevacizumab (%ID/g). There is no correlation. Spearman's rank correlation coefficient, r = -0.06

2.4.3.4 Specificity

Specificity of uptake of ^{111}In-bnDTPA-bevacizumab in xenografts (FaDu, LS174T and 786-O) was tested by comparing uptake of the tracer to that of a non-specific isotype matched antibody (^{111}In-bnDTPA-IgG1κ) and with an excess (100 fold=300 μg) of cold bevacizumab. Uptake of the control antibody was less than 5 %ID/g in all xenografts and similar to uptake of tracers within a negative control cell line (MDA-MB231 IE3) which expressed very low levels of VEGF (FIGURE 18). In addition, uptake of ^{111}In-bnDTPA-bevacizumab was suppressed when an excess of cold bevacizumab was coinjected. In contrast normal tissue uptake was not significantly altered by the addition of an excess of cold bevacizumab. These results confirm that ^{111}In-bnDTPA-bevacizumab binds specifically to the xenografts and that an excess of cold bevacizumab competitively inhibits the binding of the tracer. This is supported by SPECT-CT imaging of the mice which displayed strong uptake of tracer within the tumours in the mice injected with ^{111}In-bnDTPA-bevacizumab in comparison to those that received ^{111}In-bnDTPA-IgG1κ (FIGURE 19).

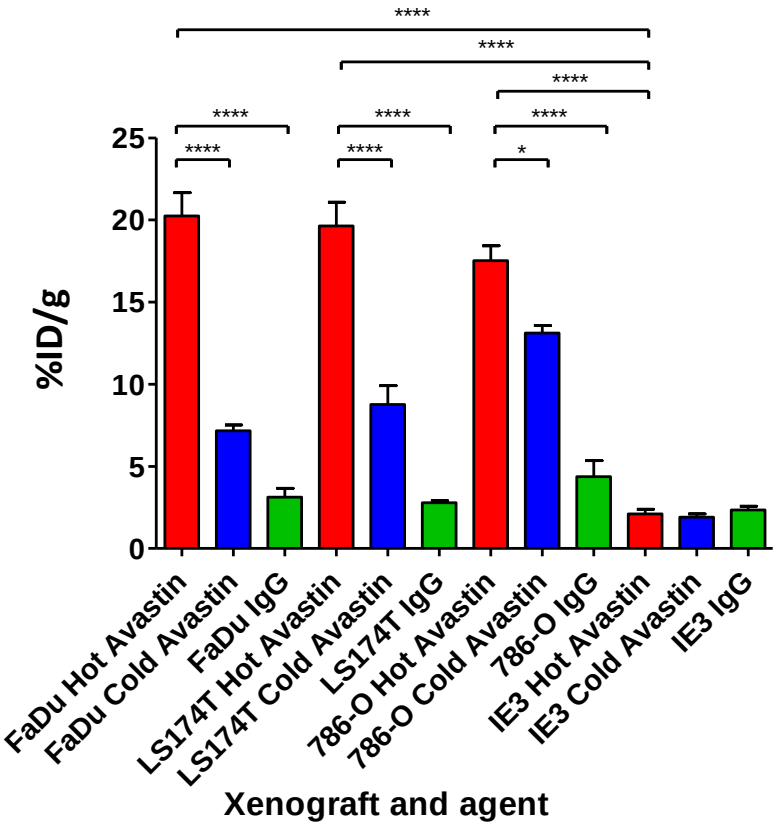


Figure 18: *In vivo* specificity of uptake of ^{111}In-bnDTPA-bevacizumab. Average uptake of different imaging agents (Hot Avastin=^{111}In-bnDTPA-bevacizumab; cold Avastin= ^{111}In-bnDTPA-bevacizumab + excess of cold bevacizumab; IgG=^{111}In-bnDTPA-IgG1κ) in different tumour models. Error bars are SEM. (*=P<0.05; ****=P<0.0001). A Bonferroni correction was applied to the analysis of this table.

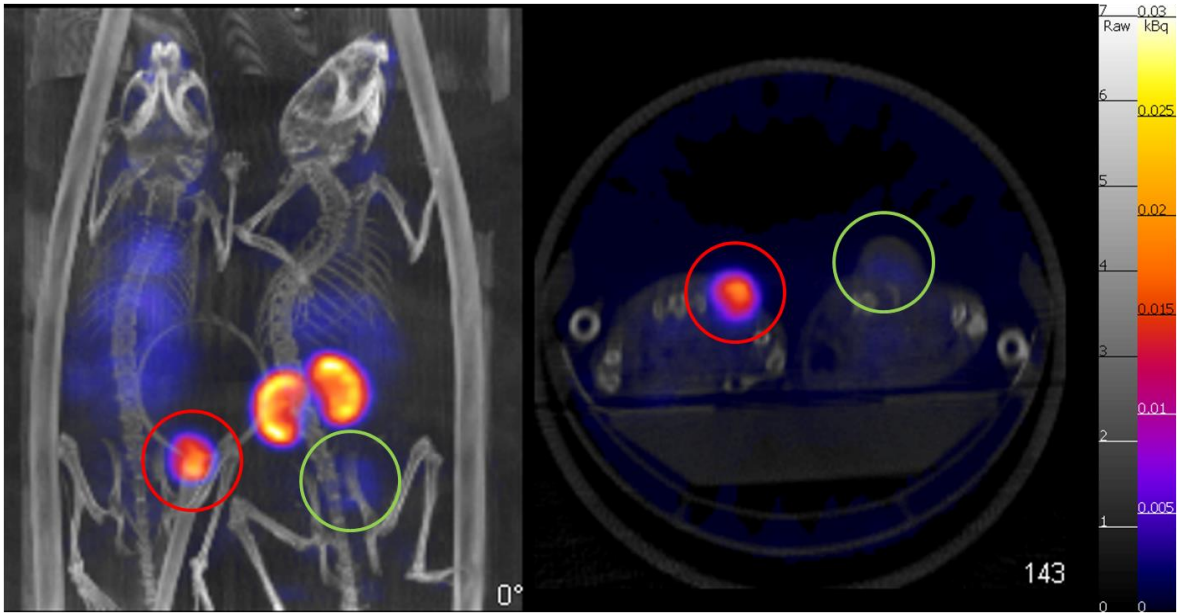


Figure 19: SPECT-CT of FaDu xenograft bearing mice injected with either ^{111}In-bnDTPA-bevacizumab (left mouse, red circle for tumour) or ^{111}In-bnDTPA-IgG1κ (right mouse, green circle for tumour) . The left panel is a maximum intensity projection (MIP) image. The right is a single transaxial image at the level of the tumours in both mice.

2.4.3.5 Xenograft VEGF levels

The levels of VEGF within the xenografts were determined using VEGF ELISAs after homogenisation of the tissues (FIGURE 20). These demonstrate that LS 174T and FaDu xenografts produce significant levels of VEGF. However, only a low level of VEGF was detectable in 786-O xenografts. A similar result was obtained when ELISAs were performed on conditioned media from the different cell lines. The level of VEGF in 786-O cells was similar to that in the negative control cell line (MDA-MB 231 IE3= 1.6 pg/g of protein; 786-O=1.02 pg/g of protein), which was significantly less than in VEGF-expressing cell lines, LS174T and MDA-MB231 2F11. This result appears inconsistent with the apparent specificity of uptake of the tracer in the 786-O xenograft model. One possible reason for the discrepancy is that in 786-O cells VEGF is undetectable using an ELISA assay because of the presence of an inhibitor to binding of VEGF (e.g. soluble VEGFR, which sequesters VEGF and prevents it binding to its receptors). This was investigated by taking conditioned media from LS 174Ts and seeing if VEGF levels as measured by ELISA were suppressed by the addition of 786-O media. ELISAs of LS 174T media demonstrated statistically

significant higher VEGF levels (245.5 ± 3.1 pg/g of protein) in comparison to the mixture with 786-O media (150.2 ± 2.8 pg/g of protein) when analysed with an unpaired t-test (*P*=0.002). This helps clarify the discrepancy between the results of the specificity experiment and the VEGF ELISAs of the tumours, though, the identity of the putative inhibitory factor is not known.

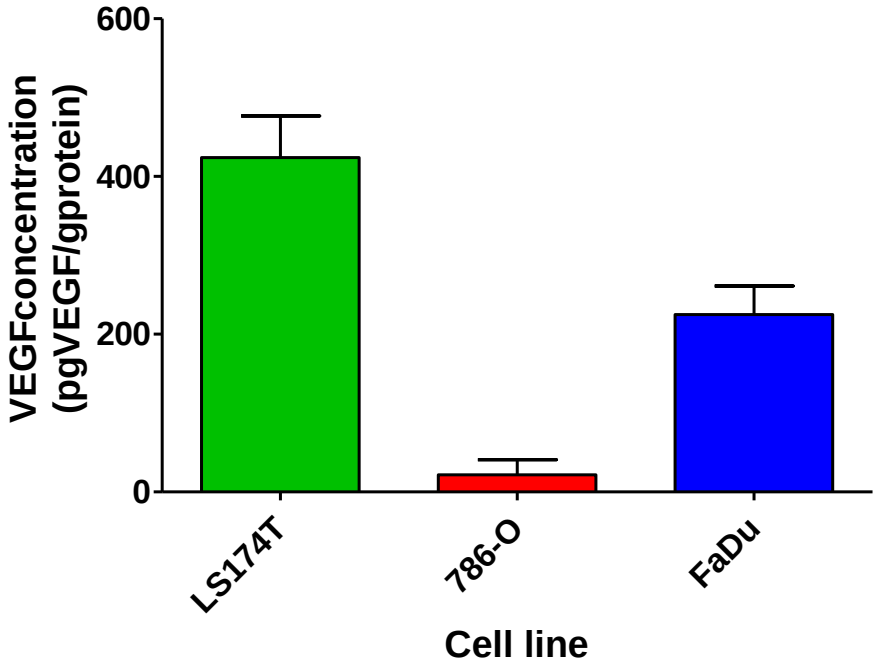


Figure 20: VEGF levels in xenografts as measured by ELISAs of homogenised specimens. Error bars are SEM.

VEGF levels (as determined by ELISA) from the LS 174T and FaDu xenografts were compared to uptake of ^{111}In-bnDTPA-bevacizumab (FIGURE 21), which showed there is no correlation. This lack of correlation may relate to freely diffusible isoforms of VEGF (such as $VEGF_{121}$) which may not affect uptake of tracer but may be measured by the VEGF ELISA [136]. To resolve this, comparison was made between localisation of tracer on autoradiographs and VEGF by immunohistochemistry (FIGURE 22). This shows that distribution of the tracer and VEGF colocalise, which indicates that the tracer is binding specifically to VEGF in the tumours.

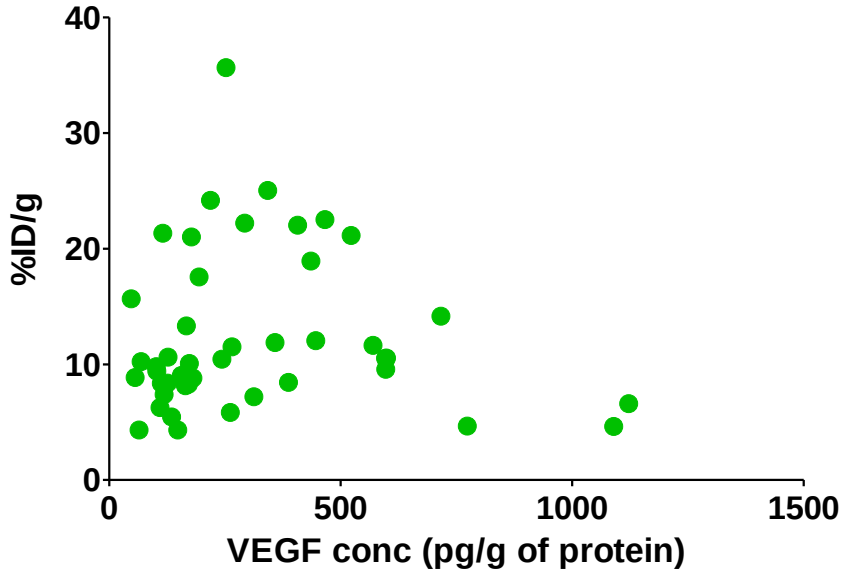


Figure 21: Comparison of VEGF levels in xenografts with uptake of ^{111}In-bnDTPA-bevacizumab. There is no evidence of a correlation.

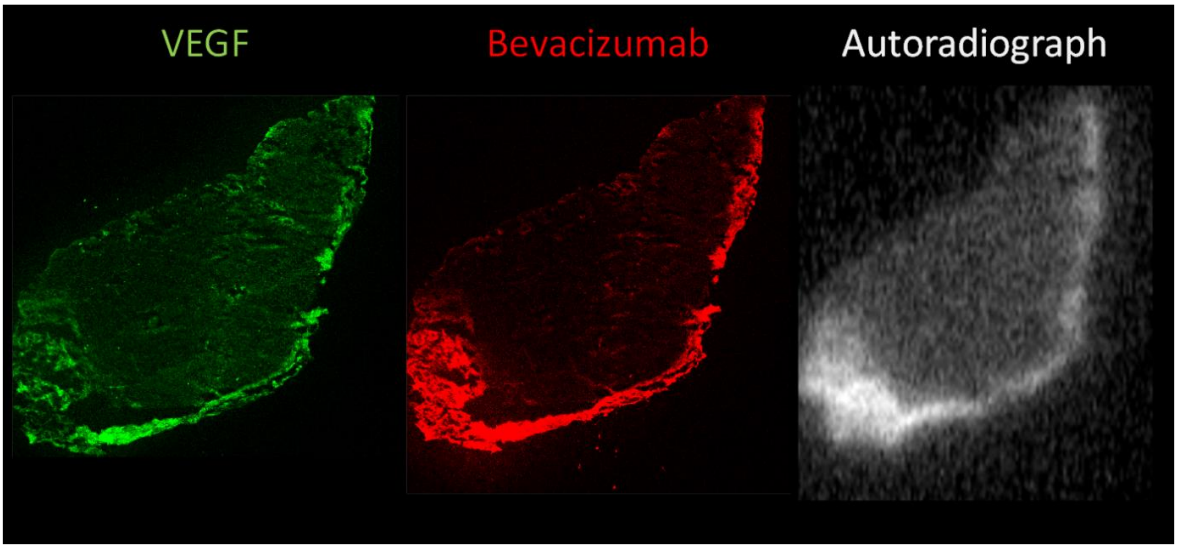


Figure 22: Comparison of the distribution of VEGF, bevacizumab and ^{111}In in a FaDu xenograft section. The right image is an autoradiograph that has been inverted in scale so that whitest areas are the regions of highest radioactivity. Immunofluorescence images are provided by Sarah Able.

2.5 Discussion

There are several antibody imaging approaches to assessing the VEGF status of a tumour. Of the antibodies available, bevacizumab was chosen as it is commercially available and readily supplied to a clinical standard. In addition, in comparison to other potential antibodies its biology has been intensively investigated and well characterised. Furthermore, it is envisaged that as the antibody is produced in line with good manufacturing practice (GMP) and already used as a therapy in patients, it will be practical to translate its use as an imaging probe into clinical use.

Labelling of an antibody with a radionuclide for imaging requires a radionuclide with a half-life comparable to the time taken for the antibody to reach optimal target to background ratio. This is a function of the time taken for the antibody to reach and bind specifically to the target and for the background uptake (especially in the blood) to clear. For antibodies the optimal time for uptake is between 3-7days. This limits the radionuclides suitable for imaging to PET radionuclides such as ^{124}I, ^{64}Cu, ^{86}Y and ^{89}Zr; and SPECT radionuclides such as ^{123}I, ^{67}Ga and ^{111}In. ^{111}In was chosen as it has been extensively used for radiolabelling of antibodies and has relatively simple chelation steps which occur at room temperature and with good yield. Similar to the rationale for using bevacizumab, ^{111}In can be obtained by clinical distributors which would facilitate its translation into clinical imaging.

The synthesis of radiolabelled bevacizumab was performed successfully with yields of up to 20% and a very high radiochemical purity (>95%). This compares favourably with the yields from the Nijmegen group that first reported on the use of ^{111}In-bevacizumab and used slightly different reaction conditions and purification techniques [35, 135]. A 6.6 molar excess of the chelator was used in conjugation with the antibody and did not significantly interfere with binding of the antibody to VEGF *in vitro*.

In vivo, 3 µg of bevacizumab was chosen for uptake studies as this has been previously shown to be an optimal dose [135]. Uptake of tracer within xenografts increases with increasing amounts of

antibody until the binding sites on the tumour are saturated [135]. The tracer demonstrated high levels of uptake in the VEGF expressing xenografts (up to 40%ID/g) with relatively low uptake within the normal organs. This is reassuring for imaging purposes as it leads to excellent visualisation of the tumour as seen in Figure 19.

Pharmacokinetic analyses demonstrated that the greatest uptake and greatest tumour to background ratio occurs at 5 days after injection. This differs from the data reported by Stollman et al [135] who showed in the same tumour model that uptake was greatest on day 3 and the tumour to background ratios increase over the week with day 7 post-injection having highest values. However, these investigators did not measure uptake values on day 5 and so may have missed the peak signal to background ratio. The overall implication of these pharmacokinetics is that in patients, the optimal time for imaging would be after a few days post-injection. This is comparable to other monoclonal antibodies used for clinical imaging such as ^{111}In-capromab pendetide (Prostascint) where optimal images are obtained between 4-6 days post-injection [144].

The stability of ^{111}In-bnDTPA-bevacizumab has been investigated previously. 7 days of storage of the tracer in human serum at 37^{o}C resulted in ≤5% decrease in antibody-bound radioactivity [35]. This is consistent with our results which demonstrate good colocalisation of radioactivity of tracer and antibody on histological specimens 5 days after injection and also low uptake in the liver and spleen in keeping with low levels of free ^{111}In in the blood.

^{111}In-bnDTPA-bevacizumab accumulated specifically in tumours. This was demonstrated for the first time in 3 different VEGF-expressing xenograft models by suppression of uptake through competitive inhibition by an excess of cold bevacizumab and by comparison with an ^{111}In-labelled IgG isotype-matched control antibody. Specificity for VEGF, however, was not supported by comparing uptake with VEGF ELISAs of the tumour tissue. This probably represents a differential in the isoforms of VEGF being detected. ^{111}In-bnDTPA-bevacizumab is hypothesised to detect

predominantly matrix and cell membrane associated VEGF (e.g. $VEGF_{165}$ and $VEGF_{189}$), whereas the ELISA would recognise all isoforms including diffusible forms such as $VEGF_{121}$. Evidence for this is that the spatial distribution of VEGF in histological sections from the tumours colocalised with the tracer on autoradiography. This has not been previously demonstrated by other groups. In addition, uptake of ^{111}In-bnDTPA-bevacizumab has been shown to only be specific in blocking studies with tumours expressing $VEGF_{165}$ and $VEGF_{189}$ in comparison to those expressing $VEGF_{121}$ [136]. The results also correspond with the first clinical trials of ^{111}In-bnDTPA-bevacizumab in patients with colorectal cancer liver metastases and RCC, in which no correlation was established between uptake of ^{111}In-bnDTPA-bevacizumab and VEGF levels measured by ELISA and ISH [137, 145].

2.6 Conclusion

^{111}In-bnDTPA-bevacizumab can be used to visualise VEGF within tumours. In particular it is likely to be specific for matrix and cell membrane associated forms of VEGF. It holds promise as a tool for investigating VEGF expression within tumours. This has important implications as VEGF levels correlate with prognosis and may be useful for guiding patient management, especially with the development new antiangiogenic therapies.

3 Clinical Validation of Integrin Imaging

3.1 Introduction

3.1.1 Integrins in Angiogenesis

In addition to VEGF, numerous other molecules that modulate angiogenesis have been identified. Amongst them are the cell adhesion molecules including integrins, which are important mediators of angiogenesis [42]. Integrins are a large family of cell-surface receptors that bind and mediate adhesion to ECM components, organise the cytoskeleton, and activate intracellular signalling pathways [146]. Of the 24 known integrins, a number have been implicated in cancer growth and invasion including $\alpha_v\beta_3$, $\alpha_v\beta_5$, $\alpha_2\beta_1$, $\alpha_5\beta_1$, $\alpha_6\beta_1$ and $\alpha_6\beta_4$ [147]. For tumour angiogenesis $\alpha_v\beta_3$ and $\alpha_v\beta_5$ have been found to be especially critical [148, 149].

The $\alpha_v\beta_3$ integrin was the first integrin associated with angiogenesis [150]. It is found on endothelial cells, smooth muscle cells and haemopoietic cells such as platelets and osteoclasts. In particular, it is highly expressed on activated endothelial cells and some solid tumour cells. $\alpha_v\beta_3$ leads to increased expression of and sensitivity to VEGF [151, 152]. Clinical studies have demonstrated that $\alpha_v\beta_3$ is over-expressed in tumours, and its expression correlates with tumour grade and histological type [51, 153-155]. High expression levels are associated with increased cell invasion and metastasis [156]. Given the important role integrin $\alpha_v\beta_3$ plays in tumour angiogenesis and cancer progression, the ability to visualise and quantify $\alpha_v\beta_3$ integrin expression level within tumours and $\alpha_v\beta_3$-associated angiogenesis may offer significant clinical benefit.

3.1.2 RGD-based imaging agents

In the early 1980s, the arginine-glycine-aspartate (RGD) tripeptide sequence was characterised as the cell attachment site for fibronectin (an ECM protein) with its cell surface receptor [157]. Subsequently the motif was identified in other ECM proteins (e.g. vitronectin, osteopontin and fibrinogen) as a binding site for integrin receptors and also found in snake venoms leading to inhibition of integrin-mediated cell adhesion [158]. Of particular significance was the finding that

RGD peptides interact with integrins, such as $\alpha_v\beta_3$ and $\alpha_v\beta_5$, that are overexpressed in tumour and angiogenesis. It was further observed that though the integrins recognised the RGD motif, they were also able to discriminate between different ligands [159]. For example $\alpha_5\beta_1$ only binds to fibronectin, whereas $\alpha_v\beta_3$ binds to several ECM proteins including vitronectin, fibrinogen and fibronectin [160]. It was hypothesised that this may be due to the secondary and tertiary structures of the RGD sequence, dependent on the protein in which the sequence is present. This has guided the development of synthetic RGD compounds, initially leading to cyclisation to restrict their conformational freedom and thus improve selectivity [161].

Subsequent investigation into RGD peptides has generated a variety of agents for the treatment and imaging of cancer and cardiovascular disease. The first RGD-based antiangiogenic therapy used in clinical trials was cilengitide, a cyclic RGD molecule which is currently being tested in Phase III trials in several cancer groups including brain tumours [160]. For imaging, development started with cyclic monomeric compounds and has now progressed to encompass multimeric, nanoparticle and microbubble agents.

[^{18}F]-galacto-RGD was the first RGD agent to be used in clinical trials for imaging. It is a glycosylated RGD molecule which is more hydrophilic than cyclic RGD [162]. This has the advantage of increased renal excretion compared to cyclic RGD, which is excreted predominantly via the hepatobiliary route leading to high bowel activity [163, 164]. [^{18}F]-galacto-RGD has high specific affinity for $\alpha_v\beta_3$, 200-1200 fold greater than for $\alpha_v\beta_5$ and $\alpha_{IIb}\beta_3$ [164]. Tumour uptake in xenograft models has demonstrated a good correlation with α_v levels when using tumours expressing varying levels of $\alpha_v\beta_3$ [50].

[^{18}F]-galacto-RGD uptake was first evaluated in 2005 in clinical trials that involved subjects with a variety of malignant and benign conditions. Resection of tumours in 6 patients demonstrated good correlation between IHC of $\alpha_v\beta_3$ vessel density and tumour uptake (r=0.94, P=0.005) [50]. Uptake of [^{18}F]-galacto-RGD was then further compared with histological markers of angiogenesis

in a subsequent study. In 19 patients with a range of solid tumours, uptake was demonstrated to correlate with intensity of $\alpha_v\beta_3$ staining and MVD [51]. A further study investigated the use of [^{18}F]-galacto-RGD in detecting tumours in patients with squamous cell carcinoma of the head and neck. Uptake in 10 out of 12 tumours was demonstrated. Both tumours that were not detected by [^{18}F]-galacto-RGD were <5 mm in diameter and were also not detectable using MRI or CT. It was also shown that tumour size and uptake did not correlate with each other, and that kinetics of uptake were consistent with a two-tissue compartment model with reversible specific binding [165]. Later studies investigated the use of [^{18}F]-galacto-RGD in breast cancer and malignant gliomas with similar results [166, 167].

^{18}[F]-RGD-K5 is another RGD-based imaging agent that has been tested in clinical trials. In a first-in-man study of 12 patients with breast cancer, uptake was compared with that of ^{18}[F]-FDG [168] Of a total of 157 FDG-positive lesions, 122 were demonstrated by ^{18}[F]-RGD-K5 PET, with no correlation in SUV between the two tracers. There was no correlation between RGD-K5 PET uptake and histological parameters such as MVD. The authors of this report hypothesised that this was due to a lack of specificity of ^{18}[F]-RGD-K5, which is known to bind to a range of integrins. Another possible explanation was that $\alpha_v\beta_3$ is expressed on tumour cells as well as blood vessels.

Other RGD-based tracers used in clinical trials are two similar compounds developed by GE Healthcare: fluciclatide and maraciclatide, which are PET and SPECT agents respectively. Maraciclatide will be discussed below.

3.1.3 ^{99m}Tc-Maraciclatide (GE Healthcare)

Maraciclatide (also known as NC100692 and diamine dioxime-Lys-Cys-Arg-Gly-Asp-Cyc-Phe-Cys-polyethylene glycol) (Figure 23) is a cyclic synthetic ligand containing the RGD tripeptide sequence. It has a binding region for ^{99m}Tc thus enabling its use as a SPECT imaging agent. It is derived from the peptide Lys-Cys-Arg-Gly-Asp-Cyc-Phe-Cys (NC100717) which was identified by phage display screening as binding strongly to both $\alpha_v\beta_3$ and $\alpha_v\beta_5$ [169].

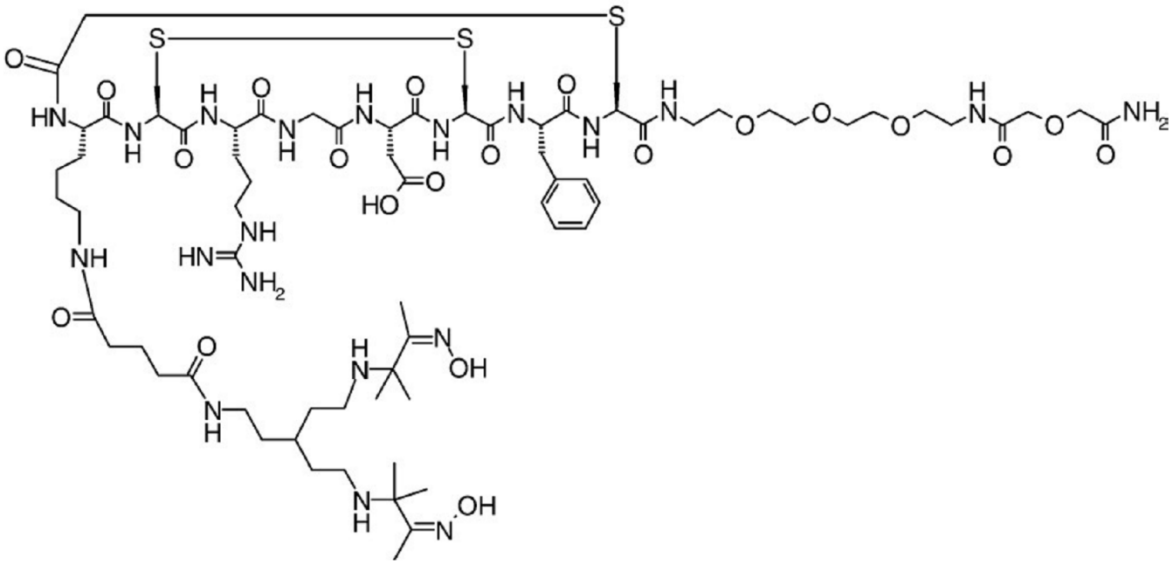


Figure 23: Chemical structure of maraciclatide. Reproduced with permission from [1]

Maraciclatide has a high affinity for the RGD receptor integrins $\alpha_v\beta_3$ (Kd=0.5±0.01nM) and $\alpha_v\beta_5$ (Kd=0.1±0.04nM), lesser affinity for $\alpha_5\beta_1$ and $\alpha_{IIb}\beta_3$ and no specific affinity for non-RGD receptor integrins such as $\alpha_1\beta_1$ and $\alpha_3\beta_1$ [1]. *In vivo* specificity has been demonstrated by competitive inhibition studies using excess unlabelled maraciclatide in C57BL/6 mice bearing Lewis lung tumours (unpublished data from GE Healthcare) (FIGURE 24).

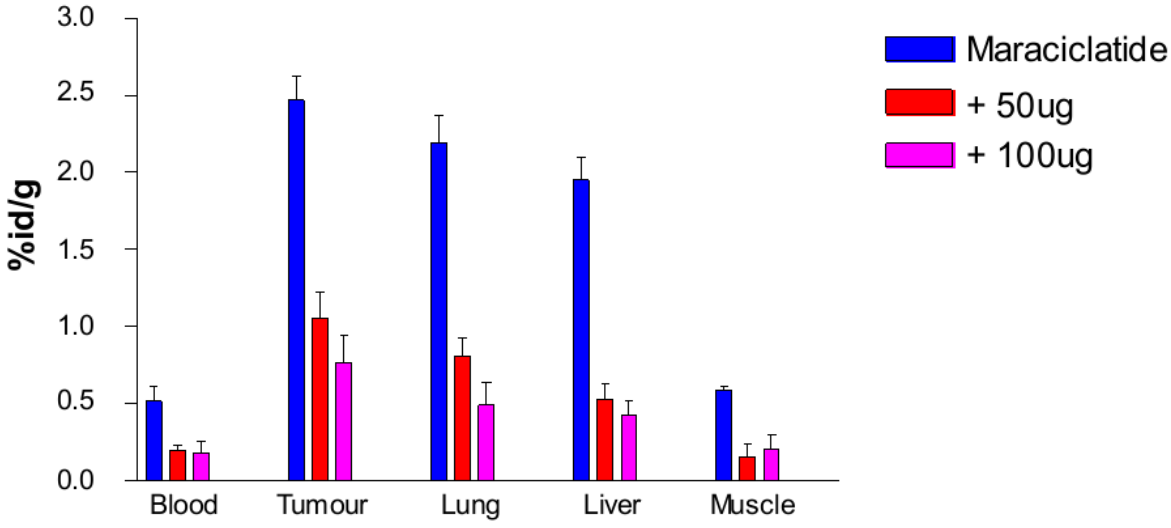


Figure 24: Distribution of ^{99m}Tc-maraciclatide with an excess of unlabelled maraciclatide. Uptake was measured 2 hours post injection in a mouse Lewis lung cancer sub-cutaneous model. (Provided courtesy of Matthew Morrison).

From biodistribution studies in rats, ^{99m}Tc-maraciclatide was found to be stable in blood and metabolised via the kidneys. Most radioactivity accumulates in the liver, kidneys and urine with only small amounts in other organs [1, 170]. Its use in ischaemia and infarction preclinical models shows high uptake in areas of neovascularisation where there is overexpression of α_v integrins [171, 172]. Binding of maraciclatide was shown to be localised on endothelial cells in regions of angiogenesis [173].

3.1.3.1 Clinical trials

The first clinical trial of ^{99m}Tc-maraciclatide in humans was a Phase I study in 25 healthy volunteers. The study demonstrated uptake in the liver and intestines, renal excretion, and minimal background in the thorax and brain [174]. A subsequent study investigated the use of ^{99m}Tc-maraciclatide for breast imaging. The majority, 86% (19 out of 22), of malignant lesions were detected. One ductal carcinoma in situ (DCIS) and 2 invasive lobular carcinomas were missed [174]. All lesions ≥1 cm in diameter were visualised including benign fibrocystic change, in which there was heterogeneous diffuse uptake, distinct from the characteristic appearance of malignant lesions. The tracer was well-tolerated by patients with only one adverse event of dysgeusia which resolved within a few minutes post-injection. A further study in patients with suspected breast cancer yielded similar results [175]. Another trial investigated its use for detection of metastases and found that it had potential for detection of lung and brain metastases from lung and breast primary cancers, whereas detection of liver and bone metastases was poor [55].

3.2 Aims

Early clinical studies have indicated the potential of ^{99m}Tc-maraciclatide as a tool for imaging sites of integrin expression, though these have been performed in a limited variety of tumour types. Comparison of ^{99m}Tc-maraciclatide uptake and histological markers of angiogenesis has been performed in preclinical studies, however, at present, there is no clinical evidence that imaging appearances of ^{99m}Tc-maraciclatide correlate with levels of angiogenesis within tumours.

The aims of this chapter were to:

- Describe the imaging characteristics of ^{99m}Tc-maraciclatide in tumour types not previously assessed in clinical trials.
- Determine whether ^{99m}Tc-maraciclatide uptake in tumours correlates with immunohistochemical markers of angiogenesis.

3.3 Materials and Methods

Please see Appendix B for full clinical trial protocol

3.3.1 Regulatory Approval

A clinical trial was set up to investigate the aims of this chapter. Ethical approval was granted by the Oxford Research Ethics Committee B (OxREC B) and the trial was provided sponsorship by the Research and Development (R&D) department of the Oxford Radcliffe Hospitals (ORH) National Health Service (NHS) Trust (now the Oxford University Hospitals (OUH) NHS Trust). The study was not classified as a clinical trial of an investigational medicinal product (CTIMP) by the Medicines and Healthcare Products Regulatory Agency (MHRA) and therefore a Clinical Trials Authorisation (CTA) was not required. The Administration of Radioactive Substances Advisory Committee (ARSAC) gave approval for the administration of the radiotracer ^{99m}Tc-maraciclatide to patients for the purposes of this trial.

3.3.2 Recruitment Criteria

Patients recruited to this trial were required to have a diagnosis of colorectal cancer (CRC), breast cancer or renal cell carcinoma (RCC) and were about to undergo surgical resection of the tumour. A diagnosis of RCC based purely on imaging appearances of detected tumours was acceptable, as biopsies are rarely performed prior to definitive resection. Study subjects were required to have adequate renal function (glomerular filtration rate (GFR)>50mL/min/1.73m^2) and to comply with the study protocol and follow-up schedule. Patients were excluded from the study if they were medically unfit due to non-malignant systemic disease, pregnant or lactating, had major surgery within 4 weeks of the study, were allergic to technetium or less than 18 years of age.

3.3.3 Patient Recruitment and Enrolment

Patients with CRC and RCC were identified at multidisciplinary team (MDT) meetings by participating clinicians. Patients with breast cancer were not identified at the MDT due to the

time constraints of their management pathway. They were either identified at assessment clinic or at the time of diagnostic biopsies performed by breast radiologists. Patients were approached at their outpatient clinic appointment and given a written information sheet (APPENDIX B) detailing the research procedures and potential risks and benefits. Patients were given at least 24 hours to consider the information and were telephoned to establish if they wished to participate in the trial. Those who agreed had an appointment organised for their trial scans. At this appointment written consent was obtained prior to commencement of trial procedures. Patients were free to withdraw from the trial at any time and any research data collected up to that point was used in trial analyses.

3.3.4 TRIAL PROCEDURES

On entry to the trial, patients were cannulated via an upper limb vein for administration of trial agents. After the scans had been performed the patient had their cannula removed and were allowed to go home.

3.3.4.1 ^{99m}Tc-maraciclatide scanning

3.3.4.1.1 Radiolabelling

Maraciclatide was provided in kit form by GE Healthcare as a sterile freeze-dried powder in a 10 mL glass vial containing 75 μg. The maraciclatide was radiolabelled in hospital radiopharmacy by the clinical radiopharmacists on the day of use as per the manufacturer's instructions. This involved adding 0.9-2.0 GBq of sodium [^{99m}Tc] pertechnetate in 3-5 mL to the vial and incubating for 20 min at 25^{o}C. An aliquot (0.2 mL) was removed from the vial and radiochemical purity was determined by ITLC. After ITLC confirmed adequate radiolabelling (>85%), 740 MBq ±10% was drawn up for administration to patients.

3.3.4.1.2 Scanning protocol

Up to 740 MBq of ^{99m}Tc-maraciclatide was administered to each patient whilst the patient was in the SPECT scanner. Scanning was performed in the nuclear medicine department by radiographers with a GE Infinia Hawkeye 4 or a Discovery 670 scanner using a low energy high resolution (LEHR, GE Healthcare) collimators. Patients were encouraged to drink water and void frequently and immediately prior to scanning. Immediately after injection of ^{99m}Tc-maraciclatide, dynamic images were taken for 15 min at 3 frames per minute. Planar static images were taken at 45 min and 2 h post injection. A SPECT-CT was performed at 1 h post injection. SPECT data were reconstructed using an ordered subsets expectation maximisation (OSEM) algorithm using 2 iterations and 10 subsets.

3.3.5 SURGERY AND HISTOLOGICAL ANALYSIS

After the trial scans were performed patients underwent tumour resection. The resected specimens were paraffin-embedded and sectioned by the Oxford Radcliffe Biobank (ORB) and the Oxford Centre for Histopathology Research (OCHRe). The samples were then sent to Dr Michael Koukourakis and Dr Alexandra Giatromanolaki, University of Alexandria, Greece, for immunohistochemical analysis and scoring.

3.3.5.1 Integrin β_3 IHC

IHC was performed using the Envision Flex+, Mouse, High pH kit (DAKO) and following the manufacturers protocol. First antigen retrieval was performed by placing the sections in citrate buffer (1:10 dilution, pH 9.0) and heated at 120^{o}c for 3 x 5 min, with cooling in between. Slides were then washed with the Envision Flex wash buffer for 3 x 5 min and were incubated overnight at 4^{o}c with the anti-integrin β_3 antibody (ab75872, Abcam), diluted at 1:100. After washing, endogenous peroxidase activity was neutralised using the Envision Flex Peroxidase Blocking reagent for 10 min. The slides were washed with the wash buffer for 5 min and then incubated with the secondary antibody (Envision Flex LINKER) for 15 min and were washed again with the

Envision Flex wash buffer. Then the slides were incubated with the Envision Flex/HRP for 30 min and washed again. The colour reaction was developed with the Envision Flex DAB + chromogen for 5 min. The sections were counterstained with Envision Flex haematoxylin, dehydrated and mounted. Normal species specific immunoglobulin-G was substituted for the primary antibody as the negative control.

3.3.5.2 CD31 IHC

The JC70 monoclonal antibody (Dako) recognising CD31 (platelet/endothelial cell adhesion molecule; PECAM-1) was used for microvessel staining on 3 µm paraffin embedded sections using the alkaline phosphatase/anti-alkaline phosphatase (APAAP) procedure. Sections were dewaxed, rehydrated and pre-digested with protease type XXIV for 20 min at 37^{o}C. JC70 (1:20 dilution) was applied at room temperature for 30 min and washed in TBS. Rabbit anti-mouse antibody (1:50 dilution) was applied for 30 min, followed by application of APAAP complex, 1 in 1, for 30 min. After washing in TBS, the previous two steps were repeated for 10 min each. The colour was developed by incubation with new fuchsin solution for 20 min. The sections were counterstained with haematoxylin, dehydrated and mounted. Normal species specific IgG was substituted for the primary antibody as the negative control.

3.3.5.3 VEGFR IHC

The phosphorylated form of VEGFR2 (pKDR) was assessed using monoclonal antibody 34a, raised against the Y1214 tyrosine residue of the KDR protein. The antibody specifically recognises the phosphorylated form of VEGFR2/KDR [176].

Sections were cut at 3 µm and were dewaxed and rehydrated in graded alcohol solutions. For heat-induced epitope retrieval, the sections were placed in citrate buffer (1:10 dilution, pH 7.2) and heated at 120^{o}C for 3 x 5 min. Endogenous peroxidase activity was neutralised using peroxidase block for 5 min. Non-specific binding was blocked by preincubation with Novocastra Protein Block for 5 min at room temperature (Novocastra Laboratories Ltd). Slides were then

incubated with the primary antibody overnight (1:2 dilution). The slides were washed with PBS (2 x 5 min) and then incubated with post-primary block (to enhance penetration of the subsequent polymer reagent) for 30 min at room temperature (Novocastra Laboratories Ltd). The slides were then washed with PBS for 2 x 5 min and incubated with NovoLink polymer for 30 min at room temperature (Novocastra Laboratories Ltd). The polymer recognises mouse and rabbit immunoglobulins and detects any tissue-bound primary antibody. After extensive washing with PBS (2 x 5 min), the colour reaction was developed in 3,3'-diaminobenzidine (DAB) for 5 min. The sections were then counterstained with haematoxylin, dehydrated and mounted. Normal species specific IgG was substituted for the primary antibody as the negative control.

Staining was quantified by determining the percentage of cancer cells with cytoplasmic or nuclear pKDR reactivity in all fields of the tissue sample. The final score was the median value for all fields.

3.3.5.4 Assessment of standard and activated vascular density

For assessing CD31 standard vascular density (sVD) and β_3-Integrin-expressing vessel density, the sections were first scanned at low power and the area of the highest vascularisation was chosen along the invading tumour front (adjacent to normal tissue; designated as t1-area) for vessel counting at x200 magnification. Vessels with a clearly defined lumen or well defined linear vessel shape, but not single endothelial cells were included for microvessel counting. The final vascular density was the mean of the vessel counts obtained in these fields. sVD was classified as either high or low dependent on whether the value was greater than (high) or less than (low) the median value for all specimens.

In addition to measuring the sVD at the tumour periphery, a previously described method to assess the decline of VD while moving from peripheral to inner tumour areas was used [177]. This involves vessel counting in three consecutive x200 fields, starting from the tumour tissue adjacent to normal tissue (t1 field; tumour periphery), and moving the optical field towards the tumour

centre twice (t2 and t3 fields; called intermediate and inner tumour area, respectively). These 3 fields (t1-3) were used to calculate a mean VD for the tumour.

Vascular survival ability (VSA) (FIGURE 25) was calculated by comparing the mean VD of the t2 and t3 fields to VD in the t1 field. Means that were greater than 50% of the t1 VD were classified as having high VSA. "Edvin" (Edge versus Inner) scores were also calculated for specimens [3]. This involved classifying tumours according to whether they had high or low sVD and VSA (TABLE 2).

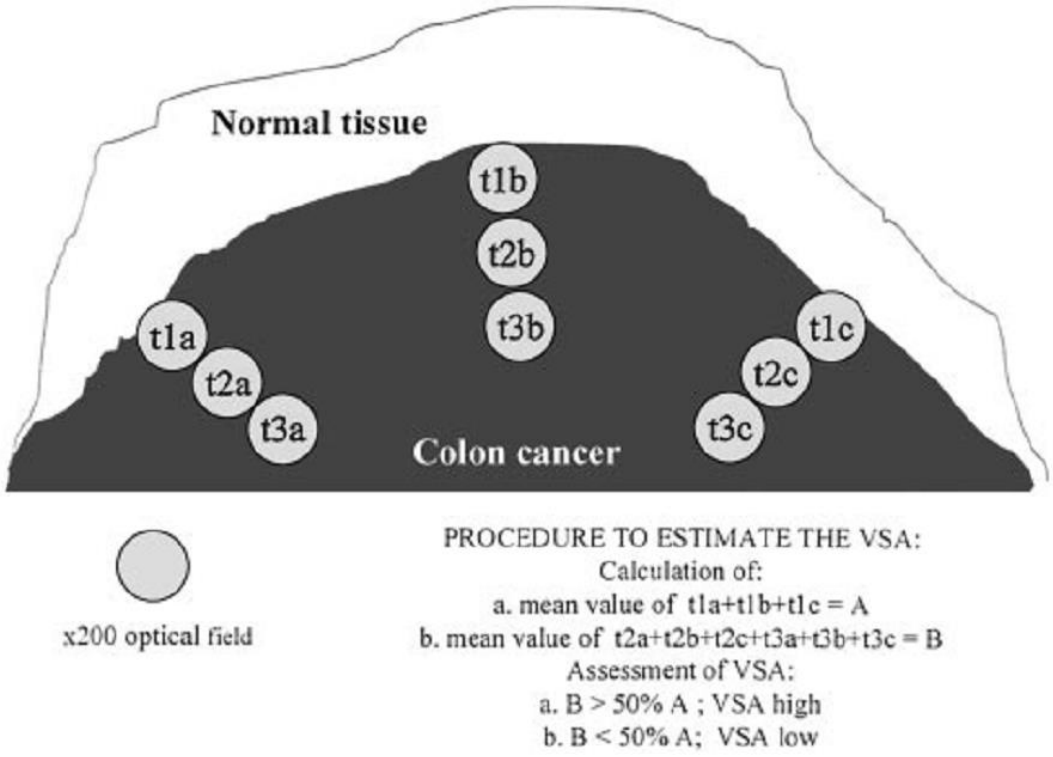


Figure 25: Process of calculating vascular survival ability (VSA). Image reproduced with permission of reference [3]

Table 2: Calculation of "Edvin" score

sVD	VSA	"Edvin" Score
Low	Low	1
Low	High	2
High	Low	3
High	High	4

3.3.5.5 Histological staging and grading

Tumour specimens also underwent routine histological analysis for stage and grade via the clinical pathology department. These results were acquired from the hospital intranet.

3.3.6 Image Analysis

All patient scans were anonymised and archived in a research database.

3.3.6.1 SPECT-CT analysis

All SPECT-CT analysis was performed on a Hermes workstation. The SPECT-CTs were fused and ROIs were drawn around the tumour on contiguous slices. ROIs were drawn combining information from both the SPECT and CT components of the scan. The individual ROIs were then combined to create a volume of interest (VOI) of the whole tumour.

VOIs drawn on the SPECT images generated several descriptors for the uptake in the tumour based upon individual voxels in the tumour. These were the mean number of counts, maximum number of counts, median number of counts and the geometric mean of counts. As might be expected, these variables correlated well with each other (Figure 26). Of these parameters, maximum number of counts per voxel was used for characterisation of tumour uptake, as it is relatively insensitive to the accuracy of drawn tumour volumes. It is also most analogous to SUVmax, which is the parameter most commonly used for assessing uptake of PET tracers.

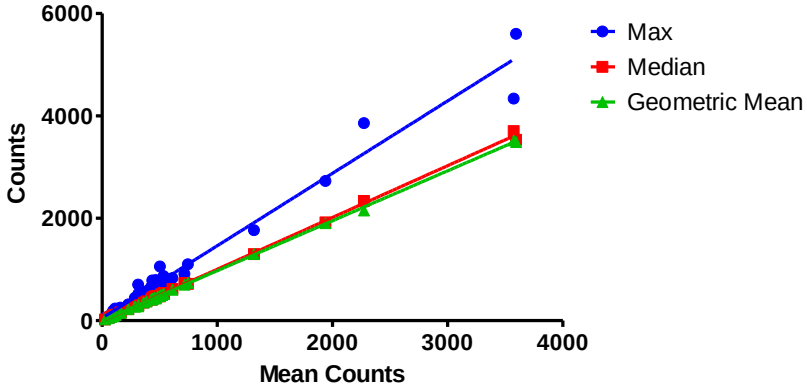


Figure 26: Comparison of different methods of assessing ^{99m}Tc-maraciclatide uptake within tumours. Correlation with mean counts demonstrates strong correlations with maximum number of counts per voxel (Max) (r=0.99, P<0.0001), median number of counts (r=1.0, P<0.0001), and the geometric mean (the nth root of the product of the numbers) of counts (r=1.00, P<0.0001).

VOIs were also created for background uptake within the body. This was generated by drawing VOIs over the gluteal muscles and subcutaneous fat contralateral to the side of the tumour. Both tissue types correlated well with each other (FIGURE 27), with muscle uptake slightly higher than fat uptake. This may have been due to the closer proximity of muscle to scatter from intra-abdominal organs, such as bowel and kidneys, which had marked uptake of ^{99m}Tc-maraciclatide. Overall background uptake was then calculated by taking the mean of average fat and muscle uptake. Overall tumour uptake was then calculated as a ratio of maximum tumour uptake to the mean of background uptake (T:B).

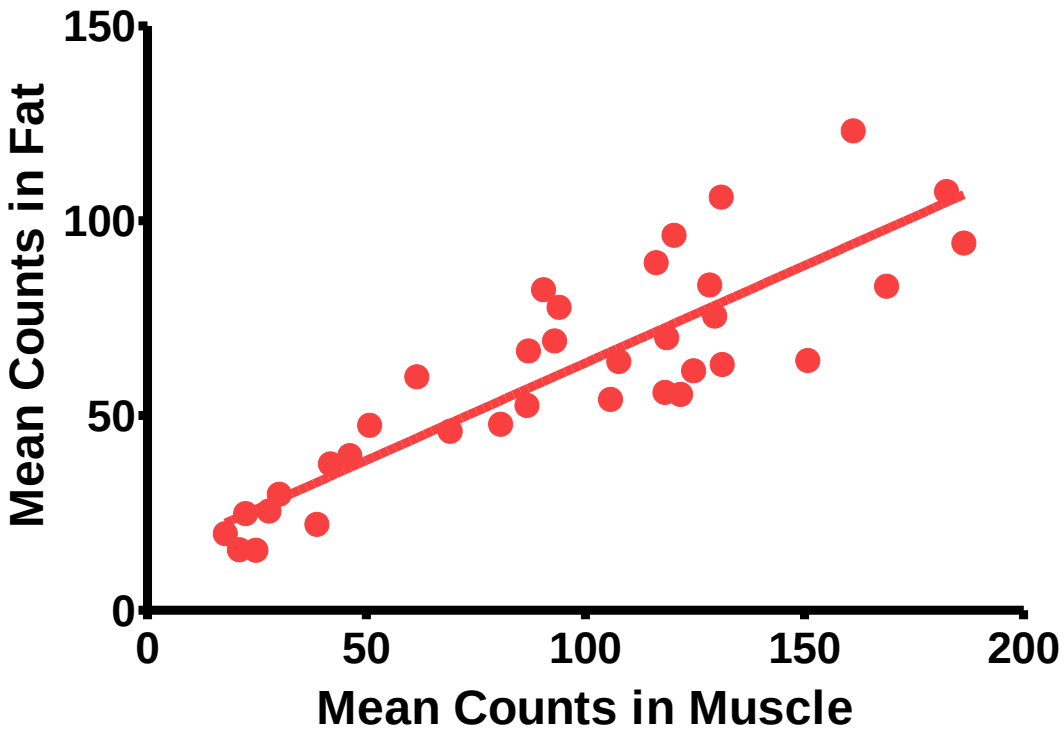


Figure 27: Comparison of mean number of counts in muscle and fat with ^{99m}Tc-maraciclatide imaging. There is a strong correlation (r=0.96, P<0.0001)

3.3.6.2 Volume analysis

Tumour volumes were determined by measuring the anteroposterior (a), craniocaudal (b) and lateral (c) dimensions of the tumour on the CT component of the SPECT-CT. These measurements were applied to the formula of an ellipsoid to calculate volume: $volume = \frac{4}{3}\pi\ (a \times b \times c)^3$.

3.3.7 Statistics

All statistical analyses were performed using Prism version 5.04 (GraphPad Software). Data points are expressed as means, and error bars, unless otherwise stated, are standard errors of the mean. Analyses performed to compare mean values of groups were either two-tailed t-tests or one-way analysis of variances (ANOVAs). All datasets were found to be normal, therefore only parametric statistical tests were performed. Pearson product-moment correlation coefficients were used to determine correlations. *P*-values of <0.05 are considered statistically significant.

3.4 Results

3.4.1 Patient demographics

Enrolment of patients occurred between October 2009 and December 2012. During this period 35 patients were recruited (see Tables 3-5). 20 were male and 15 were female with age ranging between 46 and 82 with a mean of 66 years. Two patients did not proceed to surgical resection of tumours. Of these, one had a preceding biopsy which was used for histological analysis. The other patient underwent trial scans, however no tissue sample was available and therefore this patient could not be included in the primary endpoint analyses.

3.4.2 Histology

Fifteen patients had colorectal cancer (Table 3), 10 patients had breast cancer (Table 4) and 10 patients had renal tumours (Table 5). Of note, one patient with breast cancer had bilateral breast tumours and within the renal tumour group, one tumour was an oncocytoma, and another was a metanephric adenoma. None of the patients recruited had metastases apparent on pre-enrolment clinical imaging.

Table 3: Patients with colorectal cancer.

Patient number	Age	Sex	Tumour site	Tumour type	TN-stage	Dukes Stage	Grade	Tumour Volume (cm^3)
1	63	M	Caecum	Adenocarcinoma	T3 N0	B	2	50
2	61	M	Rectum	Adenocarcinoma	T3a N0	B	2	9
3	62	M	Ileocolic anastomosis	Adenocarcinoma	T4 N0	C1	3	13
4	69	M	Sigmoid Colon	Adenocarcinoma	T4 N0	B	3	3
5	59	M	Rectum	Adenocarcinoma	T2 N0	A	1-2	13
6	68	F	Splenic flexure	Mucinous Adenocarcinoma	T4b N2	C2	3	113
7	66	M	Rectum	Adenocarcinoma	T3 N0	B	2	21
8	69	M	Caecum	Adenocarcinoma	T3 N1	C1	2	36
9	73	M	Caecum	Adenocarcinoma	T4b N1	C1	2	9
10	81	F	Caecum	Adenocarcinoma	T4 N0	B	3	57
11	71	F	Sigmoid Colon	Adenocarcinoma	T3 N0	B	2	21
14	77	M	Ascending Colon	Adenocarcinoma	T4 N1	C1	2	12
15	72	M	Transverse Colon	Adenocarcinoma	T4b N0	B	2	18
17	62	M	Sigmoid Colon	Adenocarcinoma	T4b N1	C1	2	19
20	68	M	Caecum	Adenocarcinoma	T4 N2	C1	3	16

Table 4: Patients with breast cancer. HER-2 is human epithelial growth factor receptor 2, ER is oestrogen receptor, PR is progesterone receptor. Patient 16 did not undergo tumour resection, so full histological analysis was not available.

Patient number	Age	Sex	Tumour type	TN-stage	Grade	Receptor status			Tumour Volume (ml)
						HER-2	ER	PR	
12	46	F	Mixed Lobular and Ductal	T3 N1	2	2+	8/8	8/8	14
13	53	F	Ductal	T2 N0	2	0	8/8	7/8	8
16	50	F							1
18	72	F	Ductal with Basal features	T2 N1a	3	0	0/8	0/8	13
19	45	F	Ductal	T1c N1a	2	2+	7/8	0/8	3
21	72	F	Ductal	T1c Nx	3	0	0/8	0/8	2
25	52	F	Ductal	T1c N0	3	3+	7/8	0/8	1
28	76	F	Ductal (left breast)	T1c N0	3	0	7/8	0/8	1
28	76	F	Ductal (right breast)	T1c N0	2	2+	8/8	7/8	1
29	48	F	Mixed Lobular and Tubular	T2 N1a	2	0	4/8	8/8	14
30	53	F	Lobular	T2 N2a	2	2+	0/8	0/8	2

Table 5: Patients with renal tumours. Patient 27 did not undergo tumour resection and was excluded from the comparative analysis.

Patient number	Age	Sex	Tumour type	TN-stage	Grade	Tumour Volume (ml)
22	64	F	Clear cell RCC	T3b N0	3	248
23	78	M	Clear cell RCC	T1a N0	2	13
24	52	M	Metanephric adenoma			17
26	76	M	Clear cell RCC	T1a N0	3	34
27	86	M				18
31	71	M	Papillary RCC	T2 N0	3	125
32	82	M	Chromophobe RCC	T1b N0	3	34
33	80	M	Papillary RCC	T2 N0	2	666
34	67	M	Papillary RCC	T1a N0	3	10
35	49	F	Oncocytoma			11

3.4.3 Imaging Characteristics

Visualisation of tumours on SPECT alone was variable between the different tumour groups. Breast cancers were very easy to detect on the background of breast fat and glandular tissue (Figure 28 A and B). Renal cancers were demonstrated as relatively photopaenic regions within renal parenchyma, as the kidney had high levels of uptake from renal excretion of the tracer (Figure 29). Uptake in the renal tumours was, however, greater than adjacent perinephric fat, which facilitated detection. Colorectal cancers were generally difficult to discern due to the high

levels of uptake within normal small and large bowel (FIGURE 28 C-F). Delineation of colorectal tumours was predominantly based upon CT morphology rather than SPECT appearances.

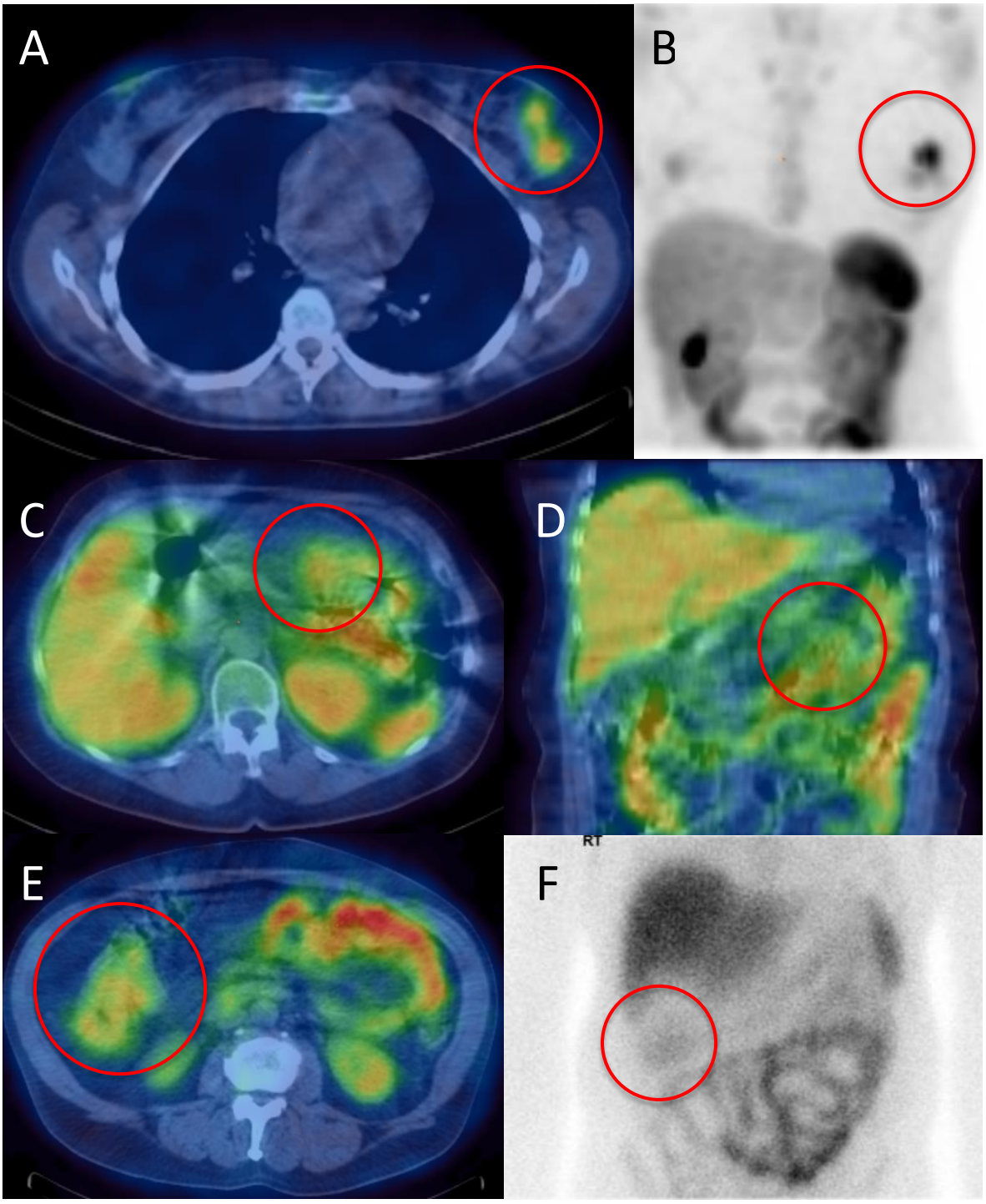


Figure 29: Examples of tumours (red circles) imaged with ^{99m}Tc-maraciclatide. Axial SPECT-CT (**A**) and maximum intensity projection (MIP) (**B**) images of a patient with breast cancer demonstrating an easily visualised bilobed cancer in the left breast. Also note physiological uptake within the nipples and gallbladder. Axial (**C**) and coronal (**D**) SPECT-CT images of a patient with a transverse colon cancer. The images demonstrate prominent bowel uptake, which makes delineation of the tumour difficult. Fused axial SPECT-CT (**E**) and planar images (**F**) of a patient with a caecal tumour performed 1h post-injection, demonstrating the tumour on the right side and prominent bowel uptake in the abdomen.

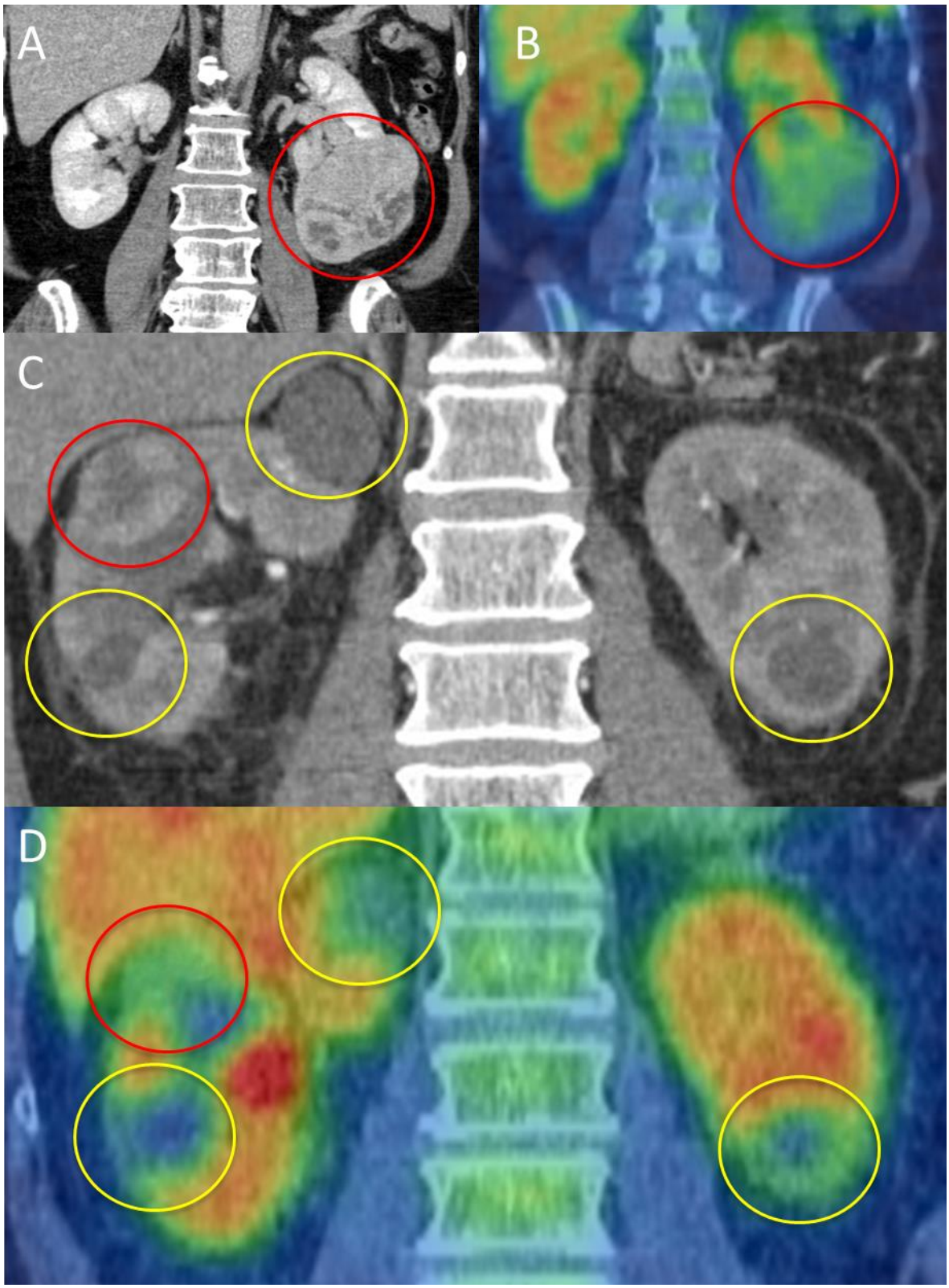


Figure 29: Exemplar scans of patients with renal tumours (red circles) imaged with ^{99m}Tc-maraciclatide. Coronal contrast-enhanced CT (**A**) and SPECT-CT (**B**) images of a left renal tumour. The contrast-enhanced CT demonstrates necrotic regions within the inferior aspect of the tumour which has decreased uptake relative to the rest of the tumour on the SPECT-CT. The main bulk of the tumour also has heterogeneous uptake within it. Coronal contrast-enhanced CT (**C**) and SPECT-CT (**D**) images of a right renal tumour. The tumour has decreased uptake within it relative to the renal parenchyma, however more than background and simple renal cysts (yellow circles) which are demonstrated as photopaenic regions within the kidneys.

Overall tumour uptake did not correlate with tumour volume (FIGURE 30A), however, a significant correlation was demonstrated when breast cancers were analysed separately (FIGURE 30B)

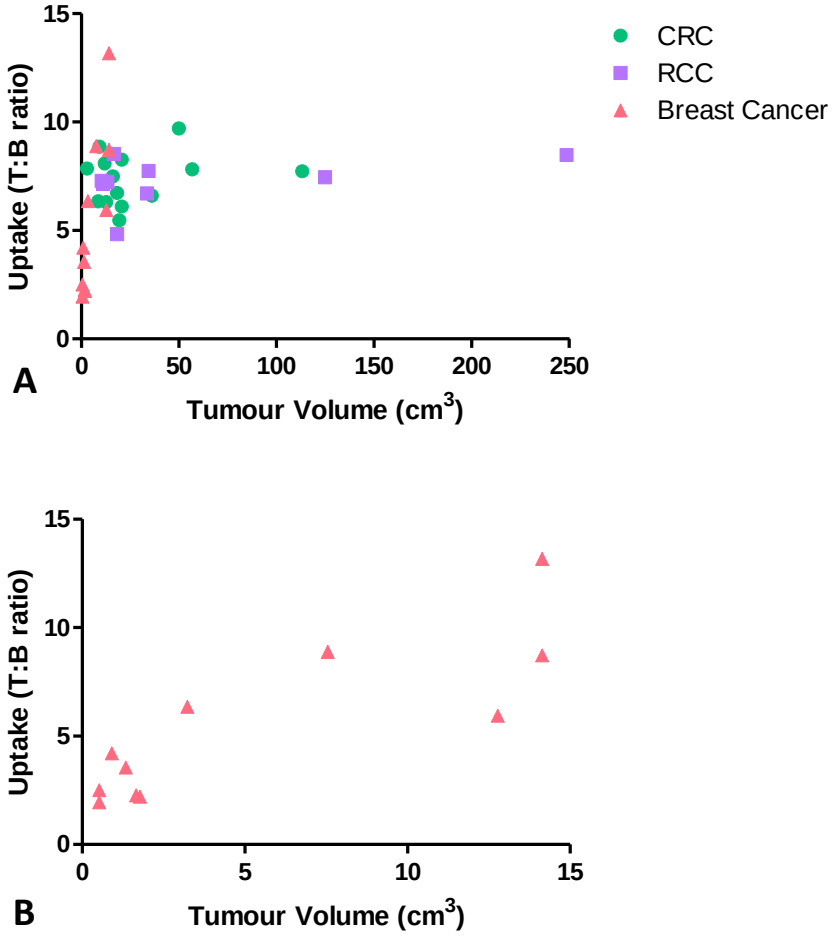


Figure 31: Comparison of uptake of ^{99m}Tc-maraciclatide with tumour volume. There is no correlation (r=0.28, P=0.1) when all tumours are compared together (**A**). When breast cancers are compared independently (**B**) there is a significant correlation (r=0.84, P=0.001).

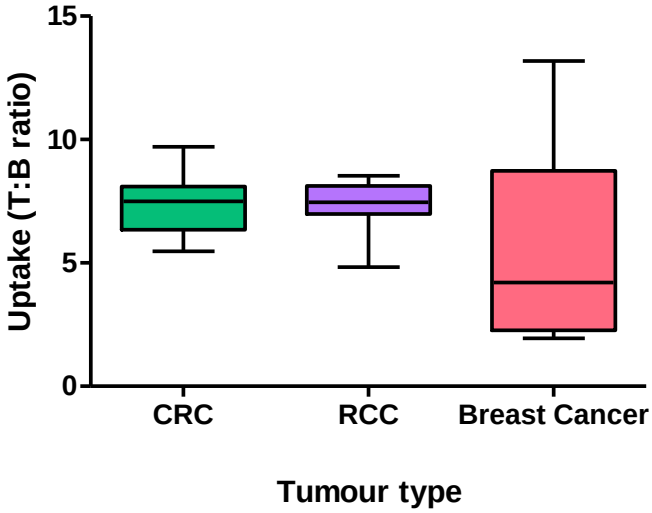


Figure 32: Uptake of ^{99m}Tc-maraciclatide in different tumour types. Uptake is measured as tumour:background ratio (T:B). There is no significant difference in uptake between the different tumour types. Whiskers represent the 5-95% centile.

3.4.4 TUMOUR SPECIFIC UPTAKE

Overall there was no statistically significant difference in mean uptake between the different tumour types. However, it appears that breast cancers tended to have a lower mean and there was greater variation in range of uptake in breast cancers, in comparison to renal and colorectal tumours (FIGURE 31). Similarly, though there was no statistically significant difference in uptake demonstrated between types, stages and grades of the tumours imaged (FIGURE 32), the breast cancers appeared to have variation in uptake dependent on histological subtype, T-stage, Grade and progesterone receptor status.

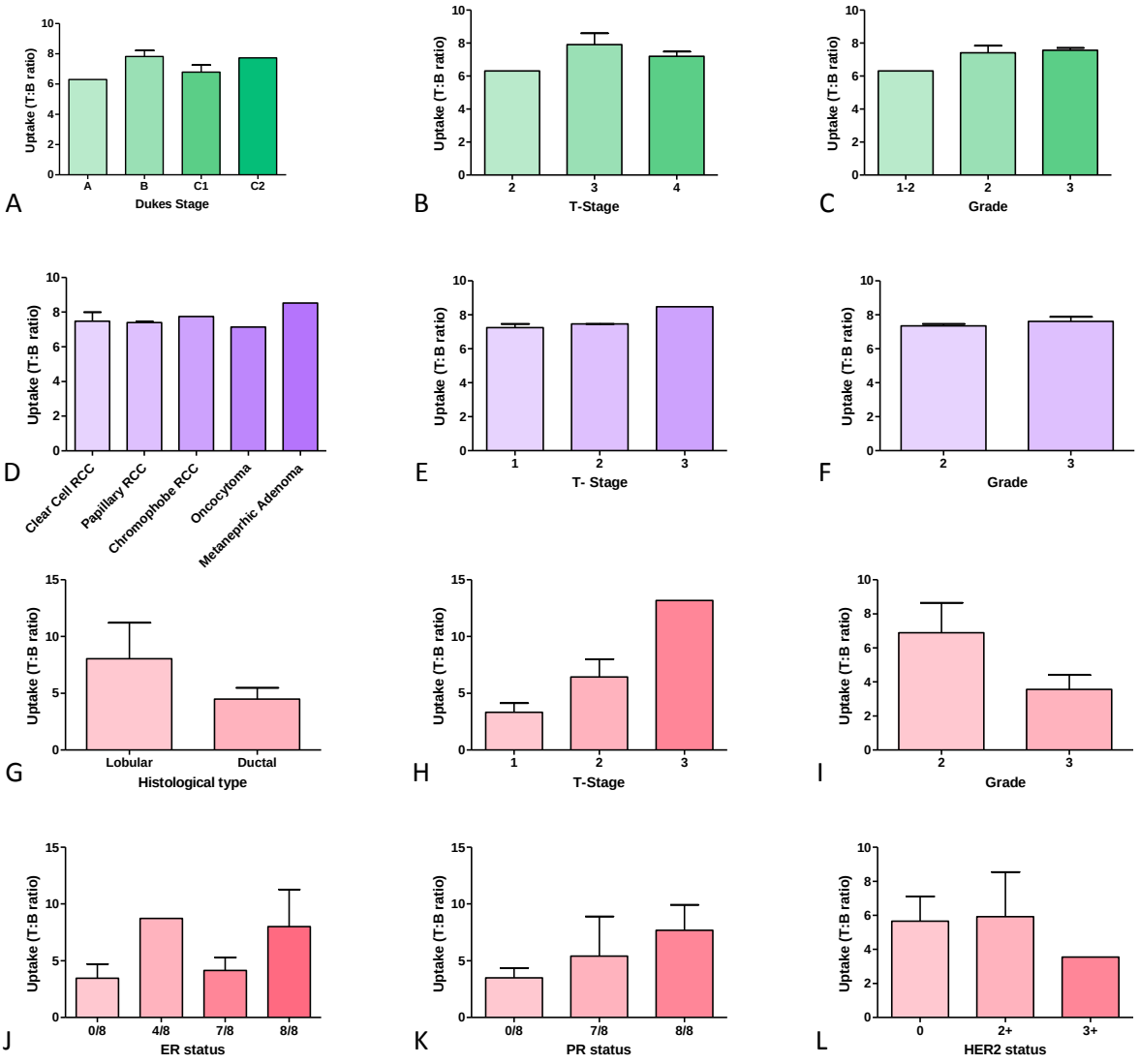


Figure 33: Comparison of uptake of ^{99m}Tc-maraciclatide in tumours of different stage and grade. **A**-**C** are colorectal cancers. **D**-**F** are renal tumours, with **E** and **F** only reflecting uptake in RCCs. **G**-**L** are breast cancers. **J**-**L** are comparisons with receptor status, ER= oestrogen receptor, PR= progesterone receptor, HER2= human epidermal growth factor receptor 2. Bars not showing error bars (SEM) represent ≤2 subjects.

3.4.5 Comparison with angiogenic markers

3.4.5.1 CD31

Standard VD, which is the vessel density at the tumours leading edge, was determined for every tumour. In addition, a mean VD was calculated, by taking the average of VD from fields at the edge and interior of the tumour. Figure 33 demonstrates examples of CD31 staining in colorectal tumours, used for calculation of VD.

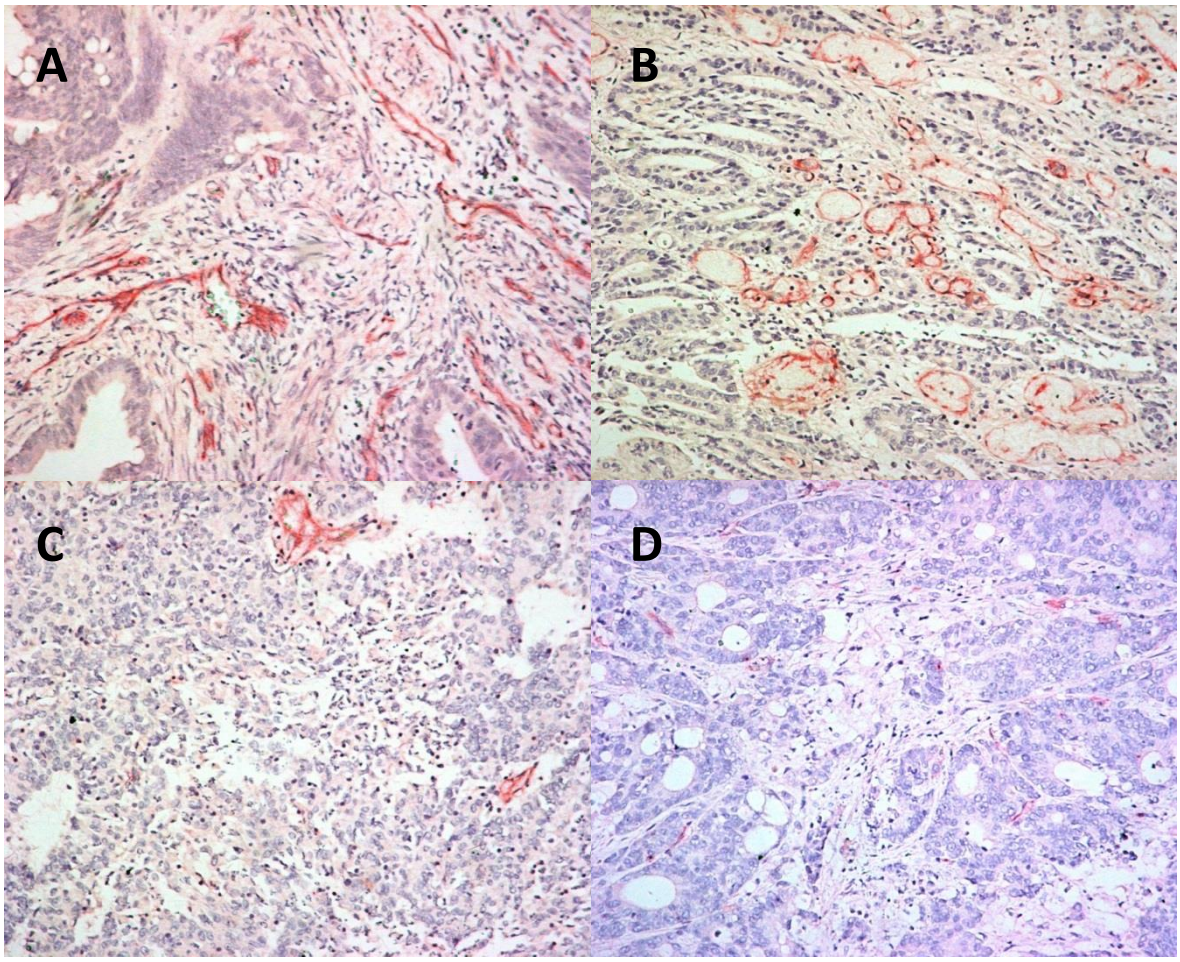


Figure 34: CD31 immunohistochemistry of colorectal tumours. **A** and **B** are tumours with high VD, in comparison to **C** and **D** which have low VD. Images provided by Michael Koukourakis.

Uptake of ^{99m}Tc-maraciclatide did not correlate with CD31 VD when compared with either standard VD or mean VD for either individual tumour groups or for all tumours combined (Figure

34). When considering all tumours together *r*=-0.08 (*P*=0.64) for standard VD and *r*=-0.17 (*P*=0.35) for mean VD.

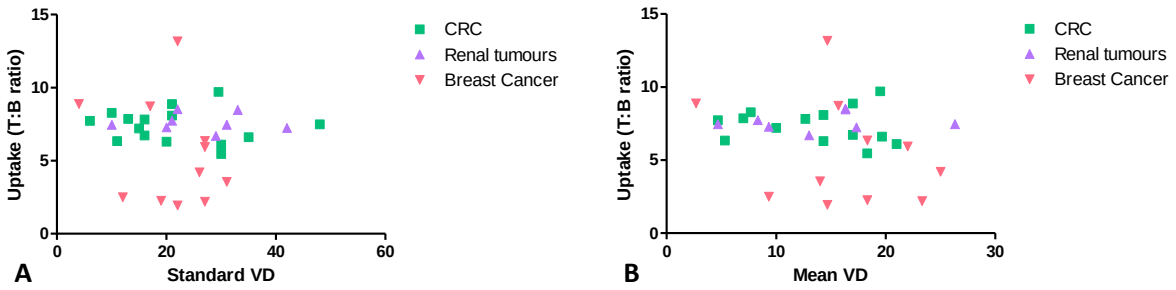


Figure 35: Comparison of ^{99m}Tc-maraciclatide uptake with CD31 standard (**A**) and mean (**B**) vessel density (VD). There is no evidence of a correlation in either individual tumour groups or all tumours combined. For standard VD when combining all tumours together, *r*=-0.08, *P*=0.64

The three vascular density measures (t1-3) were also used to calculate vascular survival ability (VSA) and "Edvin" scores. No significant difference in uptake was demonstrated for low versus high VSA tumours and between different Edvin score tumours. This was the case for all tumour types (FIGURE 35) and when each tumour type was assessed individually.

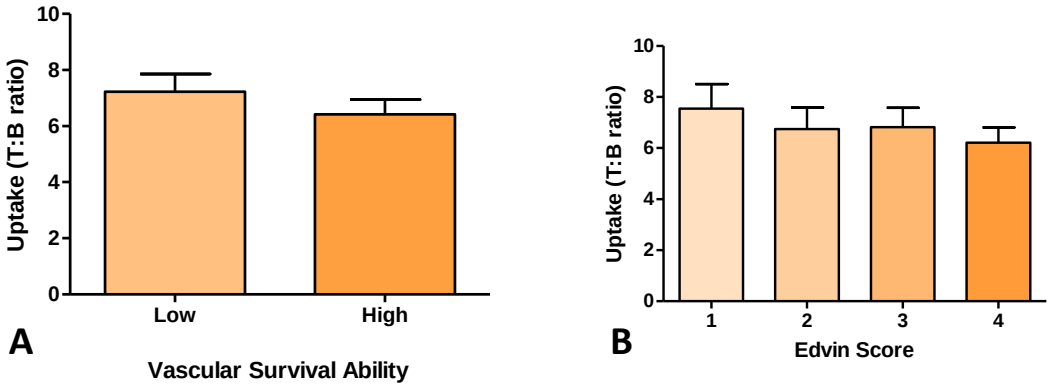


Figure 36: Comparison of VSA (**A**) and "Edvin" score (**B**) with uptake of ^{99m}Tc-maraciclatide. There is no evidence of a significant difference between groups. Error bars represent SEM.

3.4.5.2 VEGFR expression

The presence and extent of phosphorylated VEGFR2 (pKDR) in the cytoplasm (pKDRc) and the nucleus (pKDRn) was determined using IHC (FIGURE 36). This was compared with uptake of ^{99m}Tc-maraciclatide in the tumours (FIGURE 37). There was no correlation between uptake and expression of pKDRc (r=-0.23, P=0.19) or pKDRn (r=0.16, P=0.40) for all tumours combined, and when comparing individual tumour groups separately.

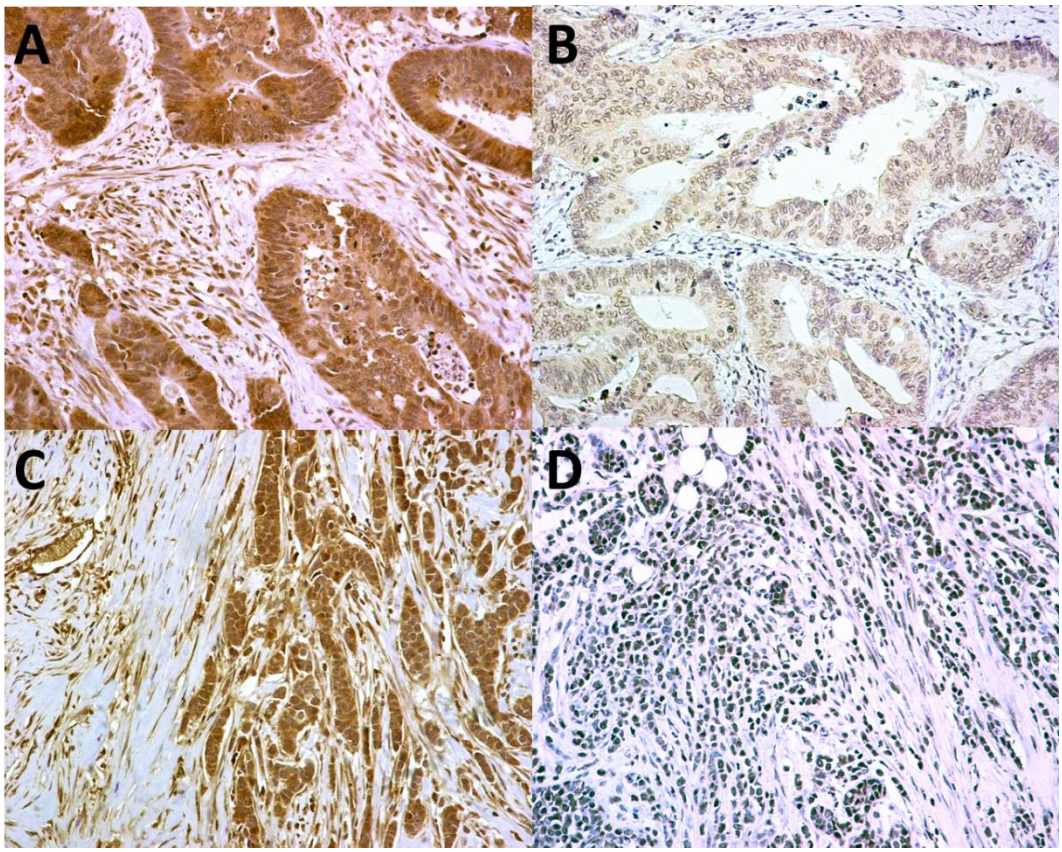


Figure 37: Examples of pKDR staining of tumour sections. High (**A**) and low (**B**) pKDR expression in colorectal cancer. High (**C**) and (**D**) low expression in breast cancer. Images provided by Michael Koukourakis.

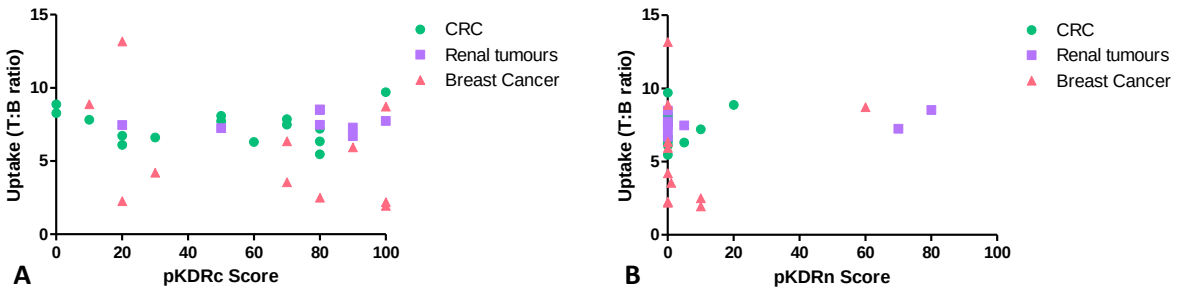


Figure 38: Comparison of pKDR staining with ^{99m}Tc-maraciclatide uptake in tumours. There is no evidence of correlation for individual tumour groups or for all tumours combined. PKDRc (**A**) and pKDRn (**B**) denote cytoplasmic and nuclear expression, respectively.

3.4.5.3 β_3 Integrin

IHC of the β_3 integrin subunit was performed and analysed to determine vascular density using a scoring system similar to that used for conventional vascular density scoring using CD31 (FIGURE 38). This involved generating a score for standard VD (for the invading tumour edge) and mean VD (for the whole tumour).

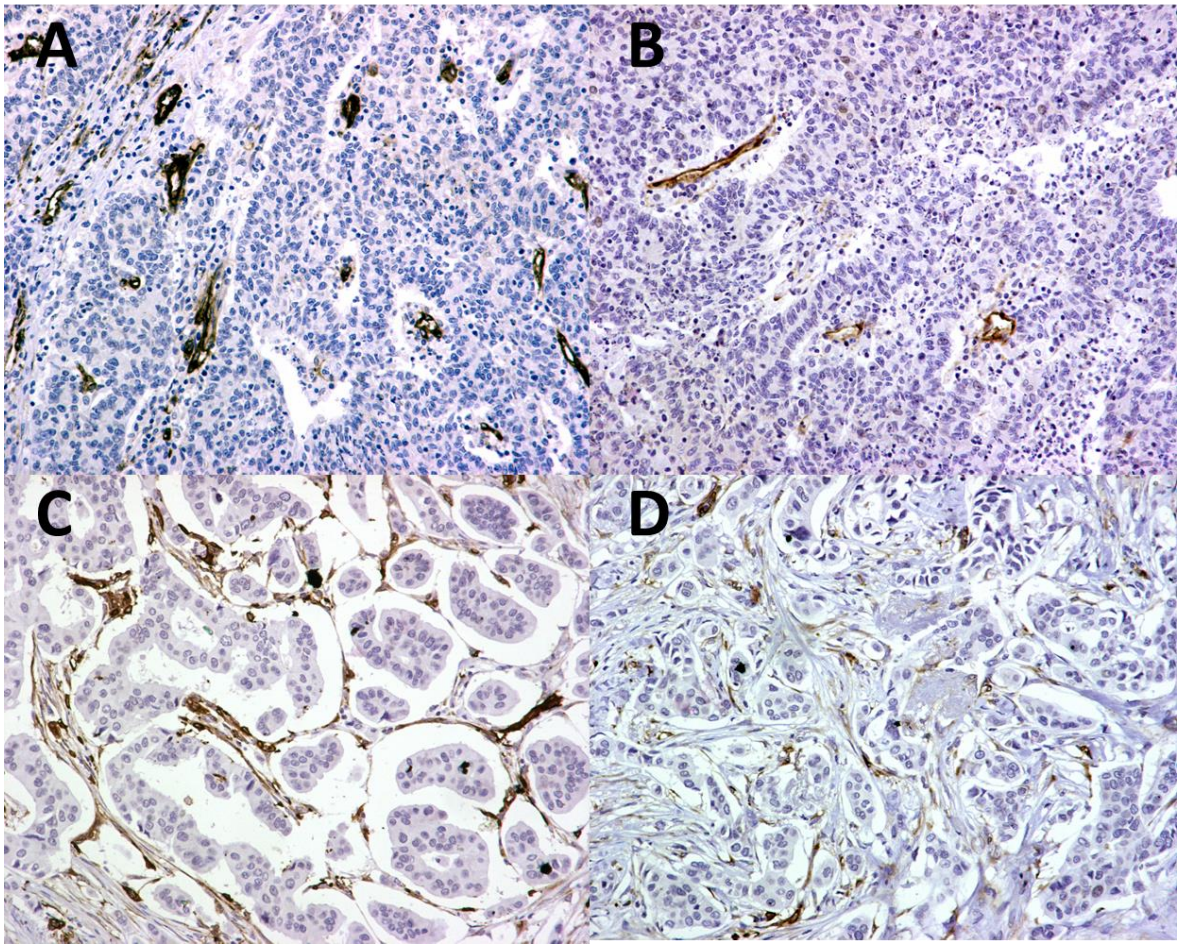


Figure 39: Examples of β_3 integrin staining in tumour sections. High (**A**) and low (**B**) VD in colorectal cancer and high (**C**) and (**D**) low VD in breast cancer. The staining is localised predominantly in blood vessels. Images provided by Michael Koukourakis.

Comparison of β_3 integrin VD with CD31 VD did not demonstrate a significant correlation either with standard (r=0.23, P=0.20) or mean VD (r=0.22, P=0.20) measurements except in colorectal tumours (FIGURE 39).

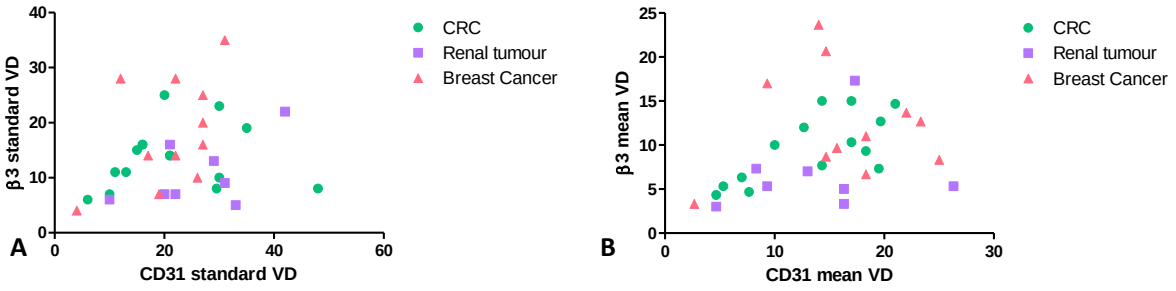


Figure 40: Comparison of β_3 integrin and CD31 standard (**A**) and mean (**B**) VD. There is no correlation for all tumour groups combined or in individual tumour groups except for mean VD values for colorectal cancers where *r*=0.69 (*P*=0.006)

Comparison between β_3 integrin standard VD and CD31 standard VD with pKDR also did not demonstrate a correlation (FIGURE 40) in combined tumours and in individual tumour groups.

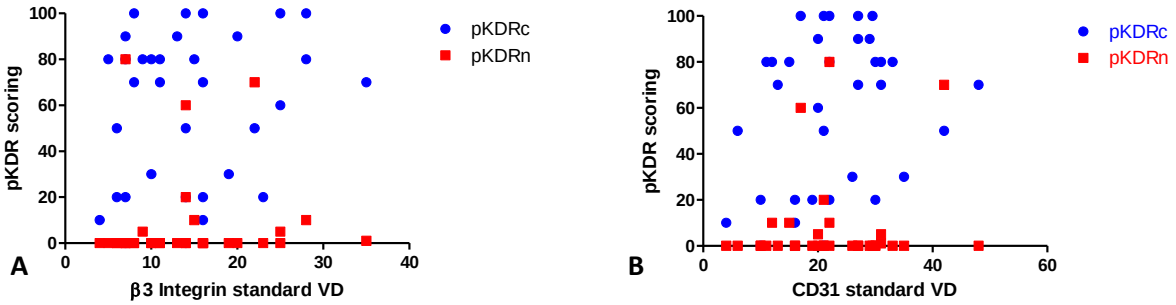


Figure 41: Comparison of standard VD of β3 integrin (**A**) and CD31 (**B**) with pKDR. There is no correlation for individual tumour groups or all tumours combined.

β_3 integrin standard VD and mean VD were compared with uptake of ^{99m}Tc-maraciclatide in the tumours (FIGURE 41). There was a significant moderate negative correlation for both standard VD (*r*=-0.52, *P*=0.002) and mean VD (*r*=-0.52, *P*=0.002). This negative correlation was also visible within each of the tumour groups, however did not quite reach significance in any individual group (e.g. for colorectal tumours standard VD correlation: *r*=-0.47, *P*=0.08).

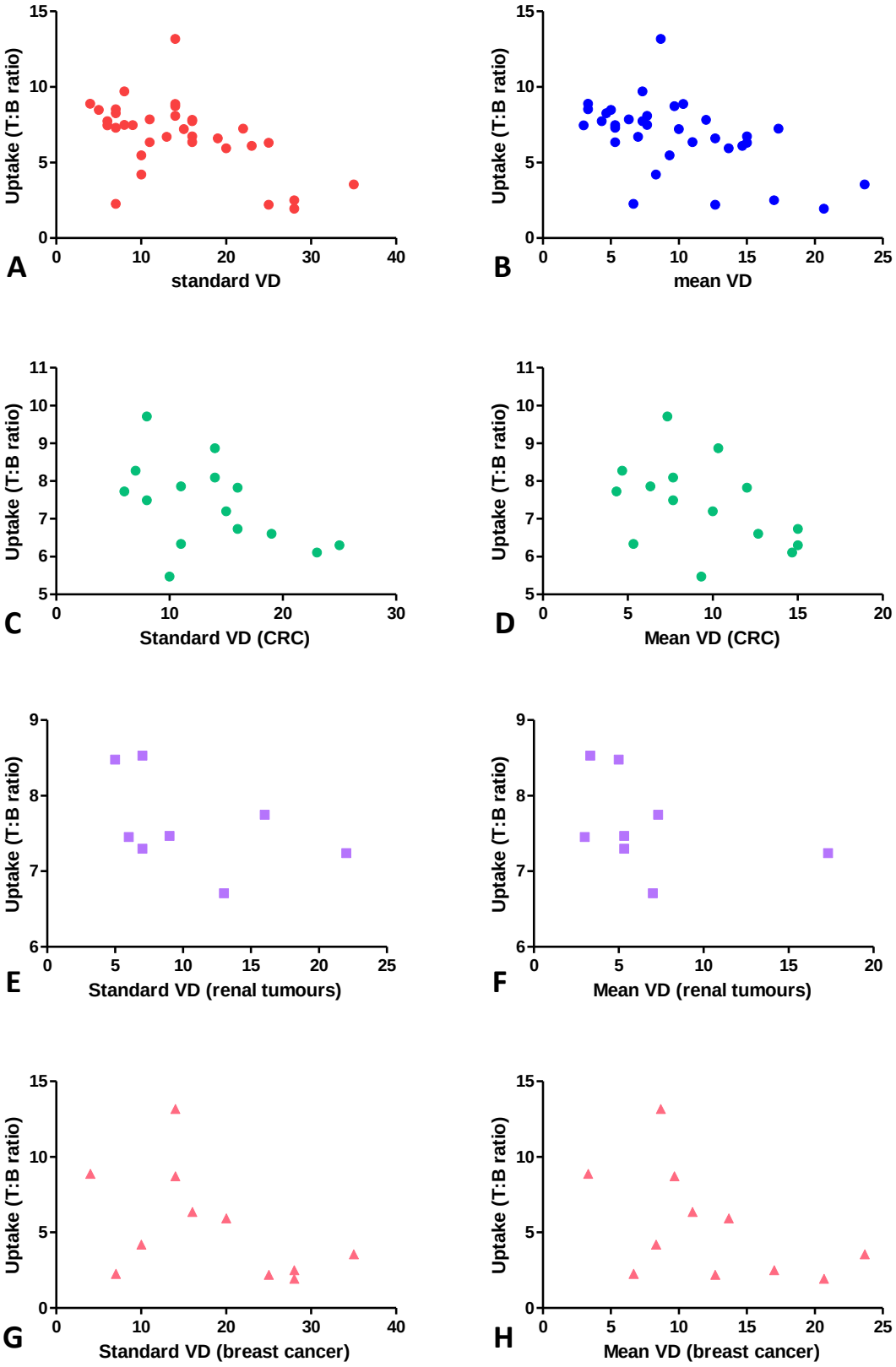


Figure 42: Comparison of ^{99m}Tc-maraciclatide uptake with β_3 integrin VD. **A**, **C**, **E** and **G** are comparisons with standard VD. **B**, **D**, **F** and **H** are comparisons with mean vessel density. **A** and **B** are all tumours combined, **C** and **D** are colorectal tumours, **E** and **F** are renal tumours, and **G** and **H** are breast cancers.

3.5 Discussion

Limited clinical evaluation of RGD-based radionuclide imaging agents has been conducted to date. ^{99m}Tc-maraciclatide is a SPECT-based RGD imaging agent developed by GE Healthcare. So far it has been tested in small clinical trials to assess safety, pharmacokinetics and basic imaging characteristics. This study is the first to directly investigate the relationship of ^{99m}Tc-maraciclatide uptake with histological markers of angiogenesis.

3.5.1 Imaging Characteristics

As ^{99m}Tc-maraciclatide is a gamma emitter and detected by SPECT, it is not possible to calculate an absolute value for tumour uptake. Therefore a relative measure, comparison of uptake within the tumour to background, was used. Background uptake was described as the mean uptake in muscle and fat in the back and gluteal region contralateral to the tumour. For breast cancer, calculation of uptake by this method also provides a good estimation for the visibility of the tumour as it is surrounded by fat. However, for colorectal and renal tumours, the background activity within the abdomen is much greater than that of fat and muscle due to significant uptake in the kidneys and bowel. This makes assessment of colorectal tumours particularly demanding as the background bowel uptake can be hard to distinguish from uptake within the tumour itself.

Furthermore, delineation of colorectal tumours in unprepared patients on CT can be difficult, especially if the tumour is plaque-like rather than a discrete mass. Overall, characterisation of colorectal tumours with ^{99m}Tc-maraciclatide SPECT is challenging and may require further optimisation of technique (such as bowel preparation) if it is to be clinically useful. In comparison, renal tumours are relatively easy to assess as they form discrete masses which can be defined on CT. They can also be readily distinguished from the renal parenchyma on SPECT, appearing as a region of relative photopaenia.

Mean relative uptake of ^{99m}Tc-maraciclatide was similar for colorectal and renal tumours, whereas breast cancers appeared to have a lower mean uptake together with a greater range of

uptake values. The tumour size did not influence the level of tracer uptake when all results were combined. However, when breast cancers were analysed separately there was a significant correlation. The breast cancers overall were much smaller than renal and colorectal tumours. Therefore this result may indicate that there is correlation between uptake and size when tumours are small, however as they get larger this correlation is lost.

Uptake in renal and colorectal tumours appeared to be independent of the tumour type, stage and grade. In breast cancers there appeared to be an effect on uptake related to histological subtype, T-stage, grade and progesterone receptor status. These differences, however, were not statistically significant, which may result from insufficient numbers in each subgroup. A correlation with grade of tumours has been seen before when comparing tumour uptake of ^{18}[F]-galacto-RGD to grade of sarcomas [51]. In a small number of patients minimal uptake of ^{18}[F]-galacto-RGD was observed in low grade sarcomas, whereas high grade sarcomas showed significant uptake of tracer. This may have partly been due to expression of $\alpha_v\beta_3$ on tumour cells themselves rather than on vessels and could be explained by the role of $\alpha_v\beta_3$ expression in cell migration, invasion and metastasis. Furthermore, higher grade tumours may have more vessels.

The uptake characteristics of breast cancers appear to be different to those of renal and colorectal tumours. As already suggested this may relate to the fact that breast cancers were much smaller, and these differences are a reflection of difference in size rather than type of tumour. These differences may also partly relate to the significant background activity within the abdomen which would lead to an artefactual increase in the overall uptake of the renal and colorectal tumours. This would also lead to decreased relative difference in uptake between the tumours. The differences seen between breast cancers and the abdominal tumours suggest that this may partly be the case.

3.5.2 Correlation with angiogenic markers

The assessment of conventional microvessel density (or standard VD) in tumours was performed through analysis of microscopic fields at the tumour edge. This measure is a reflection of tumour angiogenic activity (TAA), which is mainly controlled by angiogenic factors. In addition, a parameter known as vascular survival ability (VSA) was assessed by analysing the VD of regions deeper within the tumour. This measure, VSA, is intended to characterise maintenance of the vascular supply deep within a tumour through, for example, secretion of anti-apoptotic factors, in the face of environmental stresses such as hypoxia and acidity [178]. VSA and TAA describe different aspects of tumour vasculature and can be combined to create a scoring system characterising different "edvin" (edge vs inner) types (Table 2). This scoring system has been shown to have prognostic significance in several tumour types including breast and colorectal cancer [3, 179].

In this study there was no correlation between standard VD or mean VD with uptake of ^{99m}Tc-maraciclatide. These results are consistent with those of a previously reported study of 12 patients with breast cancer, in which ^{18}F-RGD-K5 uptake did not correlate with CD31 microvessel density (r=0.298, P=0.437) [168]. When comparing ^{99m}Tc-maraciclatide uptake to VSA and "edvin" scores there appeared to be a decrease in uptake with higher scores, however these observations were not statistically significant.

Phosphorylated VEGFR2 (pKDR) was also analysed in this study. PKDR is the activated form of VEGFR2, the expression of which has been shown to have prognostic significance and to relate to levels of VEGF and HIF1α in several cancers [180-182]. All tumours demonstrated a wide range of expression of pKDR, however no correlation was demonstrated between nuclear or cytoplasmic pKDR and ^{99m}Tc-maraciclatide uptake.

Surprisingly there was a significant negative correlation between β_3 integrin VD and uptake of ^{99m}Tc-maraciclatide. This was seen in all tumour types and was evident for both standard VD and

mean VD. This appears contradictory to previous evidence where uptake (measured by tumour: blood ratio) of ^{18}F-Galacto-RGD had a very strong correlation with $\alpha_v\beta_3$ staining intensity (r=0.94, P<0.0001) and VD (r=0.83, P<0.0001) [51]. The disparity between the two studies could be due to several differences in methodology, which will be discussed below.

In this study, uptake was compared with the β_3 integrin subunit rather than the whole $\alpha_v\beta_3$ receptor. It was not possible to evaluate $\alpha_v\beta_3$ receptor itself as all commercially available antibodies directed against it require fresh frozen tissue specimens. Only paraffin embedded specimens were available for this study. The β_3 subunit is also a component of $\alpha_{IIB}\beta_3$ integrin which is bound by ^{99m}Tc-maraciclatide with much lower affinity than $\alpha_v\beta_3$ [1]. Therefore, it is feasible that the presence of $\alpha_{IIB}\beta_3$ within the tumours could have confounded a correlation between ^{99m}Tc-maraciclatide uptake and β_3 levels. Against this, is the fact that $\alpha_{IIB}\beta_3$ is predominantly expressed on platelets, and would therefore not be expected to contribute significantly to VD score.

Another key difference between the studies is that ^{99m}Tc-maraciclatide and ^{18}F-Galacto-RGD have different binding affinities. ^{18}F-Galacto-RGD has greatest binding affinity for $\alpha_v\beta_3$. In contrast, ^{99m}Tc-maraciclatide has greater binding affinity for $\alpha_v\beta_5$ (Kd=0.1nM) compared to $\alpha_v\beta_3$ (Kd=0.5 nM). Therefore, $\alpha_v\beta_5$ levels, which were not measured, may have had a more significant effect on uptake of ^{99m}Tc-maraciclatide within the tumours than $\alpha_v\beta_3$. If this is the case, it suggests that $\alpha_v\beta_3$ and $\alpha_v\beta_5$ expression are inversely related to each other. Further work, is being performed at present to try and optimise β_5 IHC for assessment of β_5 status in tumours.

Correlation of histological parameters with uptake on imaging is also subject to sampling error. In this study histological sections were cut randomly from the tumour. The imaging showed, especially in larger tumours, that there was heterogeneity in uptake, which could be missed unless multiple sections are studied. This problem was circumvented in the study with ^{18}F-Galacto-RGD by obtaining histological samples from the region of the tumour with the highest

uptake of tracer. This was performed at the time of surgery, having evaluated imaging just before resection of the tumour.

Another potential reason for the negative correlation between β_3 VD and ^{99m}Tc-maraciclatide uptake may relate to differences in vascular permeability. Decreased $\alpha_v\beta_3$ has been demonstrated to increase vascular permeability by increasing sensitivity of endothelium to VEGF by upregulation of VEGFR2 [152]. Increased vascular permeability may lead to increased retention of tracer, therefore resulting in an inverse relationship between $\alpha_v\beta_3$ expression and ^{99m}Tc-maraciclatide uptake in tumours.

3.6 Conclusion

^{99m}Tc-maraciclatide demonstrates good uptake in colorectal cancers, renal tumours and breast cancer, though visualisation of colorectal tumours is problematic due to background uptake in the bowel. Uptake in colorectal and renal tumours is independent of size of the tumour and does not correlate with type, stage or grade of tumour. Breast cancers, possibly by virtue of their smaller size and position, demonstrate uptake that is proportional to size of tumour and may be affected by histological subtype, stage, grade and progesterone receptor status.

There is no evidence of correlation of ^{99m}Tc-maraciclatide uptake with standard vascular density measurements using CD31 staining. It does, however, demonstrate a significant negative correlation with β_3 integrin which potentially may result from the non-specific binding of ^{99m}Tc-maraciclatide. Further investigation is needed to understand the significance of this finding.

4 Imaging Response to Antiangiogenic Therapy

4.1 Introduction

The ability to guide an individual's cancer therapy based on the specific biology of their tumour is an ambition that molecular imaging may help realise. One particular focus for molecular imaging is in the arena of antiangiogenic therapies. This chapter examines the ability of 2 radionuclide angiogenesis imaging agents to detect response to antiangiogenic therapy.

4.1.1 Imaging to predict response

Imaging plays a daily role in guiding the management of patients with cancer especially in terms of whether to continue, change or abandon therapy. Imaging also has an evolving role in clinical trials to help select therapies for further development and investment. This is largely due to the heavy costs and long delays of using clinical endpoints, such as survival, to demonstrate efficacy of therapies. In addition, avoidance of potentially toxic therapy is beneficial to patients and may expedite the use of alternative options. These factors have generated a need for biomarkers that can act as surrogates for clinical endpoints.

4.1.1.1 RECIST

One popular imaging method of assessing tumours is to use the Response Evaluation Criteria in Solid Tumours (RECIST). This was originally published in 2000 [183] as a collaboration between the European Organisation for Research and Treatment of Cancer (EORTC) and the National Cancer Institutes (NCI) of the United States of America (USA) and Canada, and was revised in 2009 as version 1.1 [184]. It bases assessment of response on physical criteria such as the longest diameter of a tumour deposit, and then classifies the overall status of the patient into categories of complete response, partial response, stable disease and progressive disease. These criteria have been widely used and have been shown to predict progression free and overall survival in many cancers. However, increasingly exceptions are being observed and reported. Newer cancer therapies may be cytostatic, which despite leading to stable disease, rather than objective responses, may carry survival benefit. There are many examples of this including gastrointestinal

stromal tumours (GISTs) where patients live for long periods with stable disease [185] and hepatocellular carcinoma treated with chemoembolisation [186] or sorafenib [187]. In addition, the converse may be true, some tumours may display a response according to RECIST criteria without this translating into clinical benefit [188]. Further criticisms of RECIST include poor measurement consistency at different timepoints and between observers [189-191] and the use of categorical (qualitative) data which may magnify the effect of measurement variability [192]. It is evident that new strategies are needed for assessing tumour response beyond simple size criteria.

4.1.1.2 [^{18}F]FDG-PET response

With the advent of molecular imaging in the form of [^{18}F]-Fluorodeoxyglucose (FDG) PET, assessment of tumour response entered a new era. [^{18}F]FDG-PET uptake reflects glucose influx by cells and is related to the metabolic activity of tumours. This can be affected before size changes are detectable and can provide complementary information to anatomical imaging. [^{18}F]FDG-PET has proven value in several tumour types such as lymphoma [193], NSCLC [194], colorectal cancer [195] and breast cancer [196]. There is also evidence that uptake is related to the proliferative capacity of tumours and the number of viable cells [197, 198]. This together with the complex interplay of changes in glucose metabolism with therapy has led to increasing adoption of [^{18}F]FDG-PET in assessment of therapy. This is reflected in several published suggestions to incorporate PET criteria into formal assessment of therapy, for example the PERCIST guidelines [199].

4.1.2 Assessing antiangiogenic therapies

Imaging to assess antiangiogenic therapy poses challenges as this type of treatment may work by slowing tumour growth and preventing metastases. Furthermore, they may induce hypoxia within tumours. These effects could impact clinical outcome without necessarily affecting the physical dimensions or metabolic requirements of the tumour. In addition, many antiangiogenic therapies

have failed to show benefit in relatively unselected patients in phase III trials. This has fed into the paradigm of personalised medicine, suggesting that there are subsets of patients that may disproportionately benefit from antiangiogenic therapies. Consequently, there has been intense investigation into biomarkers that can predict and assess response to antiangiogenic therapies. Examples include physiologic changes such as hypertension; circulating markers in the blood such as tumour-associated proteins (e.g. VEGF, PlGF, sVEGFR), and endothelial cells; markers from the tumour tissue itself such as MVD and genetic profiles; and imaging biomarkers [200]. These have met with varying degrees of success, but all still need further study.

4.1.2.1 [^{18}F]FDG-PET

Several attempts have been made to use [^{18}F]FDG-PET to assess angiogenesis with conflicting reports. Some studies have demonstrated a correlation of uptake with markers such as CD105 [201], VEGF [202] and CD34 [203], whilst in others either no correlation or negative correlations were observed [201, 204, 205]. Uptake of [^{18}F]FDG-PET has also been compared with DCE-MRI and shown to have a good correlation with DCE-MRI parameters such as K_{ep} [206].

[^{18}F]FDG-PET has also been used in the assessment of response to antiangiogenic therapies. In a trial of erlotinib and bevacizumab in patients with NSCLC, changes in [^{18}F]FDG-PET uptake correlated with response, although this was not as robust as RECIST criteria and not as discriminatory as using perfusion PET ($H_2{}^{15}O$) or DCE-MRI [207]. In addition, it was not possible to determine the relative contribution of bevacizumab to changes in uptake compared to erlotinib. This has been a problem with other studies when assessing an antiangiogenic therapy in combination with another therapy, such as chemotherapy [208].

4.1.2.2 Dynamic imaging

Clearly assessing response of tumours to antiangiogenic therapy requires modalities that directly reflect the biology being modulated. Evidence for the use of dynamic perfusion techniques such as DCE-MRI and DCE-CT in a variety of tumour groups has been accumulating. Several DCE-MRI

parameters have been shown to decrease following monotherapy with a variety of antiangiogenic agents [69, 209, 210]. However, these have not all correlated with improved clinical outcome in patients [211]. One example is that of vatalanib (a VEGFR inhibitor), which demonstrated significant changes in DCE-MRI parameters in early phase trials [212], but did not translate into clinical benefit in a phase III trial [213]. DCE-MRI has also been used to assess response to chemotherapy as a monotherapy and in combination with antiangiogenic therapy. Breast cancer has been the most intensively investigated with variable results [214-216]. Unfortunately, as with the use of [^{18}F]FDG-PET in combination therapy, in cases where perfusion parameter changes have been identified, it has not been possible to differentiate the relative contributions of the therapies [217, 218]. DCE-CT, although not as intensively investigated as DCE-MRI, has also been used in the prediction of outcome [219], response to antiangiogenic treatment [220, 221] and to conventional chemotherapy and radiotherapy [222, 223] (FIGURE 42).

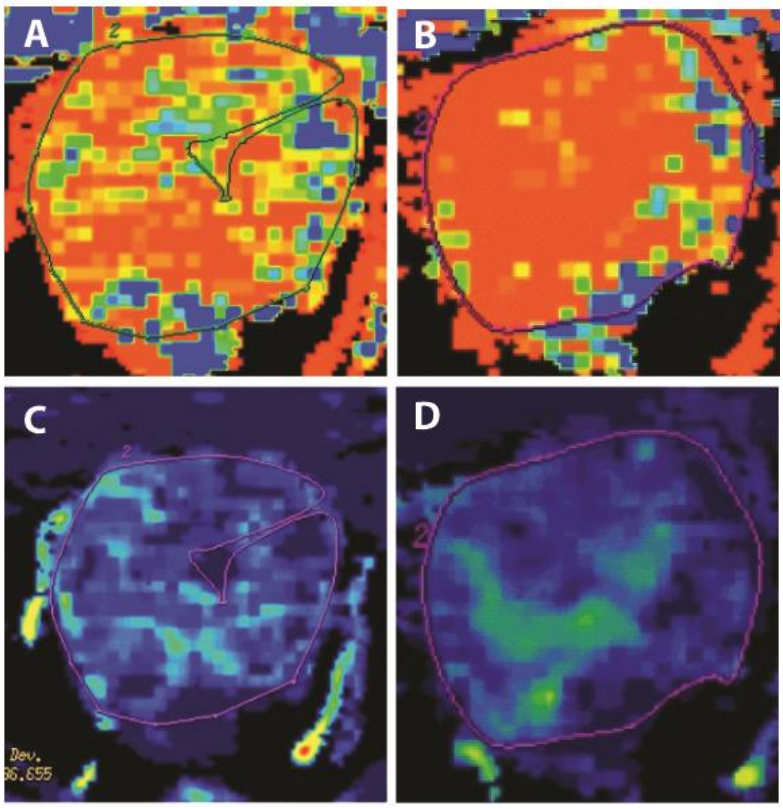


Figure 43 DCE-CT parameter maps showing response to therapy in a patient with a colorectal cancer. Panel **A** shows the mean transit time which globally decreases (from 6.3 sec to 4.0 sec) after chemoradiotherapy (**B**). This associated with a concomitant increase (from 118mL/min/100mL to 149mL/min/100mL) in blood flow between **D** (post-chemoradiotherapy) and **C** (pre-therapy). Images provided by Jamie Franklin.

4.1.2.3 Targeted imaging

In comparison with dynamic imaging modalities, targeted imaging is still in its infancy, with only a small number of tracers tested in clinical trials to date. Therefore, there is limited evidence for the use of targeted imaging agents in the assessment of antiangiogenic therapy. Most studies have been in preclinical models with only a small number of clinical trials to assess proof of concept.

4.1.2.3.1 Integrin Imaging

[^{18}F]-fluciclatide has been used in two studies to investigate the effects of antiangiogenic therapies on its uptake in mouse models of human cancer. The first used lung xenograft models to assess the effect of low-dose paclitaxel (a microtubule inhibitor) and ZD4190 (an anti-VEGFR2 tyrosine kinase inhibitor (TKI)) on uptake of [^{18}F]-fluciclatide [224]. It was shown that both drugs significantly decreased uptake of [^{18}F]-fluciclatide and that this corresponded to a decrease in MVD. In comparison, imaging with ^{14}C-FDG at the same time as [^{18}F]-fluciclatide showed no change in uptake, indicating that [^{18}F]-fluciclatide may be superior to [^{18}F]-FDG at monitoring antiangiogenic therapies. This supports results from a previous study where glucosamino ^{99m}Tc-D-c(RGDfK) was used to assess response to paclitaxel and showed similar reductions in uptake with therapy [225]. [^{18}F]-fluciclatide has also been used to assess response to sunitinib in a glioblastoma tumour model. A reduction in tumour uptake of tracer was seen as quickly as 2 days after initiation of therapy and was maintained over the course of 2 weeks of therapy [58]. This was also reflected in a decrease in MVD of the tumour specimens.

Another PET integrin imaging agent used for therapeutic monitoring is [^{64}Cu]DOTA-c(RGDfK). It was used to assess the effect of dasatinib (a TKI) on a glioblastoma xenograft model [226]. Dasatanib caused a significant dose-dependent reduction in uptake of the tracer which was not seen with [^{18}F]-FDG. [^{18}F]-FDG has also been compared to [^{18}F]-FPPRGD2 (a dimeric RGD radiotracer), which was used to image changes in xenografts after ZD4190 therapy [227]. The results of this study also showed a decrease in [^{18}F]-FPPRGD2 and [^{18}F]-FLT uptake over the first

few days of treatment, whereas there was no change in the uptake of [^{18}F]-FDG. These studies reinforce the potential for RGD agents in assessing therapeutic response which cannot be identified by using [^{18}F]-FDG-PET.

4.1.2.3.2 VEGF pathway imaging

4.1.2.3.2.1 VEGFR imaging

Imaging of the VEGF pathway for assessing antiangiogenic therapies has mainly focused on VEGF receptors. To date only a few preclinical studies have investigated efficacy. The effects of VEGFR TKIs on tumours have been investigated by two groups using single chain (sc) forms of VEGF labelled with ^{99m}Tc (^{99m}Tc-scVEGF). One group treated colorectal xenograft-bearing mice with pazopanib and showed a marked decrease (around 3-fold) in uptake after therapy despite observing no change in tumour size [228]. This fall in tumour uptake of ^{99m}Tc-scVEGF corresponded to a decrease in VEGFR2 and CD31 positive endothelial cells in tumour sections after 5 days of treatment. Another group used ^{99m}Tc-scVEGF in conjunction with sunitinib treatment of breast cancer xenografts [229]. Tracer uptake significantly decrease after 4 days mirrored by a decreased in VEGFR2 and CD31 positive endothelial cells. In a group of animals in which sunitinib had been discontinued for 3 days, uptake of the tracer increased back to control levels, concurrent with reestablishment of a dense vascular network, particularly at the tumour periphery. Such observations may provide an insight into the biology of endothelial cell recovery and help guide use of combined metronomic chemotherapy and antiangiogenic therapies [230].

Another VEGF receptor imaging tracer used for assessing therapeutic response is ^{99m}Tc-HYNIC-VEGF. Imaging with this probe was performed following administration of cyclophosphamide to a murine model of breast cancer. It was shown that tumour growth decreased with administration of both high dose therapy and low-dose metronomic therapy and that this was reflected in a reduction in tracer uptake [39]. ^{99m}Tc-HYNIC-VEGF has also been used with vatalanib (a VEGFR TKI) therapy in a glioma model [231]. Surprisingly treatment led to increased uptake of tracer

indicating raised levels of VEGFR. This correlated with increased MVD, K^{trans} on DCE-MRI and VEGF expression by western blot analysis.

VEGFR imaging has also been performed with microbubbles bound to an anti-VEGFR-2 antibody and used to detect response to an MMP inhibitor [232]. Optical methods have also been used with an anti-VEGFR2 antibody derivatised with an infrared dye to demonstrate changes following sunitinib therapy [233]. Both studies showed a decrease in uptake of the tracer in the treated groups.

4.1.2.3.2.2 VEGF Imaging

Very little preclinical research has been performed to investigate imaging VEGF to monitor response to therapy. One study used ^{89}Zr-bevacizumab to investigate the effects of NVP-AUY922, an inhibitor of heat shock protein 90 (HSP90) [129]. HSP90 is a molecular chaperone and is essential for the activity of key proteins in the transcription of VEGF. Its inhibition in an ovarian xenograft led to decreased VEGF expression together with a similar reduction in uptake of the tracer. Ranibizumab is a monoclonal antibody fragment (Fab) of bevacizumab. It has also been labelled with ^{89}Zr and used to examine tumour response to sunitinib [36]. The study reported regression of tumour growth and vascularity with treatment and pronounced rebound when treatment was stopped. This dynamic was reflected in the uptake of ^{89}Zr-ranibizumab particularly in the centre of the tumour, but not seen when using either [^{18}F]FDG or [^{15}O]H_20 PET.

Surprisingly, while there are no published preclinical data for the use of ^{111}In-bevacizumab in assessing antiangiogenic therapies, 2 clinical studies have already been published. The first examined the effect of sorafenib (a VEGFR TKI) in 8 patients with renal cell carcinoma (RCC) prior to nephrectomy [145]. After treatment there was a significant reduction (60%) of tracer in 7 patients with clear cell RCC (ccRCC). The remaining patient had papillary RCC and there was no change in uptake. ^{111}In-bevacizumab uptake within the tumours was heterogeneous and did not correlate with VEGF concentrations determined by IHC or ELISA. It was hypothesised that this was

due to destruction of the vasculature, preventing tracer delivery to the tumour. The most recent clinical study used ^{111}In-bevacizumab in 9 patients with melanoma and compared uptake pre and post a single dose of bevacizumab [138]. Treatment led to an average decrease of 21% of ^{111}In-bevacizumab uptake, presumably due to competitive inhibition. In contrast to the previous study, uptake of ^{111}In-bevacizumab did correlate with VEGF expression on IHC.

4.1.3 Summary

Predictive biomarkers that accurately assess the effect of antiangiogenic therapies are urgently needed. Several approaches have been taken to this problem with some showing promise. Molecular targeted imaging is a rapidly developing field and has only recently been applied to monitoring response to antiangiogenesis agents. In this chapter the utility of molecular targeted imaging agents is explored in the setting of antiangiogenesis therapy.

4.2 Aims

The central aim of this chapter was to investigate suitability of VEGF and Integrin imaging to evaluate the effects of antiangiogenic therapy. The specific objectives were:

1. To determine whether a response to antiangiogenic therapy is detectable using molecularly targeted radiotracers
2. To correlate changes in VEGF and integrin imaging following antiangiogenic therapy with other markers of angiogenesis

4.3 Materials and Methods

Unless otherwise stated all chemicals were purchased from Sigma-Aldrich.

4.3.1 Cell culture and animal husbandry

FaDu cell lines were used for these experiments due to their relatively stable growth rate *in vivo*. The methods for cell-culture, cell-counting, animal welfare, anaesthesia and tumour inoculations are as described in Chapter 2.

4.3.2 Synthesis of ^{111}In-bnDTPA Bevacizumab

^{111}In-labelled bevacizumab was manufactured as described in Chapter 2. Briefly: 300 µg bevacizumab was buffered exchanged with bicarbonate and combined with a 10 molar excess of BnDTPA dissolved in DMSO. After incubation for 1 h the solution was filtered using a G50 Sephadex column and the eluate from 500 µL to 850 µL was saved. The purified BnDTPA-bevacizumab solution was then buffer exchanged with citrate and added to 10-20 MBq $^{111}InCl_3$ to generate the final radiolabelled product.

4.3.3 ^{99M}Tc-Maraciclatide preparation

Maraciclatide was provided in kit form by GE Healthcare as a sterile freeze-dried powder in a 10 mL glass vial containing 75 µg. The maraciclatide was radiolabelled by the clinical radiopharmacists on the day of use according to the manufacturer's instructions. This involved adding 1250 MBq of sodium [^{99m}Tc] pertechnetate to the vial and incubating for 20 min at 25^{o}C. The radiochemical purity was then determined by ITLC. After ITLC confirmed adequate radiochemical purity, the solution was diluted up to 5 mL with sterile 0.9% saline (Braun) and 1.2 mL was withdrawn for injection.

4.3.4 Rapamycin preparation

Rapamycin (11 mg; LC laboratories) powder was dissolved in x25 DMSO (275 µL), and stored in 52 µL aliquots in a -20°c freezer until further use. On the day of treatment an aliquot was thawed and added to 1.248 mL of 5% TWEEN 80, 5% polyethylene glycol 300 (PEG300) and 0.9% NaCl (Braun) while shaking and checking for any signs of precipitation.

4.3.5 ^{111}In-bnDTPA-Bevacizumab *in vivo* studies

4.3.5.1 Rapamycin dose escalation study

Balb/c nude female mice were inoculated with FaDu tumours. Mice were randomly allocated to four different groups. Three weeks after inoculation mice received intraperitoneal (i.p.) rapamycin (1 mg/kg, 5 mg/kg or 20 mg/kg) daily. The control group of mice received an i.p. vehicle injection. After 5 days of therapy all animals received ^{111}In-bnDTPA-bevacizumab (5 MBq, 3 µg) via tail vein injection. Following a further 5 days of rapamycin or vehicle, mice were euthanised. Tumour size was measured during therapy with callipers using the formula $V = (a \times b^2)/2$ where a and b are the largest and the smallest perpendicular diameters, respectively.

4.3.5.2 Single dose rapamycin and negative control study

Balb/c nude female mice were inoculated with FaDu tumours. Three weeks after inoculation mice were started on either daily, i.p. 20 mg/kg rapamycin therapy or vehicle injection. After 5 days of therapy the mice from each arm received either ^{111}In-bnDTPA-bevacizumab (5 MBq, 3 µg) or ^{111}In-bnDTPA-IgG1κ (5 MBq, 3 µg; radiolabelled isotype-matched control antibody) via tail vein injection. The mice continued with therapy for another 5 days and then were euthanised. Tumour size was measured as described above.

4.3.6 ^{99M}Tc-maraciclatide *in vivo* studies

4.3.6.1 Uptake study

Balb/c nude female mice were inoculated with FaDu tumours. Three weeks after inoculation mice received daily i.p. rapamycin (20 mg/kg) or vehicle for 6 days, or bevacizumab (30 mg/kg) once a day on day 1 and 3. After 6 days the mice from each arm received ^{99m}Tc-maraciclatide (100 µL; 25 MBq, 1.5 µg) via tail vein injection. The mice were euthanised 1 h post-injection.

4.3.6.2 Imaging study

Balb/c nude female mice were inoculated with FaDu tumours. Three weeks after inoculation mice were imaged with DCE-MRI and SPECT-CT and then were immediately started on a daily i.p. rapamycin (20 mg/kg) or vehicle regimen for 6 days. On the day after the last treatment the mice were rescanned with DCE-MRI and SPECT-CT.

4.3.6.2.1 SPECT-CT

For pre-treatment scans, mice were anaesthetised and received ^{99m}Tc-maraciclatide (100 µL; 25 MBq, 1.5 µg) via tail vein injection. After 1 h the mice were placed in a purpose-built cradle with respiratory and temperature monitoring. A CT was performed first followed by a SPECT with a photopeak window for ^{99m}Tc. SPECT was performed using 9x1 mm pinhole apertures; 100,000 counts/projection; 24 projections and a pitch of 1.5.

Mice in the post-treatment group, were injected with ^{99m}Tc-maraciclatide while conscious and anaesthetised immediately before scanning (1 h after uptake). The remainder of the procedure was the same as for the pre-treatment group.

4.3.6.2.2 DCE-MRI

DCE-MRI was performed on anaesthetised mice using a 4.7T MRI system (Varian Inova) with a 25 mm quadrature birdcage radiofrequency coil. Mice were cannulated and placed in the scanner with respiratory and temperature monitoring. The scan was acquired using a 3D gradient echo

(GE) sequence with the following parameters: Resolution=422 µm isotropic, matrix=128x64x64, FOV=54x27x27 mm, Flip angle=5°, 17sec/frame, echo time (TE)=1.11 ms, repetition time (TR)=0.58 ms. Gadodiamide (30 µL of 0.5 mmol/mL; Omniscan, GE Healthcare) was injected after 2 min from start of acquisition and the total acquisition time was 1700 sec (28min).

Each image of the acquisition was saved in a Neuroimaging Informatics Technology Initiative (NIfTI) file format and segmented in ITK-SNAP version 2.2. The images were then processed to determine the parameters of initial area under the gadolinium curve (IAUGC) and pixel enhancement ratio. These were performed on a voxel by voxel basis within the segmented tumour region and the average for the whole tumour was calculated. Voxels were considered enhancing if the signal increased greater than 3 standard deviations above baseline. The baseline value and standard deviation were calculated from the data acquired prior to gadodiamide injection.

DCE-MRI and tumour contouring was performed by Stavros Meleminidis. The DCE-MRI parameters were calculated by Danny Allen.

4.3.7 Tumour analysis

Phycoerythrin (PE) conjugated anti-mouse CD31 antibody (100 µL; Biolegend) was administered via tail vein injection 2 min before mice were euthanised. After they had been euthanised, mice were dissected and organs and tumour were harvested. The organs and tumour of each mouse were then weighed and radioactivity measured using a gamma-counter. All radioactivity measurements were decay corrected to a standard time point. After counting, the tumours were cut in half. One half was frozen in liquid nitrogen and stored at -80^{o}c until further use. The other half was used for visualisation of the vascular network using confocal microscopy (see below).

4.3.7.1 Confocal microscopy and vessel analysis

Immediately after resection tumour specimens were examined using confocal microscopy (Leica Microsystems Ltd). Up to 4 randomly chosen fields were imaged for each tumour specimen. Images were acquired with a x10 objective and a Z-stack at 2 µm intervals. A 543 nm laser was used to excite the PE to generate the images.

For each image (FIGURE 43A) a mask of the tumour region was created and contrast of fainter vessels was improved using histogram equalisation. Vessels were detected by applying a line operator [234, 235], non-maximal suppression [236], and binary thinning to the images. The line operator was applied with an angular resolution of 4^{o} and over a scale range of 5-20 pixels. This resulted in 3 output images: A binary image showing the centreline of the detected vessels (FIGURE 43B); an image showing the vessel orientation at each point along the vessel centreline (FIGURE 43C); an image showing the vessel width at each point along the vessel centreline (FIGURE 43D).

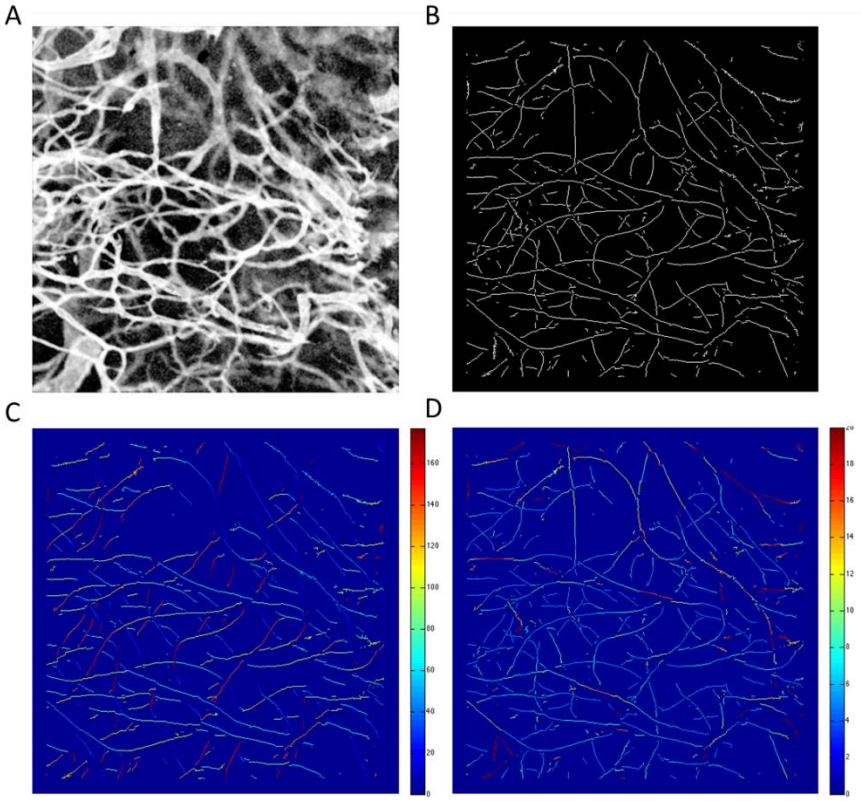


Figure 44 An example of vessel analysis from CD31 immunohistochemistry images. **A**: Original image. **B**: The binary line image. **C**: Orientation image indicating the angulation of vessels (scale represents degrees from 0-180). **D**: Scale Image representing the size of individual vessels (scale represents pixels). Images provided by Danny Allen.

Vessel density was then calculated as the sum of the vessel width image divided by the area of the image mask. Mean vessel size was calculated as the sum of the vessel width image divided by the sum of the binary line image.

Vessel analysis was performed by Danny Allen.

4.3.7.2 VEGF quantification

Tumour VEGF levels were determined by homogenizing frozen tumour samples and measuring protein concentrations and VEGF using the VEGF Quantikine kit (R&D Systems). The specific methods are described in Chapter 2.

4.3.7.3 Integrin quantification

Tumour lysate samples were prepared by homogenising tumour samples in ice-cold radio-immunoprecipitation assay (RIPA) buffer with protease inhibitor (one complete mini tablet (Roche) per 10 mL) (10 mg/mL) followed by incubation for 30 min on ice. The samples were centrifuged for 2x15 min at 14000g at 4^{O}C and the supernatant pipetted off. Protein concentrations of the supernatants were determined as in Chapter 2. The samples were then diluted to 1 mg/mL of protein with RIPA buffer prior to assay. Integrin quantification of the samples was performed using an ELISA kit for integrin β_3 (E91262Mu, USCN Lifescience Inc.) according to the manufacturer's protocol.

Integrin quantification was performed by Sarah Able.

4.3.7.4 Western blots

Homogenised samples from individual tumours were prepared and assayed for protein concentrations as described in Chapter 2. The samples were then diluted to an equal protein concentration in PBS (0.25-0.4 mg/mL). The following standards were also prepared and mixed together with 4 µL of each:

- $VEGF_{121}$ (4644-VS-010, R&D Systems) diluted to 125 ng/mL

- $VEGF_{165}$ (293-VE-010, R&D Systems) diluted to 50 ng/mL
- $VEGF_{189}$ (ab106307, Abcam) diluted to 250 ng/mL

A gel loading buffer was also prepared using, 4% Sodium dodecyl sulphate (SDS), 20% glycerol 0.004% bromophenol blue, and 0.125 M Tris HCl, pH 6.8. Dithiothreitol (DTT) was added immediately before use at 5% to reduce/denature samples. The gel loading buffer was then added to samples and standards (1:1 dilution) and heated to 70^{o}C for 10 min for denaturing. The protein samples were loaded onto a 10 well 4-12% Bis(2-hydroxyethyl) imino-tris (hydroxymethyl) methane-HCl (Bis-Tris) precast gel (Invitrogen). The samples and standards were run on the gel for 55 min at 200V using a NuPage MOPS SDS running buffer (Invitrogen). The gels were then removed and blotted using NuPage transfer buffer (Invitrogen) onto nitrocellulose membrane at 100V for 1 h. The membrane was incubated in blocking buffer (5% BSA in 0.1% Tween-20 in TBS) to block non-specific binding sites. After 1-2 h the blocking buffer was removed and primary antibody added: rabbit anti-VEGF (sc152, Santa Cruz; 1:200 dilution); and rabbit anti-beta actin (ab8227, Abcam; 1:5000 dilution), and diluted in blocking buffer. This was incubated overnight at 4°C with gentle shaking. The next day the membrane was washed 3x5 min with TBS + 0.1% Tween (TBST). Following this, a secondary antibody (goat, anti-rabbit horseradish peroxidase (HRP) conjugate (656120, Invitrogen; 1:3000 dilution), was added, diluted in blocking buffer and incubated for an hour with shaking. This was then washed again for 3x5 min with TBST. The blot was placed against a radiographic film (Super RX, Fujifilm) in the dark (for 30 sec - 1 min) and developed. Following this, the blot was scanned and saved as a tagged image file format (tiff).

Quantitative analysis of the blot was performed using Photoshop CS6 (Adobe). The image was converted to grayscale and inverted. ROIs were drawn around bands and integrated density was calculated. The individual bands were standardised for actin levels and background density of the gel.

Western blots were performed by Sarah Able.

4.3.8 Statistics

Statistical analyses were performed as described in Chapter 2.

4.4 Results

4.4.1 ^{111}In-bnDTPA-bevacizumab studies

4.4.1.1 Rapamycin dose escalation study

To determine the optimal dose of rapamycin for use *in vivo* experiments, the effect of different doses of rapamycin on tumour growth and angiogenesis were investigated. Treatment of FaDu tumours with rapamycin appeared to have a dose dependent effect on growth of the tumours (Figure 44). In the study the highest dose given was 20 mg/kg and this appeared to stabilise the growth of the xenografts. On this basis 20 mg/kg dosing was used for subsequent studies.

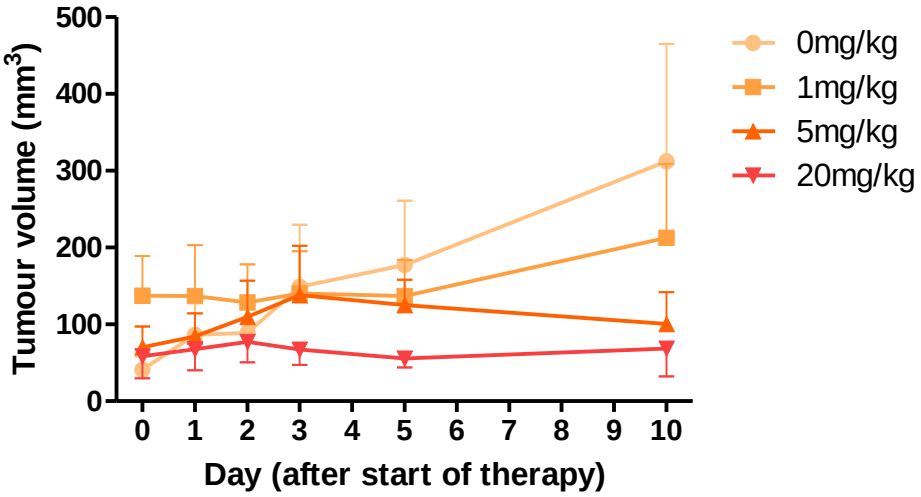


Figure 45: Growth curves of FaDu xenografts in mice treated with daily intraperitoneal rapamycin at different doses. Error bars are SEM. There was no statistically significant difference in size between groups.

The growth inhibition was coupled with an antivascular effect as exhibited by CD31 confocal microscopy of the tumours. The images show reduction in blood vessels (Figure 45A) with increasing doses of rapamycin. Quantitative analysis of the images demonstrated that with the highest dose of rapamycin there was a statistically significant decrease in vessel density (Figure 45B), however no effect was seen on vessel size (Figure 45C).

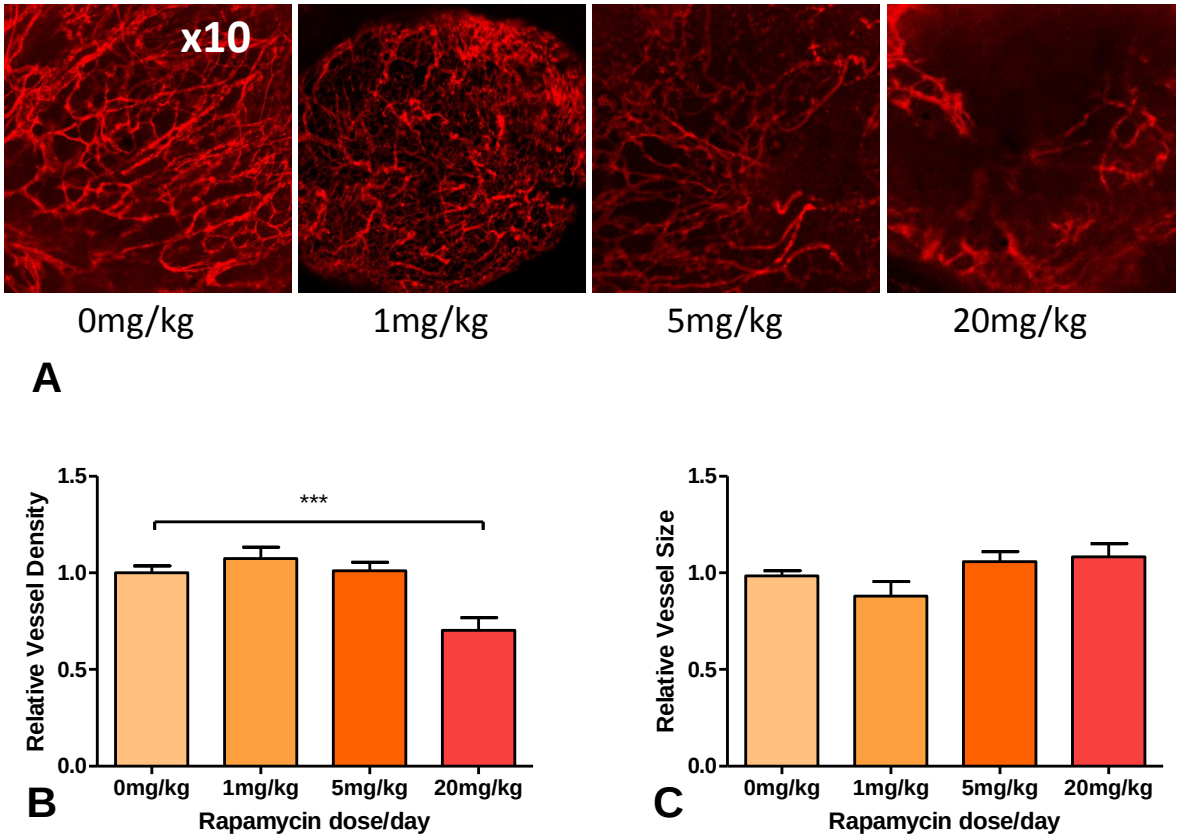


Figure 46: Effects of rapamycin therapy on tumour vasculature. **A**: Selected images of CD31 confocal microscopy of tumours from the different dosage groups. As dose increases there is reduction of vessels. **B**: Changes in relative vessel density with different doses of rapamycin; **C**: Changes of relative mean vessel size with different doses of rapamycin. Bars represent a minimum of 3 tumours with a median of 3 images per tumour. Error bars are SEM.

Increasing doses of rapamycin led to increasing uptake of ^{111}In-bnDTPA-bevacizumab in tumours (FIGURE 46). The only groups that were significantly different from each other were the 20 mg/kg group and the controls, when using an ANOVA (for %ID/g P=0.0012, for T:M ratios P=0.014).

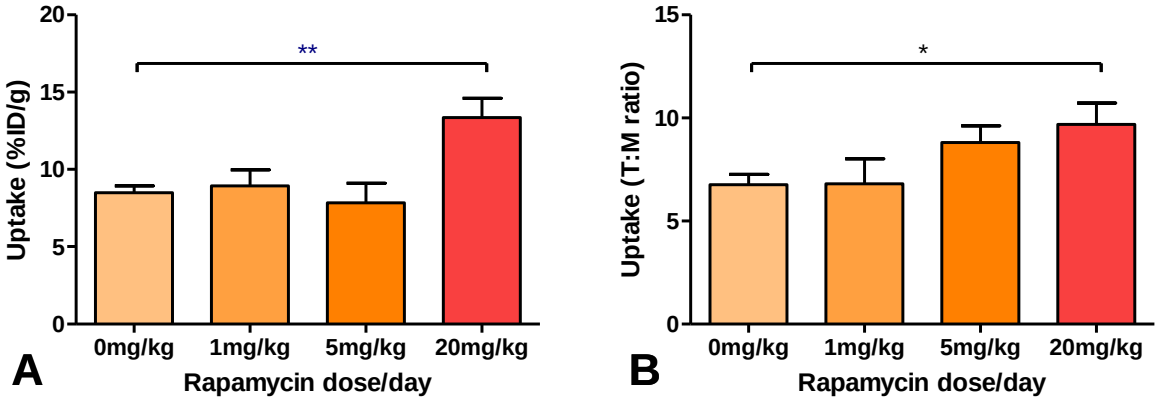


Figure 47: Changes of uptake of ^{111}In-bnDTPA-bevacizumab with increasing doses of rapamycin in FaDu xenografts. Uptake was measured on an absolute scale (%ID/g, **A**) and relative scale (T:M ratio, **B**). Bars represent a minimum of 3 tumours. Error bars are SEM, (*=P<0.05; **=P<0.01).

VEGF within the tumours was quantified by ELISAs, which showed a trend towards increased VEGF production with low dose therapy. However, this did not reach statistical significance (FIGURE 47).

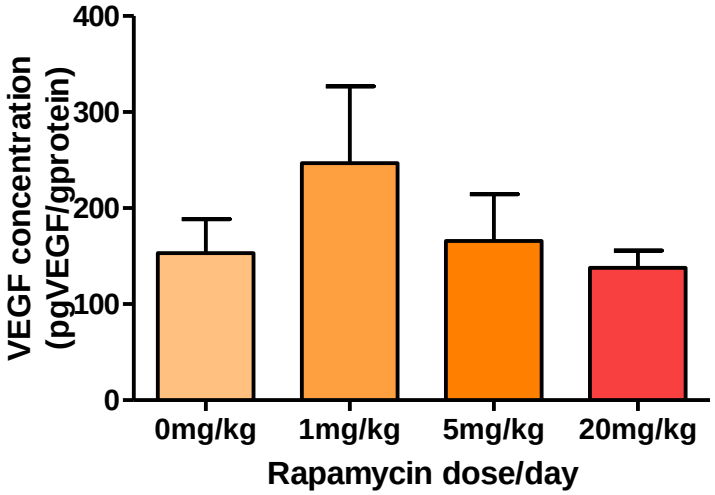


Figure 48: VEGF concentrations within tumours. ELISAs of FaDu xenografts treated with different doses of rapamycin over 10 days. Each bar represents a minimum of 3 tumours. Error bars are SEM. There is no statistically significant difference between groups.

Western blots (FIGURE 48) were used to quantify the relative changes in different isoforms of VEGF (FIGURE 49). These show that $VEGF_{165}$ and $VEGF_{189}$ appear to increase in a similar manner to the total VEGF levels seen in the ELISA. In contrast, $VEGF_{121}$ in the xenografts appears to gradually decrease with increasing dose of rapamycin though numbers are too small to be significant.

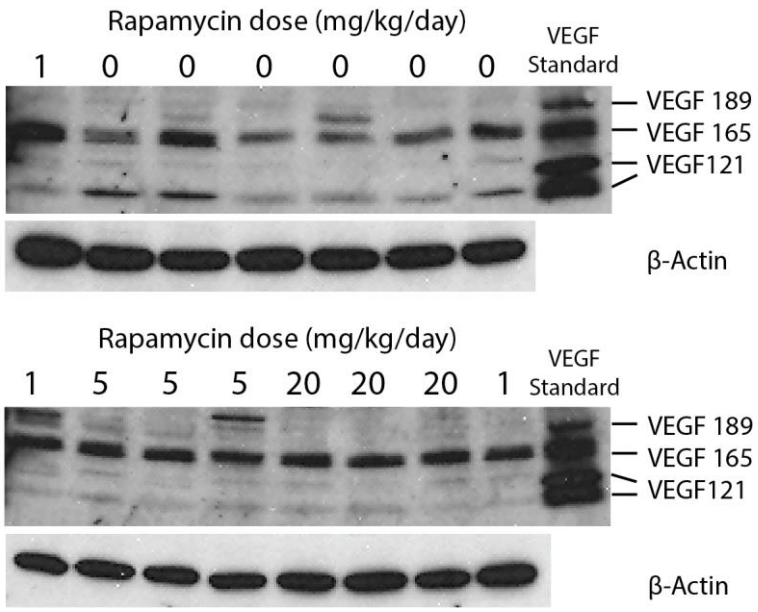


Figure 49: Western blots of VEGF isoforms in FaDu xenografts from mice treated with different doses of rapamycin. Each column is an individual tumour, with the dose of rapamycin specified above it. Images provided by Sarah Able.

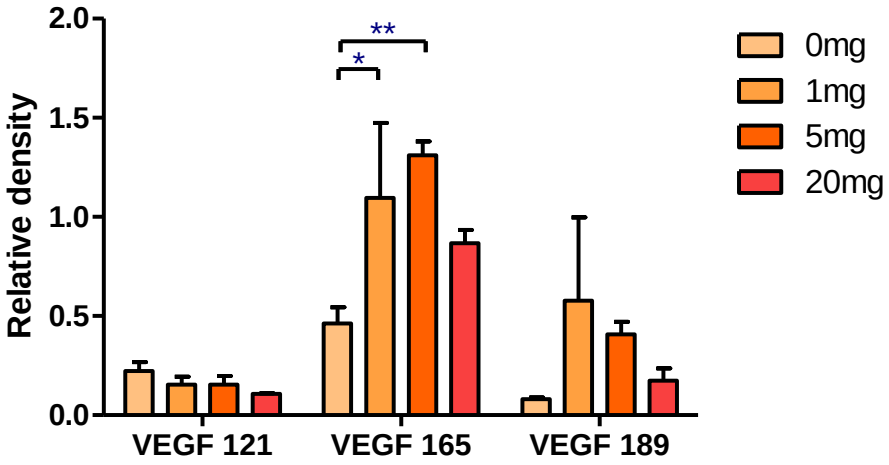


Figure 50: Quantitative analysis of western blots of VEGF isoforms in FaDu xenografts from rapamycin treated mice. Bars represent the dosage groups in Figure 48. Errors bars are SEM. The only statistically significant differences are in the VEGF 165 levels between the control and the 5mg and 20mg treatment groups. (*=P<0.05, **=P<0.01).

4.4.1.2 Single dose rapamycin and negative control study

The increased ^{111}In-bnDTPA-bevacizumab uptake with high dose rapamycin therapy was associated with a decrease in vessel density. One possible explanation for accumulation of the probe is that it is retained non-specifically within the tumours as the vessels are destroyed. To clarify this, tumour uptake of ^{111}In-bnDTPA-bevacizumab was compared with a radiolabelled isotype-matched non-specific antibody tracer (^{111}In-bnDTPA-IgGκ) in mice treated with 20 mg/kg/day rapamycin or vehicle control. In this experiment rapamycin (20 mg/kg/day) had a significant effect on tumour growth (FIGURE 50). There was again a significant decrease in vessel density with therapy, however this time a significant increase in mean vessel size was also demonstrated with the therapy (FIGURE 51).

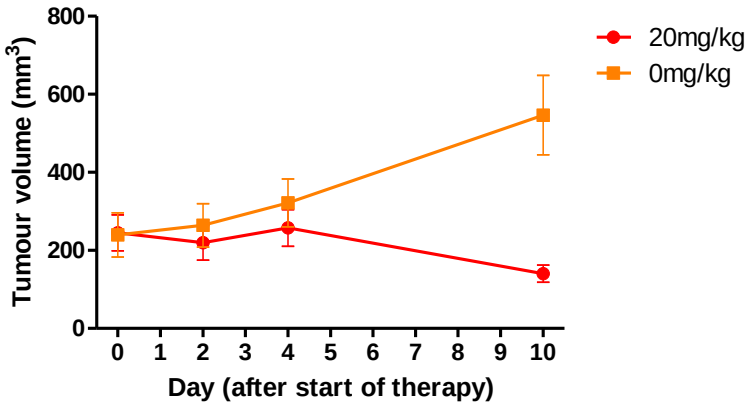


Figure 51: Growth rate of FaDu xenografts in mice treated with rapamycin. Each line represents a minimum of 12 mice. Error bars are SEM. The tumour volumes are statistically different on day 10 (P=0.0004).

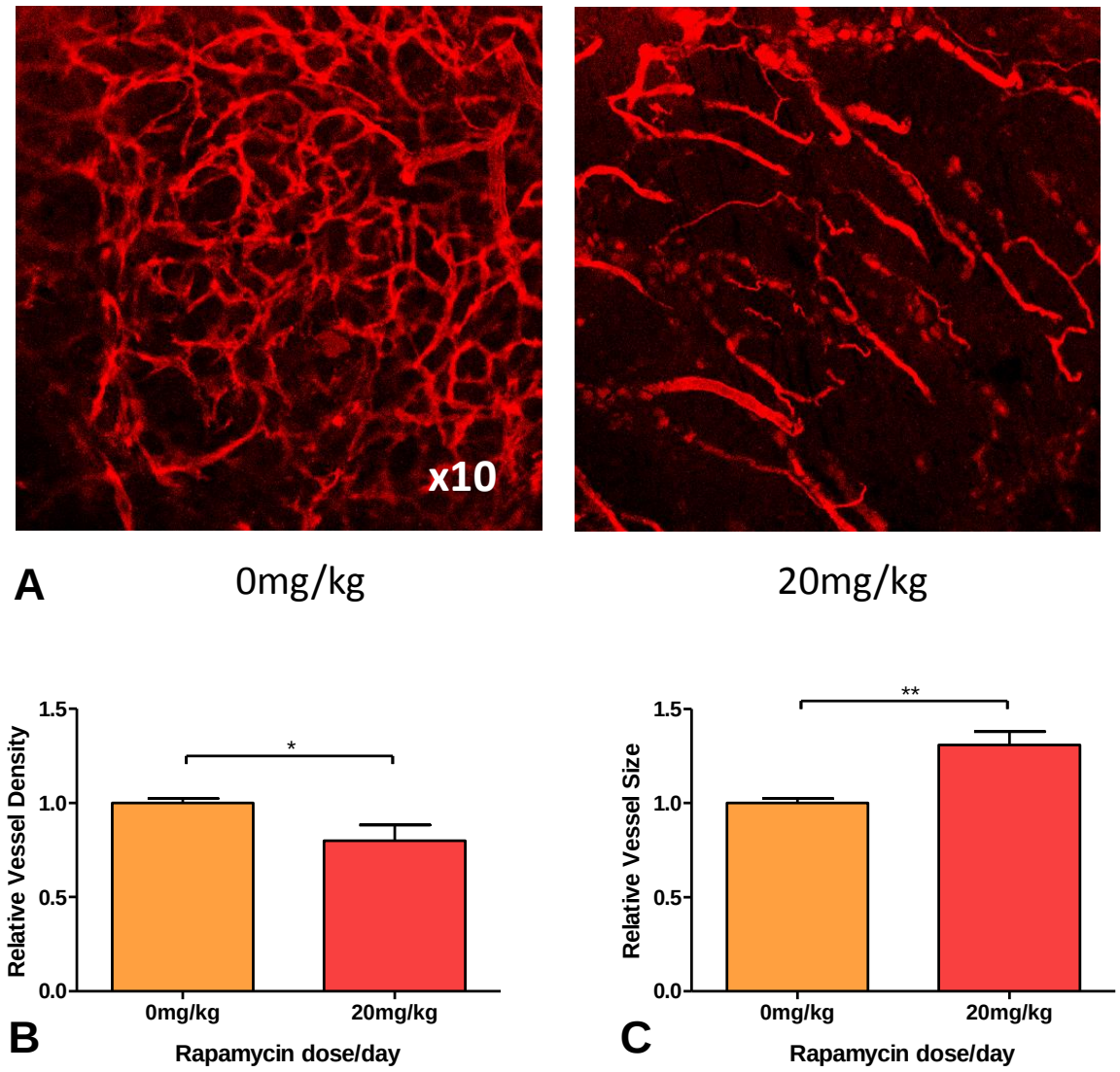


Figure 52: Effect of rapamycin therapy on FaDu xenografts. **A**: Select images of CD31 confocal microscopy of tumours from mice treated with rapamycin 20 mg/kg/day or vehicle control; **B**: Changes in relative vessel density with rapamycin therapy; **C**: Changes of relative mean vessel size of rapamycin. Bars represent 6 tumours with a median of 3 images per tumour. Error bars are SEM. (*=P<0.05, **=P<0.01).

Tumour uptake of ^{111}In-bnDTPA-bevacizumab significantly increased (68% increase in uptake) with rapamycin therapy (FIGURE 52). In contrast the control antibody had very low uptake which did not significantly change (10% increase in uptake) after rapamycin therapy. This indicates that the increase in ^{111}In-bnDTPA-bevacizumab uptake is specific and not related to the associated vascular changes.

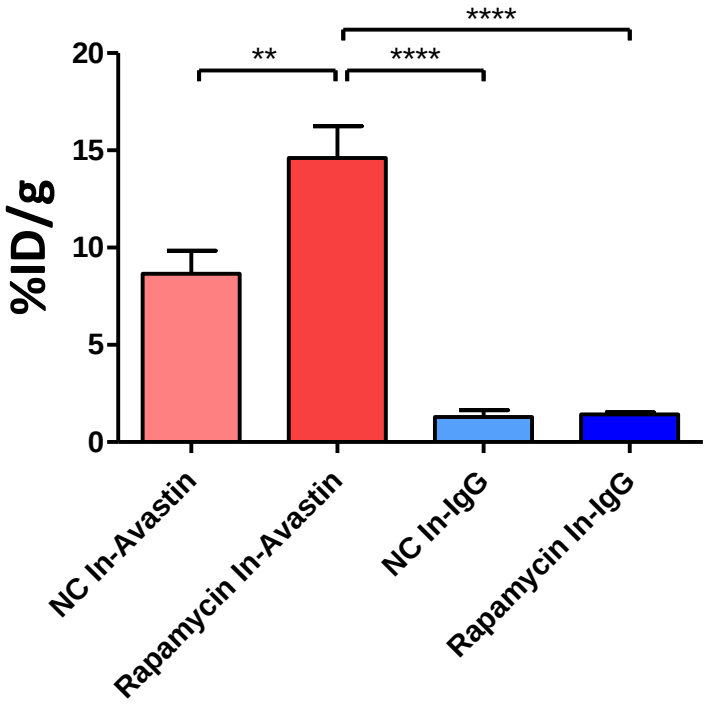


Figure 53: Uptake changes of ^{111}In-bnDTPA-bevacizumab (In-Avastin) and ^{111}In-bnDTPA-IgGκ (In-IgG) in FaDu xenografts treated with rapamycin (20 mg/kg). NC=negative control, treated with vehicle injections. Each bar represents a minimum of 5 mice. Error bars are SEM; (**=*P*<0.01, ****=*P*<0.0001).

Comparison with overall VEGF levels (measured by ELISA) within the tumours suggest that the increased uptake of ^{111}In-bnDTPA-bevacizumab was associated with an increase in VEGF (FIGURE 53), however the changes were not statistically significant. Relative differences in VEGF isoforms may account for this as described later.

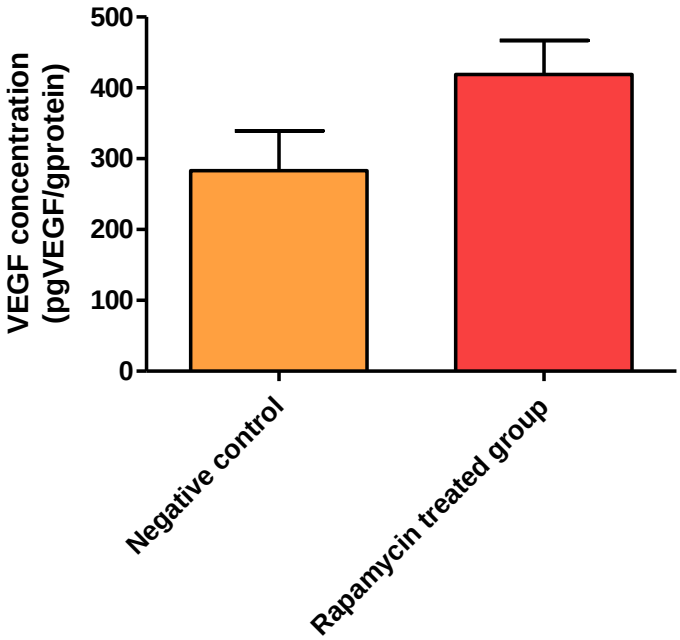


Figure 54: Changes in VEGF levels in FaDu xenografts with rapamycin (20mg/kg) therapy. Each bar represents a minimum of 11 mice per group. Error bars are SEM.

Similarly, when assessing the different isoforms of VEGF with western blots, $VEGF_{165}$ appeared to with rapamycin therapy, whereas $VEGF_{121}$ and $VEGF_{189}$ did not appear to change in concentration (FIGURE 54).

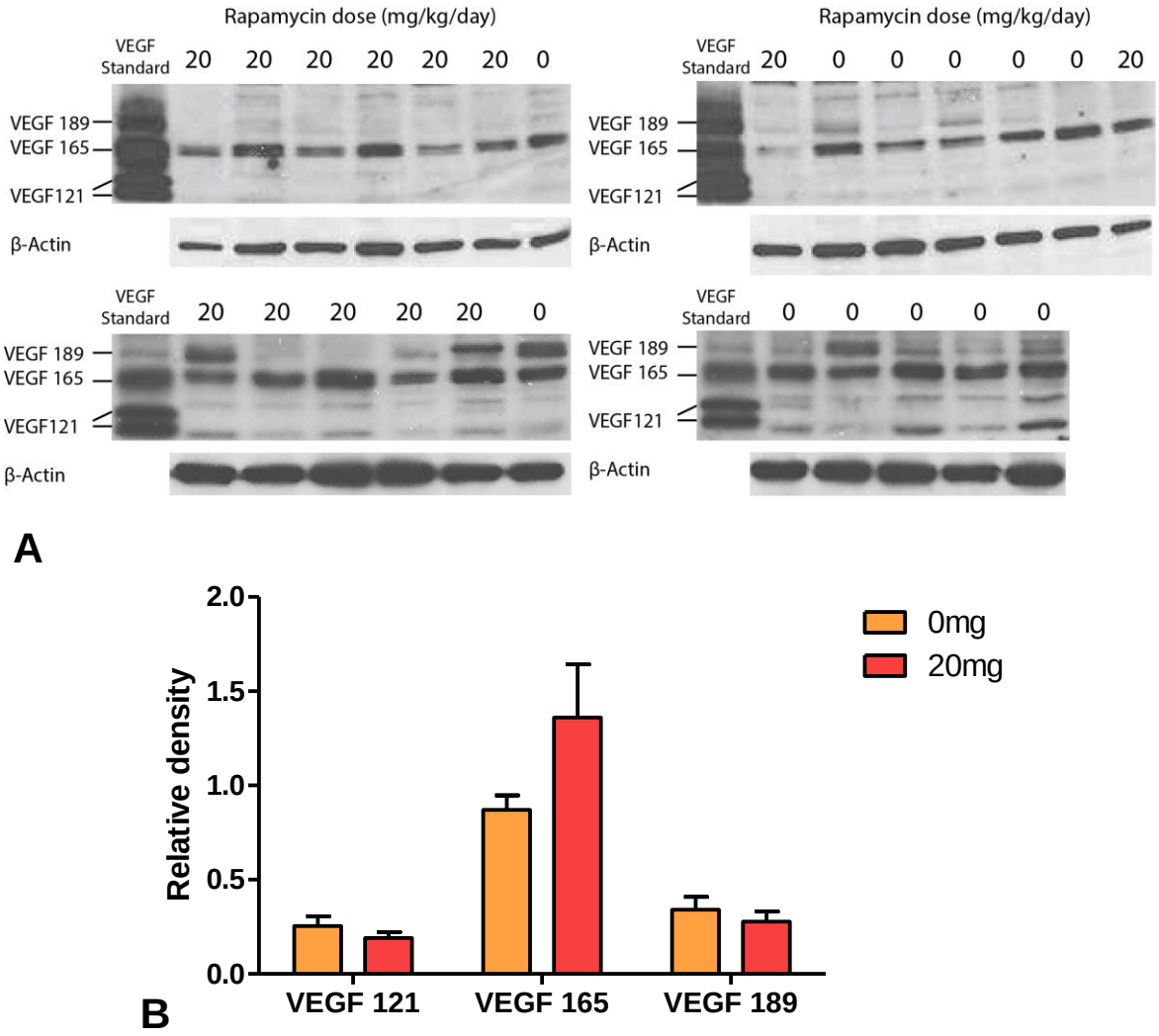


Figure 55: Changes in VEGF isoforms in FaDu tumours from mice treated with rapamycin. **A**: Western blots of each tumour. **B**: Quantitative analysis of the western blots. Bars represent the mean of each treatment group. Error bars are SEM. There is no statistical difference between treated and untreated VEGF isoform levels. Western blot images provided by Sarah Able.

4.4.1.3 Both experiments combined

The individual experiments did not demonstrate a significant change in VEGF isoforms, however, when data from both experiments were combined for the mice treated with 20 mg/kg/day of rapamycin and compared with the vehicle treated group, there was a statistically significant

increase in $VEGF_{165}$ levels with therapy (FIGURE 55). This may result from activation of alternative pathways to induce VEGF expression, as will be discussed later.

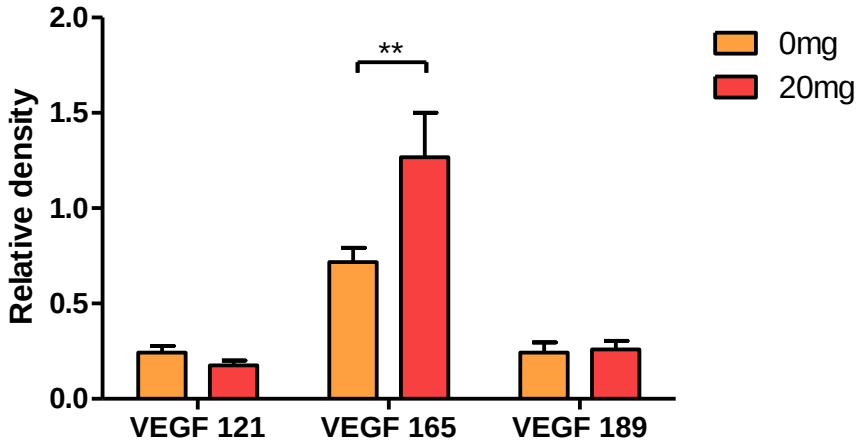


Figure 56: Quantitative analysis of western blots for VEGF isoforms. A significant change was only demonstrated in $VEGF_{165}$ levels. Each bar represents 16 tumours. Error bars are SEM, (**=*P*<0.01).

Furthermore, blood vessel changes when compared using the combined results from both experiments yielded greater statistical significance (FIGURE 56).

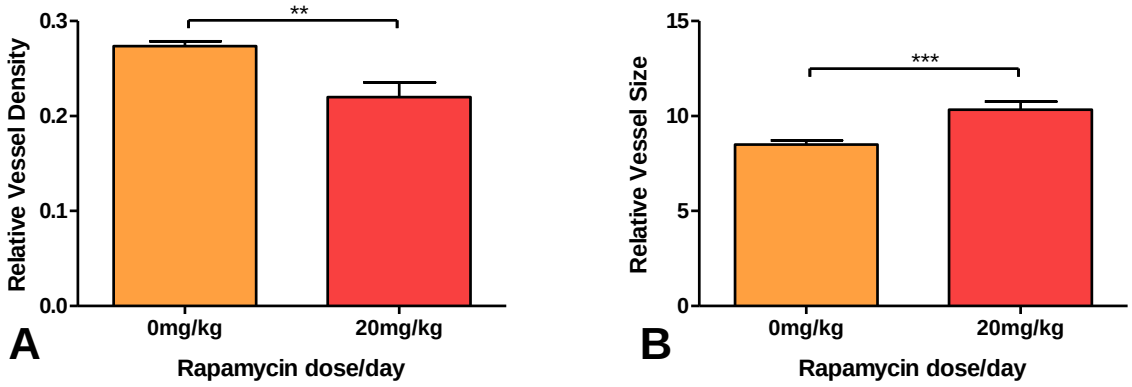


Figure 57: Vessel changes of FaDu xenografts with rapamycin therapy. **A**: Changes in relative vessel density with different doses of rapamycin; **B**: Changes of relative mean vessel size with different doses of rapamycin. Bars represent a minimum of 12 tumours with a median of 3 images per tumour. Error bars are SEM, (**=*P*<0.01; ***=*P*<0.001).

4.4.2 ^{99M}Tc-maraciclatide studies

4.4.2.1 Tracer characteristics

Mice were injected with ^{99m}Tc-maraciclatide and distribution of tracer after one hour was determined by gamma counting of ex vivo specimens. Greatest uptake was seen in the kidneys (≈ 3%ID/g) followed by the tumour (≈2%ID/g), with remaining organs at around 1%ID/g or less (Figure 57A). The mean tumour to muscle ratio was 2.3. Similar to ^{111}In-bnDTPA-bevacizumab, no correlation was seen between the size of tumour and the degree of uptake (Pearson r=0.09, P=0.69) (Figure 57B). Also, like ^{111}In-bnDTPA-bevacizumab there was a correlation between calculation of uptake by %ID/g and by T:M ratios (Pearson r=0.58, P=0.003)

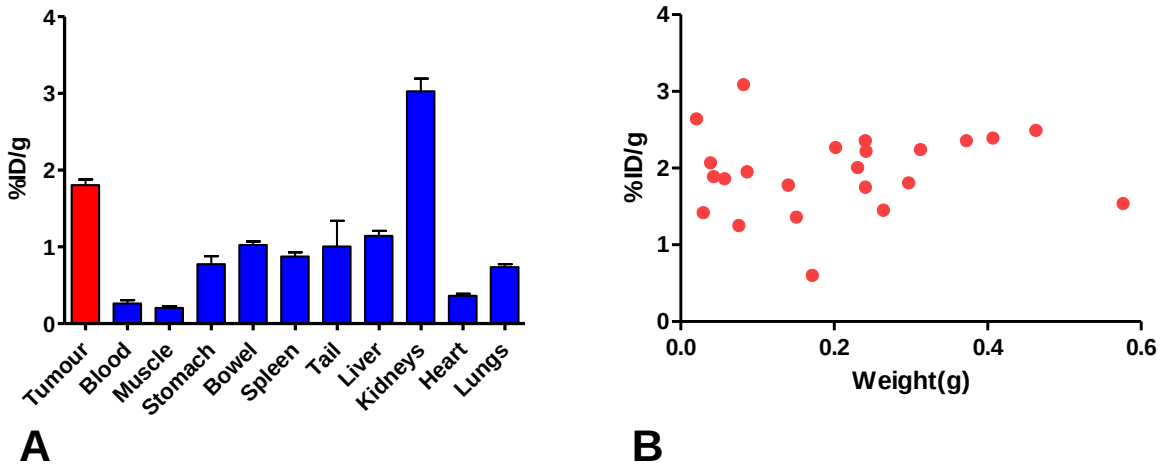


Figure 58: Characteristics of ^{99m}Tc-maraciclatide uptake in FaDu xenografts 1 hour after injection. **A:** Distribution of tracer within organs and tumour; **B**: comparison of uptake (%ID/g) and mass of tumour.

4.4.2.2 Pre- and post-therapy

4.4.2.2.1 Uptake study

Mice bearing FaDu xenografts were treated with either rapamycin (20 mg/kg per day) or bevacizumab (30 mg/kg twice weekly) for 6 days. Treatment with both drugs appeared to lead to vascular reduction which was most prominent in the rapamycin-treated group (Figure 58). There was no significant effect on the size of the tumours following either treatment. Uptake of ^{99m}Tc-

maraciclatide (measured by gamma counting of *ex vivo* tumours) significantly decreased in the rapamycin treated group with a relative mean decrease of 35% (P<0.01) (FIGURE 59). In contrast, no significant change in uptake was demonstrated in the bevacizumab-treated group.

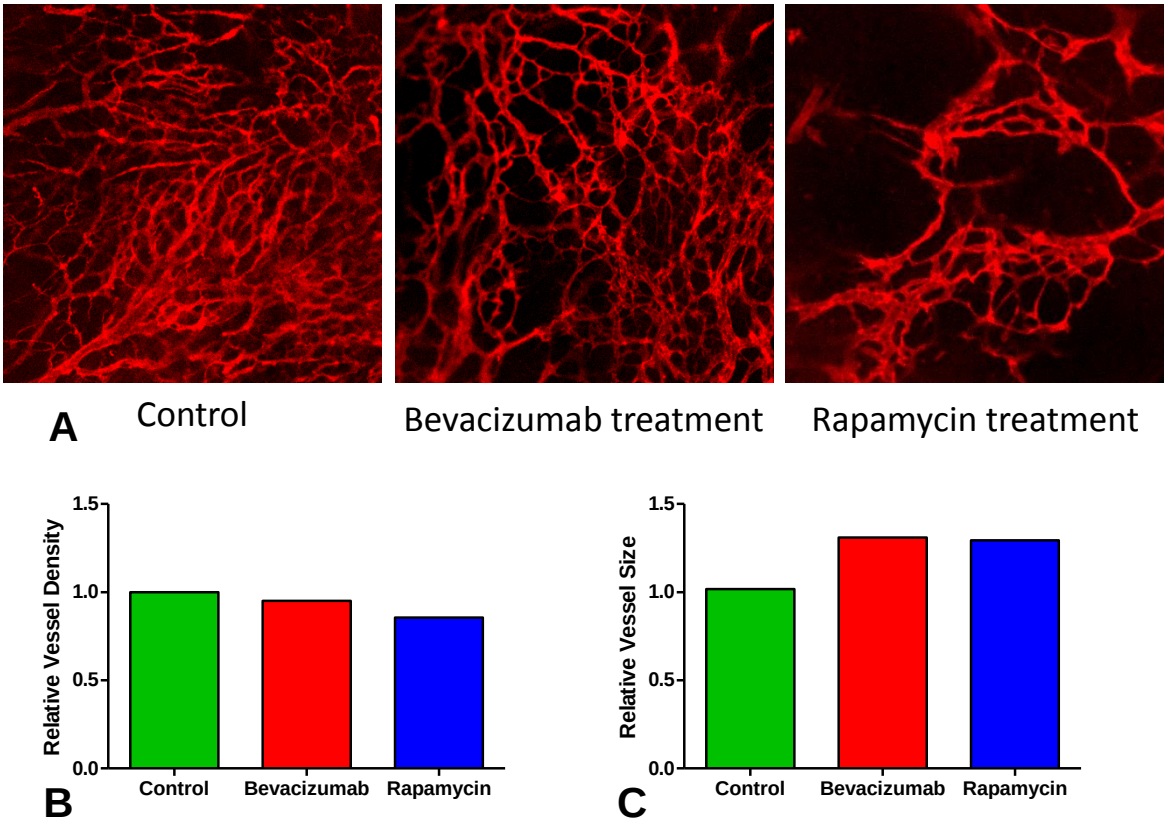


Figure 59: Vascular changes with antiangiogenic therapy. **A:** Select images of CD31 confocal microscopy of tumours with different antiangiogenic therapies. **B:** Changes in vessel density with different therapy; **C**: Changes of mean vessel size with different therapy. Bars represent 2 tumours with 4 images per tumour.

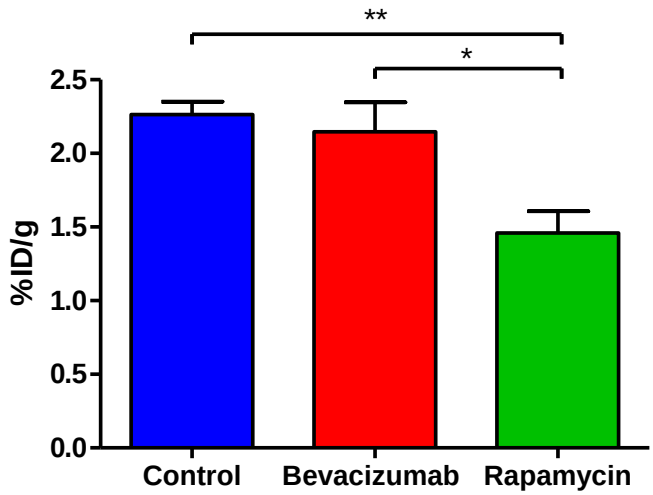


Figure 60: Changes in uptake of ^{99m}Tc-maraciclatide in FaDu xenografts with either rapamycin or bevacizumab therapy after 6 days. Bars represent a minimum of 7 tumours. Error bars are SEM; (*=P<0.05, **=P<0.01)

The change in uptake of ^{99m}Tc-maraciclatide with therapy was reflected in β_3 integrin levels (as determined by ELISA), which appeared to show a decrease in the rapamycin treated group and a slight increase in the bevacizumab treated group, though none of these changes were statistically significant.

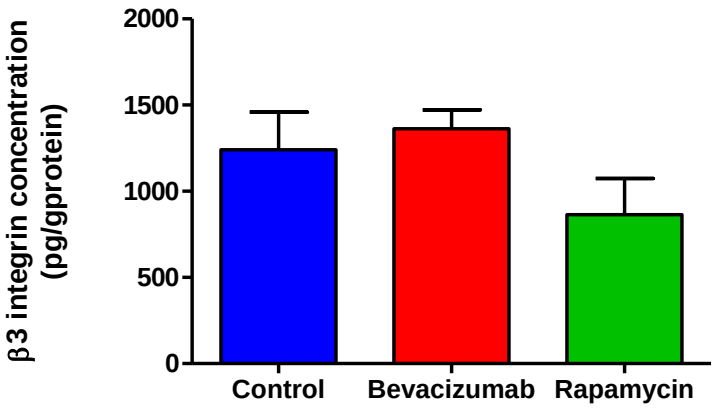


Figure 61: Changes in β3 integrin levels with antiangiogenic treatment. There appears to be a decrease in the rapamycin treated group, though this is not statistically significant. Bars represent a minimum of 7 tumours. Error bars are SEM.

Comparison between uptake of ^{99m}Tc-maraciclatide and β3 integrin levels yielded an almost statistically significant correlation (r=0.24, P=0.056).

4.4.2.2.2 Imaging study

The uptake study displayed a decrease in ^{99m}Tc-maraciclatide uptake between the rapamycin treated group and the untreated group by gamma counting *ex vivo* tumours. To investigate whether such changes were reproducible in an individual and detectable by imaging, SPECT-CT was used to image mice pre and post therapy. This was combined with DCE-MRI as a comparative method for assessing angiogenesis. SPECT imaging with ^{99m}Tc-maraciclatide failed to demonstrate any significant uptake within the tumour (FIGURE 61), despite changes to the protocol which enabled uptake time in the mice whilst not anaesthetised. This was anticipated to decrease activity within the bladder by enabling the mice to micturate whilst awake.

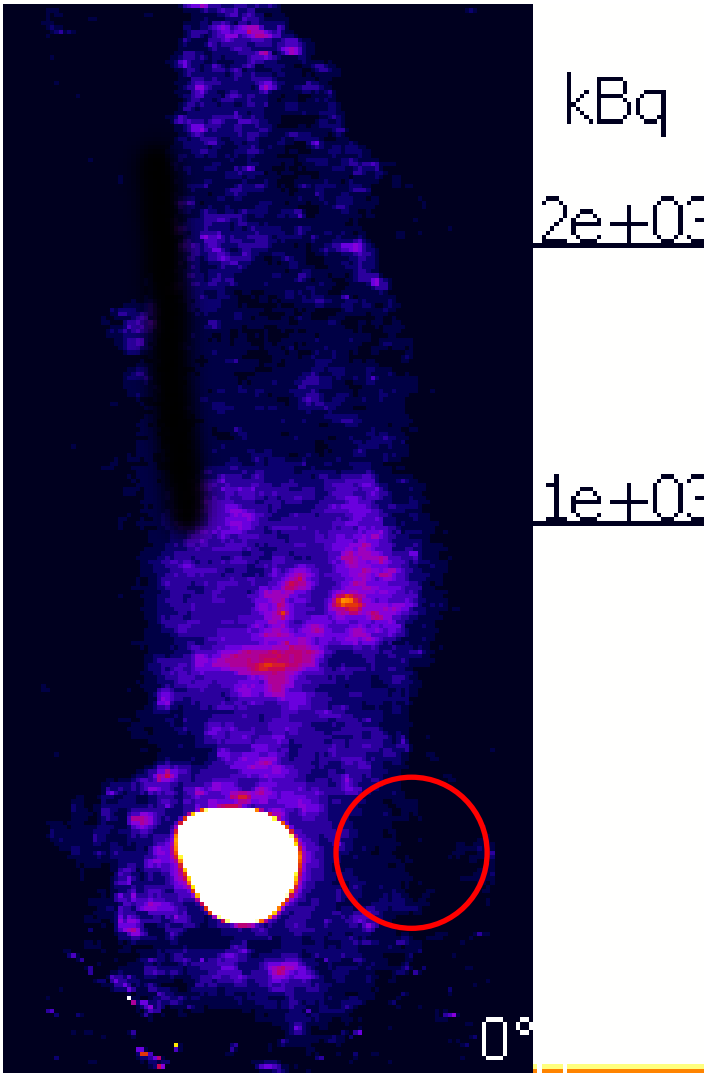


Figure 62: ^{99m}Tc-maraciclatide in a FaDu xenograft bearing mouse. SPECT MIP 1 h after injection. Activity is predominantly seen within the bladder. The tumour was not visualised (site marked with red circle).

The DCE-MRI was performed before and after therapy on 5 (3 treated and 2 untreated) mice (FIGURE 62). The dynamic enhancement of the tumours was analysed by determining the change in the initial area under the gadolinium curve (IAUGC) and fraction of enhancing voxels at different times from the start of injection of gadolinium. The results suggested that there is increased IAUGC and voxel enhancement in the control group, whereas the treated group appears to show decreased IAUGC and decreased voxel enhancement. Due to the small number of mice included, the results could not be analysed for statistical significance.

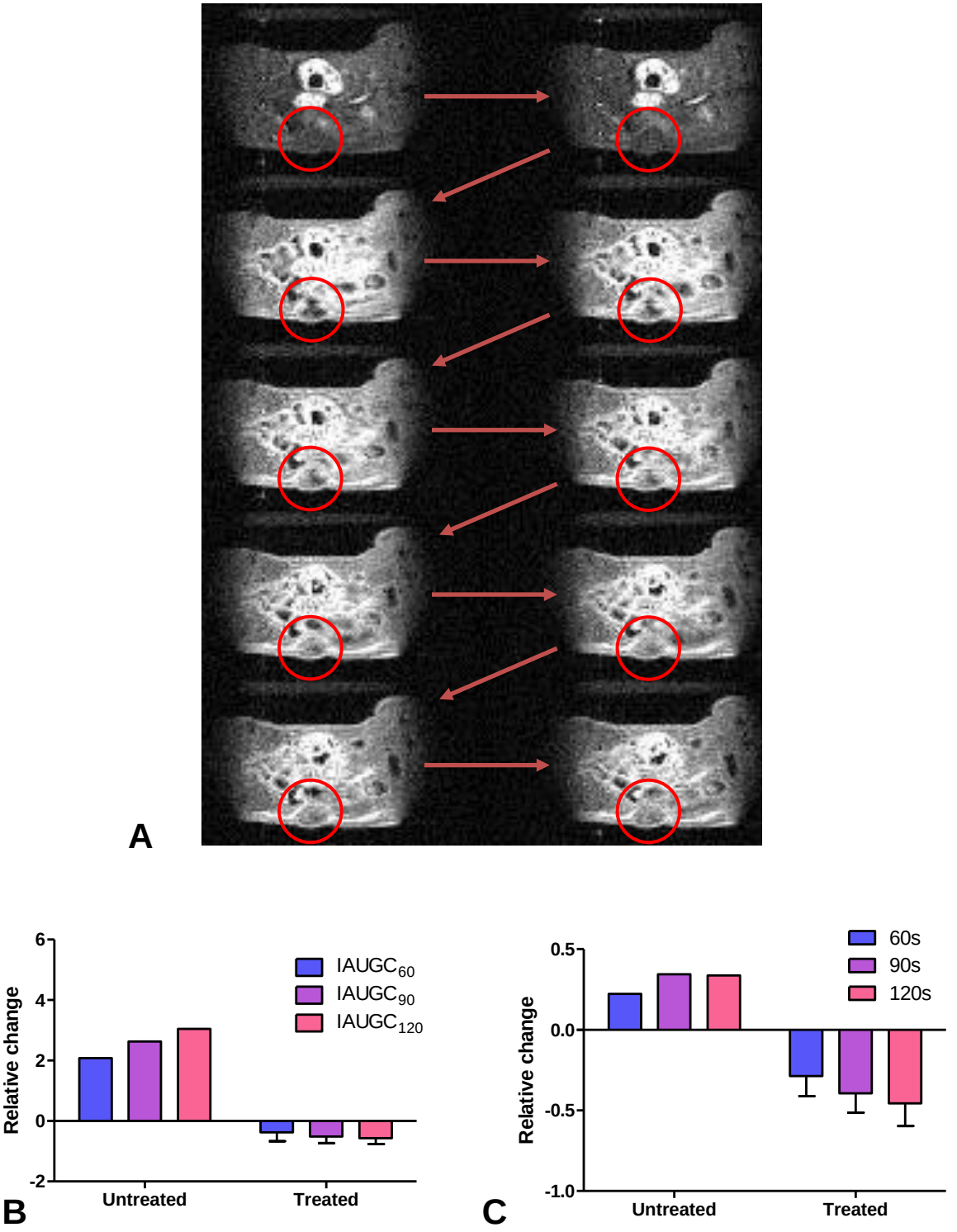


Figure 63: DCE-MRI of FaDu xenografts. **A** is an example of one tumour (red circles) imaged sequentially post-contrast injection. Images read from left to right and are 10 frames (170s) apart. The tumour enhances initially from the periphery and then fills in towards the centre. From the images, changes in IAUGC (**B**) and enhancing fraction (**C**) between pre and post therapy scans were determined. Both graphs demonstrate the relative change in parameters after the initial 60, 90 or 120 seconds post-contrast injection, in individual tumours treated with either 20 mg/kg/day rapamycin (treated) or vehicle control (untreated). Bars represent 2 mice in the untreated group and 3 mice in the treated group. Error bars are SEM. DCE-MRI images provided by Stavros Melemenidis.

4.5 Discussion

Over the last decade great progress has been made in the development of a number of antiangiogenic therapies. Despite several positive results there is concern about the efficacy of the drugs which may be useful only in a small and, at present, unidentifiable subset of patients. This coupled with high drug costs and adverse side effects has highlighted the need for accurate biomarkers for assessing angiogenesis and its response to therapy. This study investigated the response of two different angiogenesis imaging agents to antiangiogenic therapy (rapamycin and bevacizumab).

4.5.1.1 ^{111}In-bnDTPA-bevacizumab

Rapamycin was used in these experiments as it has antiangiogenic activity leading to decrease in VEGF and MVD in several preclinical animal models [237, 238]. It is a macrolide and binds to FK506 binding-protein 12 (FKBP12) to create a complex that inhibits the mammalian target of rapamycin (mTOR). MTOR is a component of the phosphoinositide 3-kinase (PI3K)/protein kinase B (AKT)/mTOR pathway, and is a major regulator of cell proliferation, metabolism, survival and angiogenesis [239] (Figure 63).

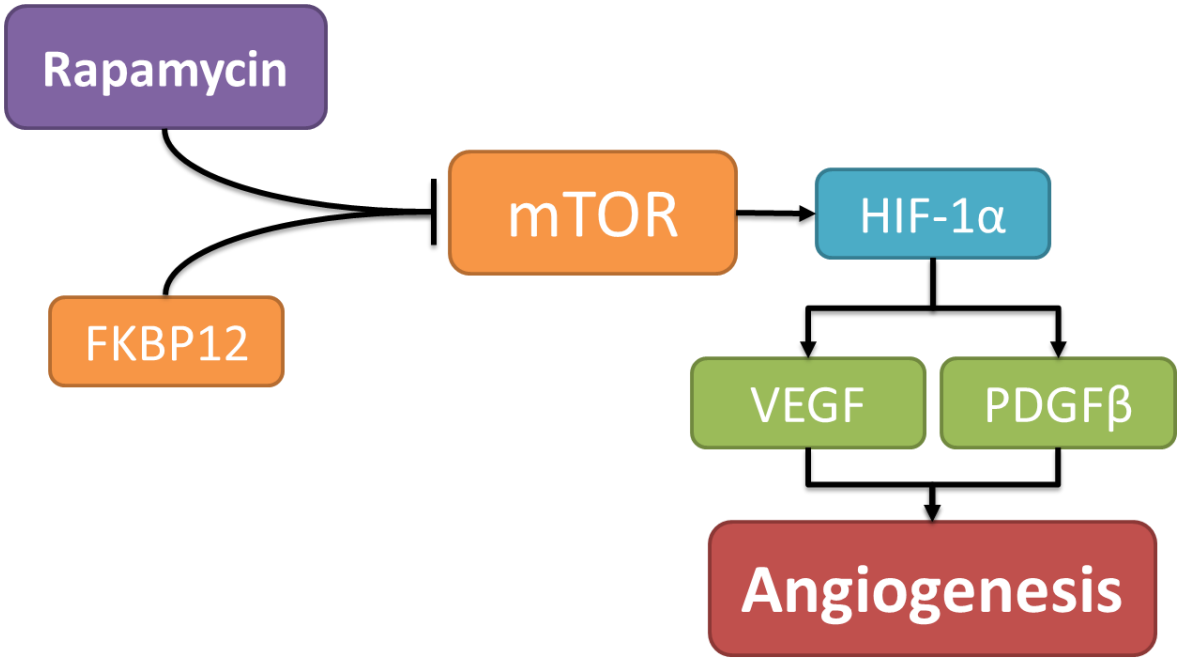


Figure 64: Rapamycin and inhibition of angiogenesis. Rapamycin binds to FKBP12, and the complex binds to mTOR to inhibit its kinase activity. This suppresses HIF-1α levels in cells leading to reduced VEGF and PDGFβ and consequently angiogenesis.

The initial dose-optimisation study using rapamycin demonstrated a dose dependent tumour growth inhibitory effect. Furthermore, vessel density in the xenografts decreased in the highest dose treatment group when analysed with CD31 confocal microscopy. This was most striking when visually comparing the images. Quantitative analysis of the vessel changes did not demonstrate as great a difference between groups, and may indicate that further refinement of the analytical technique is required.

The highest dose group also yielded significant changes in uptake of ^{111}In-bnDTPA-bevacizumab. Therefore further studies were conducted with the 20 mg/kg/day dose in this tumour model. VEGF changes in this study were measured by ELISAs and western blots, which demonstrated that $VEGF_{165}$ is the dominant isoform within the tumours and that its level increases with rapamycin therapy.

A subsequent experiment investigated whether the changes in uptake were a phenomenon specific to ^{111}In-bnDTPA-bevacizumab imaging or due to purely structural changes within the vasculature. To address this, uptake of ^{111}In-bnDTPA-bevacizumab was compared to uptake of an isotype-matched, non-specific, control antibody (^{111}In-bnDTPA-IgGκ). Treatment with rapamycin led to a significant increase of 68% of uptake of ^{111}In-bnDTPA-bevacizumab, in contrast to the control antibody where there was no significant increase in uptake. These results confirm that the changes in uptake of ^{111}In-bnDTPA-bevacizumab with rapamycin therapy are specific.

The experiment also used larger numbers than the dose-optimisation study to further assess the significance of the architectural and molecular angiogenic changes seen in the optimisation study. The results demonstrated that treatment with 20 mg/kg/day of rapamycin led to overall decreased growth within the tumours, combined with a significant decrease in vessel density, whilst mean vessel size in the tumours significantly increased. Such changes within the vessels are in keeping with “normalisation” of tumour vessels [240], where smaller vessels are pruned leading to reduced vascular density with an overall increased mean vessel diameter.

Quantification of VEGF levels with ELISAs demonstrated a trend towards VEGF levels increasing with rapamycin therapy, which is in keeping with the increase in uptake of ^{111}In-bnDTPA-bevacizumab seen. The lack of statistical significance in the increase of overall VEGF levels may have been attributable to relative differences in VEGF isoforms. Analysis of the western blots, suggested that the changes in VEGF levels were predominantly due to an increase in $VEGF_{165}$. $VEGF_{121}$ and $VEGF_{189}$ levels did not appear to change with rapamycin therapy. These results conflict with the mechanistic hypothesis that mTOR inhibition decreases VEGF levels, and also with evidence from other groups who have shown decreased VEGF levels in tumours treated with rapamycin [238, 241, 242]. A potential explanation for this apparent inconsistency is that the rapamycin dose used is one of the highest doses described for animal experiments [242]. It could have led to hypoxia, which may have countered the effects of rapamycin on HIF-1α, leading to increasing levels of VEGF.

4.5.1.2 ^{99m}Tc-maraciclatide

^{99m}Tc-maraciclatide has a different biodistribution to ^{111}In-bnDTPA-bevacizumab with overall much lower uptake at 1 hour within organs and tumour as a function of the injected dose, though tumour to background as measured by tumour to muscle ratio is comparable. The highest uptake is seen within the kidneys, with the next highest within the tumour. Blood levels are very low in comparison to ^{111}In-bnDTPA-bevacizumab where levels are around 10%ID/g even after 5 days. These differences are partly a result of the size of the molecules. ^{111}In-bnDTPA-bevacizumab is 149 kDa whereas ^{99m}Tc-maraciclatide is 1.7kDa, which results in much faster pharmacokinetics and shorter biological half-life.

For ^{99m}Tc-maraciclatide the effects of both rapamycin and bevacizumab on uptake were investigated. Vessel analysis was only performed for 2 tumours out of each group due to time constraints and limited personnel available for conducting the experiment. Therefore changes in relative vessel density and mean vessel size could not be determined with confidence. Both

therapies appeared to have an effect on vessel structure with increased mean vessel size, whereas, there was no evidence of effect on vessel density. Changes in the vasculature with rapamycin therapy were also demonstrated in the second experiment with DCE-MRI. In the few mice imaged, IAUGC and the fraction of enhancing voxels appeared to decrease when mice were treated with rapamycin. These results suggest that rapamycin led to decreased vascular permeability and perfusion of the tumours.

Of the two antiangiogenic therapies, only rapamycin had a significant effect on uptake of ^{99m}Tc-maraciclatide in the tumours. This was reflected by ELISAs of the tumour samples which showed a similar but non-significant trend in changes of β_3 integrin levels. The lack of statistical significance may result from lack of a strong correlation between ^{99m}Tc-maraciclatide uptake and β_3 integrin levels. This may be due to ^{99m}Tc-maraciclatide binding specifically to not only β_3 but also β_5 subunit integrins [1], and β_3 integrin levels also representing $\alpha_{IIB}\beta_3$ levels, to which ^{99m}Tc-maraciclatide does not bind.

As ^{99m}Tc-maraciclatide can be imaged on the same day as administration, a further experiment was attempted to determine uptake changes with therapy in individual mice. It was not possible to perform this type of experiment with ^{111}In-bnDTPA-bevacizumab as imaging is optimal at 5 days after administration. This means that assessing the effects of therapies against controls with ^{111}In-bnDTPA-bevacizumab would lead to xenografts growing too big before re-imaging could be performed. Unfortunately, it was not possible to visualise ^{99m}Tc-maraciclatide uptake in xenografts with SPECT-CT. One possible explanation for this is the high amount of activity that is retained in the bladder, which leads to large amounts of scattered radiation and reduces the ability to demonstrate surrounding structures. The imaging protocol was altered to attempt to decrease bladder activity by anaesthetising the mice immediately before they were due to be imaged. Despite such measures, tumour uptake of ^{99m}Tc-maraciclatide was not demonstrated. Another group using ^{99m}Tc-maraciclatide (ACTREC, Navi Mumbai, India) has also reported similar

difficulties in visualising flank xenografts due to bladder activity (personal correspondence). By moving the site of implantation to the neck, where there is very little background activity, they managed to remedy this problem and visualise the xenografts. Future work with this tracer will involve changing the site of implantation of xenografts to facilitate imaging with SPECT-CT.

Both rapamycin and bevacizumab have an effect on vascularity but only rapamycin leads to a decrease in integrin expression. This suggests that mTOR activation is an upstream event to integrin expression, and its inhibition leads to a decrease in integrin expression. The lack of effect of VEGF inhibition may relate to a differential effect on integrin expression. There is evidence that VEGF is mediated predominantly via $\alpha_v\beta_5$ expression in comparison to basic fibroblast growth factor (bFGF) which requires $\alpha_v\beta_3$ function [149]. Therefore inhibition of VEGF via bevacizumab may only affect $\alpha_v\beta_5$ expression, hence not necessarily affecting the levels of $\alpha_v\beta_3$ or ^{99m}Tc-maraciclatide uptake. The interplay between VEGF and integrins is further complicated by the fact that $\alpha_v\beta_3$ stimulates VEGF expression [151] and enhances VEGF signalling via VEGFR2 [243].

4.5.2 Conclusion

Uptake of both ^{111}In-bnDTPA-bevacizumab and ^{99m}Tc-maraciclatide, changed in a xenograft model following treatment with antiangiogenic therapies. Such changes appear to be related to altered expression of VEGF and integrins respectively and are also associated with changes in vessel structure and function as demonstrated by the CD31 and DCE-MRI analysis. The results also highlight the complex nature of the effects of antiangiogenic therapies and indicate that further work is necessary before the significance of changes in tracer uptake are fully understood.

5 Discussion

5.1 Introduction

It is well established that the tumour microenvironment is a key determinant of the natural history of cancers. The growth of new blood vessels, angiogenesis, is one of the fundamental processes required for tumour growth and metastases [244, 245]. Currently, a number of agents targeting the angiogenic pathway such as bevacizumab, sunitinib and sorafenib have been studied in clinical trials and demonstrated to be of some benefit [246-251]. Despite this, their use is limited because of both cost and our current inability to predict which patients will either derive benefit or develop resistance [252-256]. At present, no reliable biomarkers that correlate with the efficacy of anti-angiogenic therapy have been identified. These biomarkers are urgently needed to identify responders and to predict the efficacy of regimens that include anti-angiogenic agents [257, 258].

Imaging with targeted radionuclides holds promise as a non-invasive method for assessment of tumour angiogenesis and potential disease response. In addition, it may aid the selection of anti-angiogenic therapy with drugs targeting a specific pathway expressed in the tumour. This is especially relevant for metastases (the main targets for therapy), where there is incomplete understanding of the important pathways and limited histological samples available for analysis. Some of the key pathways in angiogenesis involve members of the VEGF family and integrins. The ability to accurately assess the status of these mediators would help elucidate the complex mechanisms of angiogenesis and guide therapy.

This thesis focusses on 2 radio-tracers: ^{111}In-bnDTPA-bevacizumab and ^{99m}Tc-maraciclatide for imaging VEGF and integrins, respectively. The aims of the research presented in this thesis were to validate the tracers and to determine whether they can detect the effect of antiangiogenic therapies in tumours.

5.2 Validation of Imaging Agents

5.2.1 ^{111}In-BnDTPA-Bevacizumab

5.2.1.1 Rationale

VEGF is one the key effectors in the VEGF pathway and angiogenesis. Despite being extensively investigated there are still many facets of its biology that are not fully understood. These include the range of expression profiles in metastases, organ dependence and response to antiangiogenic therapies. The ability to image VEGF expression in tumours would enable their investigation.

Bevacizumab was chosen for the purpose of imaging VEGF as it is an antibody that binds to all isoforms of VEGF, is readily available and produced to GMP standard. It has a long biological half-life and pharmacokinetic profile which necessitates labelling with a radioisotope with a long half-life to ensure adequate target accumulation prior to imaging. ^{111}Indium was used as the radioisotope for labelling bevacizumab as it has a suitable half-life (67 h), is commonly used for radiolabelling proteins and antibodies and is currently used for numerous applications in clinical nuclear medicine.

5.2.1.2 Synthesis

Synthesis of radiolabelled bevacizumab was achieved using 2-(4-isothiocyanatobenzyl) DTPA to allow labelling of bevacizumab with ^{111}In. This was performed using a simple set of procedures at room temperature and pressure, with satisfactory yields of antibody (≈20%) and very high radiochemical purity (>95%). This is encouraging for translation of the radiotracer into clinical use, as developing this process according to GMP requirements is likely to be a relatively easy process. This will be facilitated by the commercial availability of ^{111}In and bevacizumab at GMP standard. In addition, the synthesis of ^{111}In-bnDTPA-bevacizumab can be performed relatively quickly (<4 h) which is convenient for clinical use.

5.2.1.3 Validation and Characterisation

In vitro competitive inhibition assays confirmed that the conjugation and radiolabelling process did not interfere with the binding of bevacizumab to VEGF. *In vivo* investigation of the radiotracer included biodistribution studies by dissection and SPECT-CT imaging of xenograft bearing mice. ^{111}In-bnDTPA-bevacizumab demonstrated excellent tumour to background organ uptake, with up to 40%ID/g of tracer accumulating in xenografts. In contrast, the mean solid organ uptakes were <8%ID/g.

Peak uptake in xenograft bearing mice occurred at 5 days post injection. This indicates that the optimal imaging time for ^{111}In-bnDTPA-bevacizumab in patients is several days after injection. Indeed, the first clinical studies investigating this tracer in patients with colorectal cancer liver metastases and renal cell cancer found 7 days post injection to provide good visualisation of tumour deposits [137, 145]. A subsequent study in patients with stage III/IV melanoma specifically investigated the pharmacokinetics of ^{111}In-bnDTPA-bevacizumab and found the 4th day post injection to be an optimal time point [138]. These results are confounded by the fact that different doses of tracer were used in the studies, therefore further work will be needed to optimise the dose and timing of imaging in patients.

The requirement for patients to be scanned several days post-injection of tracer is possible but not very practical, especially when considering the logistical constraints of clinical departments. Ideally an imaging agent would be injected and imaged on the same day. Improved kinetics of the tracer can be achieved by using smaller variants of the tracer that retain binding specificity. In the case of antibody-based imaging agents, smaller fragments such as Fab or single chain Fv fragments (FIGURE 64) can be used. In addition, other potential agents are engineered compounds like affibodies and designed ankyrin repeat proteins (DARPins) which offer fast pharmacokinetics, whilst possessing high target specificity and binding affinity [259, 260].

For bevacizumab, there is a commercially available Fab fragment, ranibizumab (Lucentis, Novartis), which has been radiolabelled with ^{89}Zr, a positron-emitting radionuclide. In a murine xenograft model it demonstrated maximal uptake in tumour by 24h post injection, with good tumour visualisation by 3 hours [36]. It has yet to be tested in clinical trials, but has the potential to permit injection and imaging within a single day. Faster pharmacokinetics also facilitates use in preclinical studies, enabling a more dynamic insight into angiogenic mechanisms which would be precluded by long uptake times. It is likely that the future of VEGF imaging will include smaller antibody fragments such as ranibizumab.

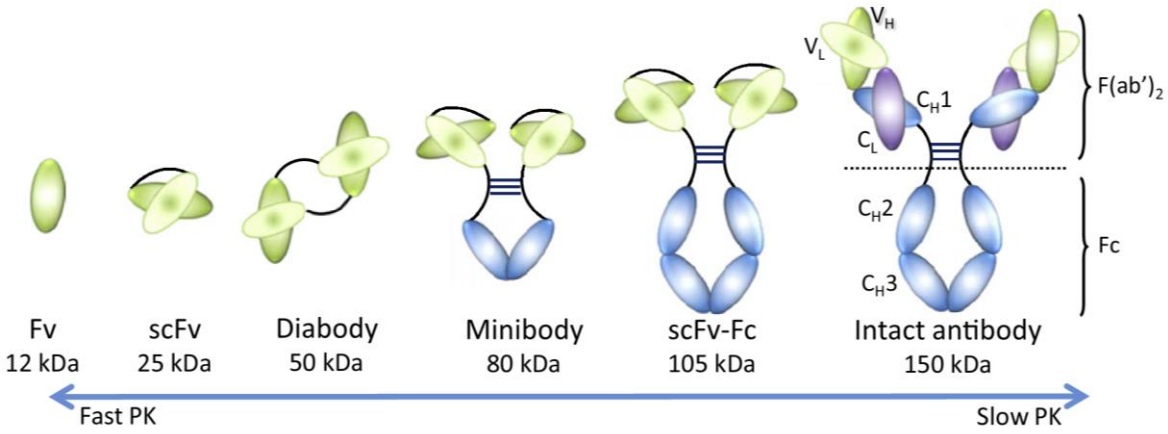


Figure 65: Schematic of different antibody derived imaging agents, engineered from an intact antibody. Fv=single variable domain fragment; scFV=single chain Fv; V_H=variable heavy chain; V_L=variable light chain; C_L=constant light chain; C_H=constant heavy chain. Reproduced with permission from [2]

In vivo studies showed that uptake of ^{111}In-bnDTPA-bevacizumab is specific in xenograft models. Correlation with VEGF levels, however, yielded mixed results. Uptake did not directly reflect VEGF levels as measured by VEGF ELISAs. This is corroborated by similar findings in clinical studies [137, 141] and could be explained by ^{111}In-bnDTPA-bevacizumab uptake reflecting membrane bound isoforms of VEGF such as $VEGF_{165}$ and $VEGF_{189}$ rather than diffusible isoforms such as $VEGF_{121}$. This

is supported by *in vitro* studies that show ^{111}In-bnDTPA-bevacizumab only displays specific binding in competitive binding studies when tumours express $VEGF_{165}$ and $VEGF_{189}$ and not in those expressing $VEGF_{121}$ [136]. This is further suggested by the colocalisation of ^{111}In-bnDTPA-bevacizumab distribution on autoradiographs with immunostaining for bevacizumab and VEGF in the same xenografts. In addition, a recent clinical study in patients with melanoma, used IHC staining intensity of VEGF to correlate with uptake of ^{111}In-bnDTPA-bevacizumab in nine patients, and demonstrated a significant correlation (r=0.75, P=0.017) [138].

5.2.1.4 Future work

These initial results indicate that ^{111}In-bnDTPA-bevacizumab may be a useful tool for investigating the biology of VEGF. More studies are required to further develop it for use as a biomarker of angiogenesis. Future preclinical work will involve evaluation of the relationship of tracer uptake with different angiogenic markers such as VEGFR status, and other microenvironmental factors such as hypoxia. In addition, comparison with other vascular imaging modalities such as DCE-MRI and contrast ultrasound, and other radionuclides for assessing angiogenesis (e.g. ^{99m}Tc-maraciclatide) will help further define its role.

Further clinical development of ^{111}In-bnDTPA-bevacizumab is also required. To this end, a pilot study (APPENDIX B) is being initiated in Oxford with the objectives of investigating the optimal time point for imaging tumours with ^{111}In-bnDTPA-bevacizumab and describing the variation of uptake in different tumour types. Another aim is to compare tumour uptake of tracer with circulating serum markers of angiogenesis such as $VEGF_{121}$, soluble VEGF receptors, and factors associated with hypoxia pathway activation (e.g. osteopontin, stromal cell-derived factor-1 (SDF-1) and hepatocyte growth factor (HGF)). It is hoped that the results of the study will further characterise the utility and significance of ^{111}In-bnDTPA-bevacizumab as an angiogenic imaging agent.

5.2.2 ^{99M}Tc-maraciclatide

5.2.2.1 Rationale

Integrins are a family of cell surface receptors, of which $\alpha_v\beta_3$ and $\alpha_v\beta_5$ are critical for angiogenesis. The RGD tripeptide sequence is a key binding motif for these receptors and has been incorporated into a variety of agents for imaging and inhibition of integrin function. ^{99m}Tc-maraciclatide is a PEGylated RGD molecule developed by GE Healthcare for SPECT imaging that has entered clinical trials. However, only limited published evidence validating its use in imaging angiogenesis is currently available.

5.2.2.2 Preclinical Study

^{99m}Tc-maraciclatide was investigated in a human head and neck (FaDu) cancer xenograft model. It demonstrated significantly lower uptake within the tumour (<2%ID/g) when compared to ^{111}In-bnDTPA-bevacizumab (up to 40%ID/g). However, background organ uptake was also decreased such that tumour to muscle ratios were of comparable magnitude for the two tracers. Despite this, visualisation of tumours in the mice with ^{99m}Tc-maraciclatide SPECT-CT was not possible. This is likely to be related to high renal uptake and clearance of ^{99m}Tc-maraciclatide, which leads to intense activity within the bladder. This results in high levels of scattered radiation in the abdominal cavity, which masks signal from the tumour. In future studies of ^{99m}Tc-maraciclatide the xenograft will be repositioned to the neck, where there is minimal background activity.

5.2.2.3 Clinical Study and Future Work

As for preclinical studies, there was significant uptake and excretion via the kidneys of ^{99m}Tc-maraciclatide. There was also significant activity within the bowel which led to difficulties in visualisation of bowel tumours. Both these factors potentially led to a disparity in uptake profile between renal and colorectal tumours and breast cancers due to high background activity. Renal and colorectal tumours appeared to have an overall higher and narrower range of uptake than breast tumours. Also uptake in the intra-abdominal tumours did not correlate with their size,

type, stage or grade. In contrast, there was a strong correlation between size and uptake of ^{99m}Tc-maraciclatide in breast cancers. There also appeared to be an effect of histological subtype, stage and grade on tumour uptake. These differences may also be related to the relatively small size of tumours within the breast cancer group compared to those of the other two tumour sites.

There was no correlation between ^{99m}Tc-maraciclatide uptake and markers of angiogenesis such as CD31 vascular density (VD), pKDR status, VSA and "edvin" scores. In contrast, there was a moderate negative correlation between ^{99m}Tc-maraciclatide uptake and β_3 integrin VD. This may be attributable to β_3 integrin VD also reflecting $\alpha_{IIB}\beta_3$ levels, to which ^{99m}Tc-maraciclatide does not bind. In addition, ^{99m}Tc-maraciclatide has a high binding affinity for $\alpha_v\beta_5$, which may also confound the correlation. Further work will involve assaying the β_5 integrin subunit levels within the existing tumour specimens, to determine if there is a correlation with ^{99m}Tc-maraciclatide uptake. In addition, a substantial amendment is being submitted to extend the study. Changes to the study protocol will include collection of tumour sample at the time of surgery enabling specimens to be frozen for later immunostaining with whole $\alpha_v\beta_3$ receptor antibody. Acquiring such information should clarify the relationship between ^{99m}Tc-maraciclatide uptake and the different integrins.

It is important to note that direct comparison of the distribution of ^{99m}Tc-maraciclatide in tumours with immunostaining of equivalent tumour sections was not possible because sections for histological analysis were selected randomly. To remedy this, future collection of samples at surgery will involve orientation of the tumour in orthogonal planes. This will enable specimens to be cut in the same plane as the preceding imaging, thus allowing spatial comparisons of uptake and IHC to be performed. This already has been attempted with the latest renal tumours to be resected (FIGURE 65).

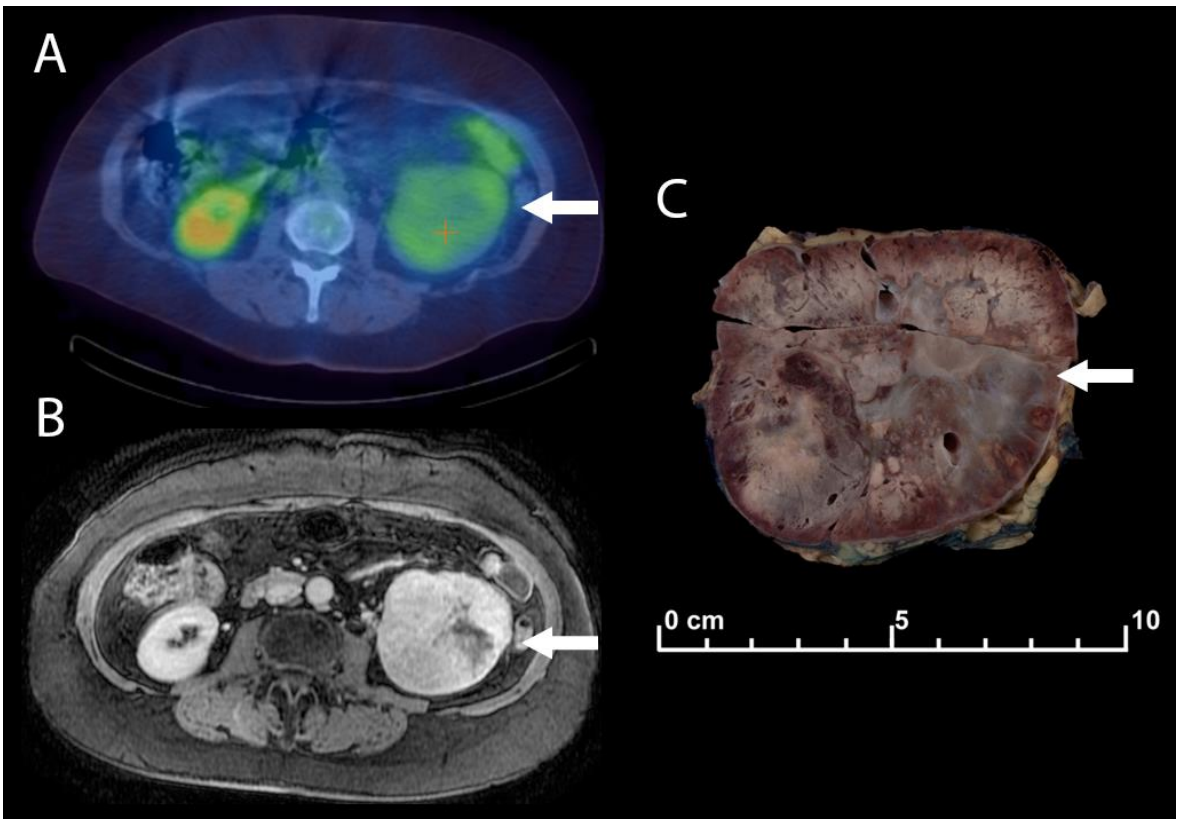


Figure 66: Spatial comparison between imaging and histology. An example of a patient with a left sided renal cell carcinoma. The SPECT-CT (**A**) of ^{99m}Tc-maraciclatide uptake demonstrates a photopaenic region within the tumour (arrow). This corresponds to decreased contrast enhancement (arrow) on DCE-MRI (**B**) and a scar (arrow) in the resected tumour (**C**) cut at the same level and plane as the imaging.

5.2.3 PET versus SPECT

Both ^{111}In-bnDTPA-bevacizumab and ^{99m}Tc-maraciclatide are gamma-emitters and are detected using SPECT. In preclinical studies SPECT is an adequate means for assessing uptake as quantification is relatively easy and spatial resolution is comparable to PET imaging. In oncological clinical imaging use of gamma-emitters poses a challenge as accurate quantification and characterisation of spatial distribution of tumour uptake is required. This is particularly relevant to these two agents, which are likely to be used for characterisation rather than detection of tumours.

PET imaging provides a more attractive method for imaging radionuclides as it possesses a number of advantages over SPECT. These include greater sensitivity, better spatial and temporal

resolution, lower radiation dose and quantitative capability. Of particular importance is the ability of PET to quantify the amount of radioactivity within a given volume. For SPECT this is generally less robust or not available, therefore relative methods of assessing tumour uptake such as comparison with background uptake are employed.

Ideally ^{111}In-bnDTPA-bevacizumab and ^{99m}Tc-maraciclatide would be developed further as PET tracers. Bevacizumab has been radiolabelled previously with several long-lived PET tracers such as ^{89}Zr (T½= 3.3d) [35], ^{86}Y (T½ = 14.7h) [131], ^{64}Cu (T½ =12.7h)[130] and ^{124}I (T½ =4.2d) [132]. ^{99m}Tc-maraciclatide has an equivalent PET tracer, ^{18}F-fluciclatide, which has similar binding and distribution characteristics [261]. It is likely that clinical adoption will involve positron-emitting versions of the tracers due to the advantages of PET imaging. For future work in Oxford ^{18}F-fluciclatide will supersede ^{99m}Tc-maraciclatide, with the intention of making the imaging assessments more accurate and quantifiable.

5.3 Therapeutic response assessment

It is envisaged that both VEGF and integrin imaging will guide clinical management of patients by predicting and assessing response to antiangiogenic therapy. To investigate the potential of these imaging strategies in detecting response to therapy, ^{111}In-bnDTPA-bevacizumab and ^{99m}Tc-maraciclatide were used in a preclinical xenograft model with antiangiogenic therapy.

For both tracers rapamycin therapy was administered to FaDu xenograft-bearing mice. Rapamycin is an mTOR inhibitor which suppresses HIF-1α levels to inhibit angiogenesis. In the studies presented in this thesis, rapamycin led to vessel reduction with decreased mean vessel density and increased overall vessel diameter. Its effects on blood vessels were also demonstrated with DCE-MRI. In the small group of mice that were imaged, IAUGC and the fraction of enhancing voxels appeared to decrease, indicating decreased vascular permeability and perfusion of the tumours. Rapamycin also appeared to increase VEGF within the tumours, with most significant effect on the $VEGF_{165}$ isoform. This may be a reflection of the predominance

and importance of $VEGF_{165}$ over the other isoforms [262]. Uptake of ^{111}In-bnDTPA-bevacizumab exhibited similar changes to VEGF levels, with significantly increased tracer uptake in treated mice. Rapamycin also appeared to decrease β_3 integrin levels and this was mirrored by a significant decrease in ^{99m}Tc-maraciclatide uptake.

The effects of non-radiolabelled bevacizumab, an anti-VEGF antibody, on uptake of ^{99m}Tc-maraciclatide was also investigated. Its binding to VEGF precluded its use in evaluating uptake changes of ^{111}In-bnDTPA-bevacizumab. Treatment with bevacizumab appeared to have an effect on blood vessel morphology, however given the small number of mice that were analysed, it was not possible to determine the statistical significance of this change. Bevacizumab treatment of mice did not lead to significant changes in either β_3 integrin levels or in ^{99m}Tc-maraciclatide uptake.

5.3.1 Future work

These initial results are encouraging as they indicate that changes in tumour vessels caused by antiangiogenic therapies can be detected by both imaging agents and that they correspond with changes in the relevant angiogenic markers. Further preclinical work is needed to fully understand the significance of these results and to establish their applicability to other tumour models and antiangiogenic therapies. In addition, future imaging studies with ^{99m}Tc-maraciclatide should be performed with xenografts placed in the neck to enable longitudinal assessment of therapeutic effects in individual mice.

Clinical evaluation of the effects of antiangiogenic therapies on VEGF or integrin imaging is limited with only two reported studies investigating the effects of antiangiogenic therapy on ^{111}In-bnDTPA-bevacizumab uptake and none for integrin imaging. To develop this field a clinical trial is about to open in Oxford to investigate the effects of TKI therapy on uptake of ^{18}F-fluciclatide in renal cell carcinoma. The aims of the trial are to determine whether ^{18}F-fluciclatide can be used to predict and assess therapeutic response. Patients will be scanned prior to therapy and after the

first and third cycles of treatment (FIGURE 66). Changes in uptake will be compared with standard clinical staging by CT, changes in perfusion CT parameters and clinical outcome (PFS and OS) (see APPENDIX B for trial synopsis). It is hoped that this trial will help provide evidence for the clinical use of radionuclide angiogenesis imaging.

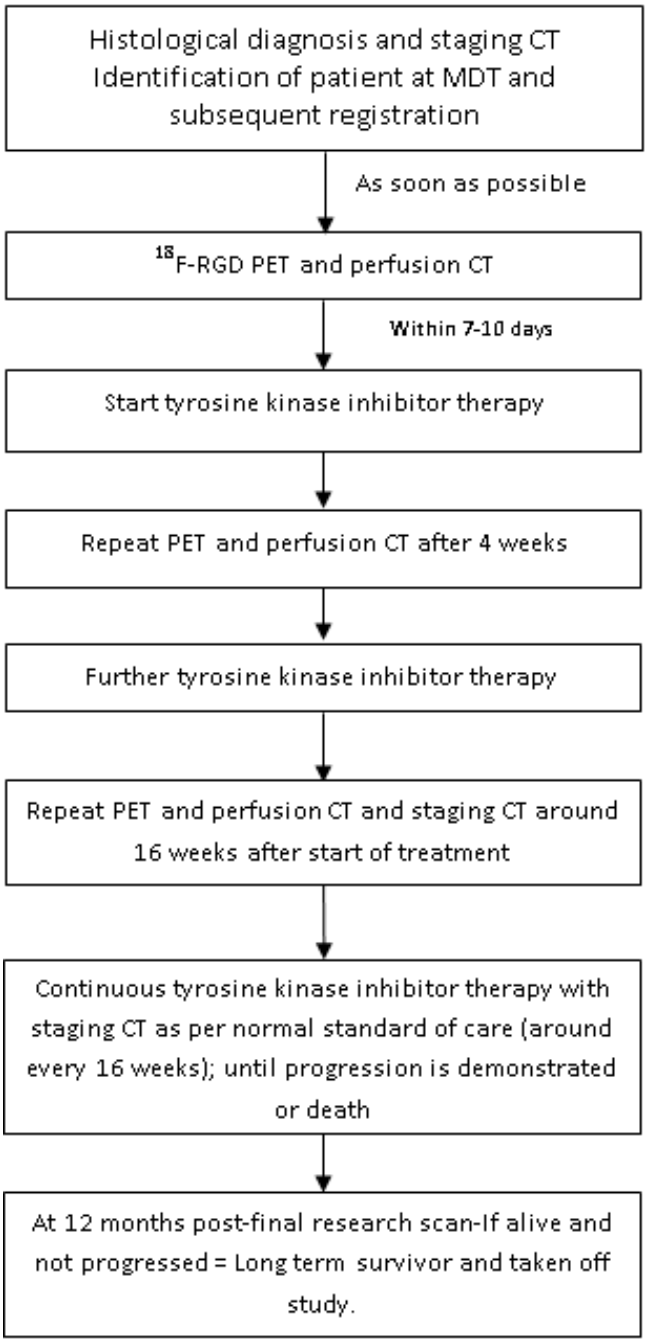


Figure 67: Fluciclatide trial. Trial procedures for investigation of the effect of TKIs in RCC on ^{18}F-fluciclatide uptake

5.4 Summary

Imaging of angiogenesis has been growing rapidly over the past few years. There are now multiple modalities with numerous techniques and imaging agents directed at accurately assessing angiogenesis. Functional techniques such as DCE-MRI have the advantage of being readily available and easily implemented with existing resources. On the other hand complex analyses of the images are often required and the derived parameters do not necessarily correlate directly with physiological processes. In comparison, targeted techniques, such as radionuclide imaging, are readily more quantifiable and physiologically relevant. They, however, are expensive and require considerable added resources such as on-site chemistry and radionuclide production facilities.

As angiogenesis involves a complex and dynamic interplay of structural and physiological processes, it is unlikely that one method of assessment at a single timepoint will provide a representative view. Rather multimodal and multiple timepoint imaging will allow comprehensive evaluation of the angiogenic process. In the future, imaging will increasingly involve the combination of modalities such as PET-CT and PET-MRI to couple functional and molecular aspects into a composite image of angiogenesis.

5.4.1 Conclusion

Treatments directed against angiogenesis will play a key role in the future of cancer medicine. It follows that robust methods for real-time assessment of angiogenesis are required for effective clinical management and for the development of new antiangiogenesis therapeutics. Radiotracers such as ^{111}In-bnDTPA-bevacizumab and ^{99m}Tc-maraciclatide hold promise as imaging agents that will help elucidate the complex and dynamic interplay of physiological processes that govern angiogenesis. It is also hoped that they will eventually be used to help guide clinical management of patients with cancer.

Appendix A: References

1. Edwards, D., et al., *99mTc-NC100692--a tracer for imaging vitronectin receptors associated with angiogenesis: a preclinical investigation.* Nucl Med Biol, 2008. **35**(3): p. 365-75.
2. Olafsen, T. and A.M. Wu, *Antibody Vectors for Imaging.* Seminars in Nuclear Medicine, 2010. **40**(3): p. 167-181.
3. Giatromanolaki, A., et al., *Differential Assessment of Vascular Survival Ability and Tumor Angiogenic Activity in Colorectal Cancer.* Clinical Cancer Research, 2002. **8**(5): p. 1185-1191.
4. Herbert, S.P. and D.Y. Stainier, *Molecular control of endothelial cell behaviour during blood vessel morphogenesis.* Nat Rev Mol Cell Biol, 2011. **12**(9): p. 551-64.
5. Hanahan, D. and J. Folkman, *Patterns and emerging mechanisms of the angiogenic switch during tumorigenesis.* Cell, 1996. **86**(3): p. 353-64.
6. Carmeliet, P., *VEGF as a key mediator of angiogenesis in cancer.* Oncology, 2005. **69 Suppl 3**: p. 4-10.
7. Fukumura, D. and R.K. Jain, *Imaging angiogenesis and the microenvironment.* APMIS, 2008. **116**(7-8): p. 695-715.
8. Schneider, B.P., M. Radovich, and K.D. Miller, *The role of vascular endothelial growth factor genetic variability in cancer.* Clin Cancer Res, 2009. **15**(17): p. 5297-302.
9. Hood, J.D. and D.A. Cheresh, *Role of integrins in cell invasion and migration.* Nat Rev Cancer, 2002. **2**(2): p. 91-100.
10. Sakurai, T. and M. Kudo, *Signaling pathways governing tumor angiogenesis.* Oncology, 2011. **81 Suppl 1**: p. 24-9.
11. Nagy, J.A. and H.F. Dvorak, *Heterogeneity of the tumor vasculature: the need for new tumor blood vessel type-specific targets.* Clin Exp Metastasis, 2012.
12. Goel, S., A.H. Wong, and R.K. Jain, *Vascular normalization as a therapeutic strategy for malignant and nonmalignant disease.* Cold Spring Harb Perspect Med, 2012. **2**(3): p. a006486.
13. Azam, F., S. Mehta, and A.L. Harris, *Mechanisms of resistance to antiangiogenesis therapy.* European Journal of Cancer, 2010. **In Press, Corrected Proof**.
14. Bridges, E.M. and A.L. Harris, *The angiogenic process as a therapeutic target in cancer.* Biochemical Pharmacology, 2011. **81**(10): p. 1183-1191.
15. Zuniga, R.M., et al., *Efficacy, safety and patterns of response and recurrence in patients with recurrent high-grade gliomas treated with bevacizumab plus irinotecan.* J Neurooncol, 2009. **91**(3): p. 329-36.
16. Shojaei, F., et al., *Tumor refractoriness to anti-VEGF treatment is mediated by CD11b+Gr1+ myeloid cells.* Nat Biotech, 2007. **25**(8): p. 911-920.
17. Jayson, G.C., D.J. Hicklin, and L.M. Ellis, *Antiangiogenic therapy - evolving view based on clinical trial results.* Nat Rev Clin Oncol, 2012. **9**(5): p. 297-303.
18. Ellis, L.M., R.A. Walker, and G. Gasparini, *Is determination of angiogenic activity in human tumours clinically useful?* Eur J Cancer, 1998. **34**(5): p. 609-18.
19. Maniotis, A.J., et al., *Vascular Channel Formation by Human Melanoma Cells in Vivo and in Vitro: Vasculogenic Mimicry.* The American Journal of Pathology, 1999. **155**(3): p. 739-752.
20. te Velde, E.A., et al., *The use of fluorescent dyes and probes in surgical oncology.* European Journal of Surgical Oncology (EJSO), 2010. **36**(1): p. 6-15.
21. Kiessling, F., D. Razansky, and F. Alves, *Anatomical and microstructural imaging of angiogenesis.* Eur J Nucl Med Mol Imaging, 2010. **37 Suppl 1**: p. S4-19.

22. Bowden, D.J. and T. Barrett, *Angiogenesis imaging in neoplasia.* J Clin Imaging Sci, 2011. **1**: p. 38.
23. Golman, K., et al., *Molecular imaging using hyperpolarized 13C.* Br J Radiol, 2003. **76 Spec No 2**: p. S118-27.
24. Maglione, D., et al., *Isolation of a human placenta cDNA coding for a protein related to the vascular permeability factor.* Proc Natl Acad Sci U S A, 1991. **88**(20): p. 9267-71.
25. Huang, K., et al., *Signaling properties of VEGF receptor-1 and -2 homo- and heterodimers.* The International Journal of Biochemistry & Cell Biology, 2001. **33**(4): p. 315-324.
26. Nilsson, I., et al., *VEGF receptor 2/-3 heterodimers detected in situ by proximity ligation on angiogenic sprouts.* EMBO J, 2010. **29**(8): p. 1377-88.
27. Grünewald, F.S., et al., *Structure–function analysis of VEGF receptor activation and the role of coreceptors in angiogenic signaling.* Biochimica et Biophysica Acta (BBA) - Proteins & Proteomics, 2010. **1804**(3): p. 567-580.
28. Gluzman-Poltorak, Z., et al., *Vascular Endothelial Growth Factor Receptor-1 and Neuropilin-2 Form Complexes.* Journal of Biological Chemistry, 2001. **276**(22): p. 18688-18694.
29. Mahabeleshwar, G.H., et al., *Integrin affinity modulation in angiogenesis.* Cell Cycle, 2008. **7**(3): p. 335-47.
30. Waltenberger, J., et al., *Different signal transduction properties of KDR and Flt1, two receptors for vascular endothelial growth factor.* J Biol Chem, 1994. **269**(43): p. 26988-95.
31. Hornig, C., et al., *Release and complex formation of soluble VEGFR-1 from endothelial cells and biological fluids.* Lab Invest, 2000. **80**(4): p. 443-54.
32. Kendall, R.L. and K.A. Thomas, *Inhibition of vascular endothelial cell growth factor activity by an endogenously encoded soluble receptor.* Proc Natl Acad Sci U S A, 1993. **90**(22): p. 10705-9.
33. Shibuya, M. and L. Claesson-Welsh, *Signal transduction by VEGF receptors in regulation of angiogenesis and lymphangiogenesis.* Experimental Cell Research, 2006. **312**(5): p. 549-560.
34. Collingridge, D.R., et al., *The Development of [124I]Iodinated-VG76e: A Novel Tracer for Imaging Vascular Endothelial Growth Factor in Vivo Using Positron Emission Tomography.* Cancer Res, 2002. **62**(20): p. 5912-5919.
35. Nagengast, W.B., et al., *In Vivo VEGF Imaging with Radiolabeled Bevacizumab in a Human Ovarian Tumor Xenograft.* J Nucl Med, 2007. **48**(8): p. 1313-1319.
36. Nagengast, W.B., et al., *VEGF-PET Imaging Is a Noninvasive Biomarker Showing Differential Changes in the Tumor during Sunitinib Treatment.* Cancer Research, 2011. **71**(1): p. 143-153.
37. Chen, K., et al., *Quantitative PET Imaging of VEGF Receptor Expression.* Molecular Imaging and Biology, 2009. **11**(1): p. 15-22.
38. Wang, H., et al., *A new PET tracer specific for vascular endothelial growth factor receptor 2.* European Journal of Nuclear Medicine and Molecular Imaging, 2007. **34**(12): p. 2001-2010.
39. Blankenberg, F., et al., *In vivo tumor angiogenesis imaging with site-specific labeled 99mTc-HYNIC-VEGF.* European Journal of Nuclear Medicine and Molecular Imaging, 2006. **33**(7): p. 841-848.
40. Qin, Z.-x., et al., *Imaging targeted at tumor with 188Re-labeled VEGF189 exon 6-encoded peptide and effects of the transfecting truncated KDR gene in tumor-bearing nude mice.* Nuclear Medicine and Biology, 2009. **36**(5): p. 535-543.
41. Pysz, M.A., et al., *Antiangiogenic Cancer Therapy: Monitoring with Molecular US and a Clinically Translatable Contrast Agent (BR55)1.* Radiology, 2010. **256**(2): p. 519-527.
42. Brooks, P.C., R.A. Clark, and D.A. Cheresh, *Requirement of vascular integrin alpha v beta 3 for angiogenesis.* Science, 1994. **264**(5158): p. 569-71.

43. Ernst Michael, J., et al., *Contrast enhanced harmonic ultrasound for differentiating breast tumors - First results.* Clinical Hemorheology and Microcirculation, 2005. **33**(2): p. 109-120.
44. Sipkins, D.A., et al., *Detection of tumor angiogenesis in vivo by alphaVbeta3-targeted magnetic resonance imaging.* Nat Med, 1998. **4**(5): p. 623-6.
45. Haubner, R., et al., *Radiolabeled αvβ3 Integrin Antagonists: A New Class of Tracers for Tumor Targeting.* Journal of Nuclear Medicine, 1999. **40**(6): p. 1061-1071.
46. Haubner, R., *Alphavbeta3-integrin imaging: a new approach to characterise angiogenesis?* Eur J Nucl Med Mol Imaging, 2006. **33 Suppl 1**: p. 54-63.
47. Chen, X., et al., *Pharmacokinetics and tumor retention of 125I-labeled RGD peptide are improved by PEGylation.* Nuclear Medicine and Biology, 2004. **31**(1): p. 11-19.
48. Wu, Y., et al., *microPET Imaging of Glioma Integrin αvβ3 Expression Using 64Cu-Labeled Tetrameric RGD Peptide.* Journal of Nuclear Medicine, 2005. **46**(10): p. 1707-1718.
49. Montet, X., et al., *Nanoparticle imaging of integrins on tumor cells.* Neoplasia, 2006. **8**(3): p. 214-22.
50. Haubner, R., et al., *Noninvasive Visualization of the Activated αvβ3 Integrin in Cancer Patients by Positron Emission Tomography and [18F]Galacto-RGD.* PLoS Med, 2005. **2**(3): p. e70.
51. Beer, A.J., et al., *Positron emission tomography using [18F]Galacto-RGD identifies the level of integrin alpha(v)beta3 expression in man.* Clin Cancer Res, 2006. **12**(13): p. 3942-9.
52. Beer, A.J., et al., *Comparison of Integrin αvβ3 Expression and Glucose Metabolism in Primary and Metastatic Lesions in Cancer Patients: A PET Study Using 18F-Galacto-RGD and 18F-FDG.* Journal of Nuclear Medicine, 2008. **49**(1): p. 22-29.
53. Kenny, L.M., et al., *Phase I trial of the positron-emitting Arg-Gly-Asp (RGD) peptide radioligand 18F-AH111585 in breast cancer patients.* J Nucl Med, 2008. **49**(6): p. 879-86.
54. Glaser, M., et al., *Radiosynthesis and Biodistribution of Cyclic RGD Peptides Conjugated with Novel [18F]Fluorinated Aldehyde-Containing Prosthetic Groups.* Bioconjugate Chemistry, 2008. **19**(4): p. 951-957.
55. Axelsson, R., et al., *An open-label, multicenter, phase 2a study to assess the feasibility of imaging metastases in late-stage cancer patients with the αvβ3-selective angiogenesis imaging agent 99mtc-nc100692.* Acta Radiologica, 2010. **51**(1): p. 40-46.
56. Doss, M., et al., *Biodistribution and Radiation Dosimetry of the Integrin Marker 18F-RGD-K5 Determined from Whole-Body PET/CT in Monkeys and Humans.* Journal of Nuclear Medicine, 2012. **53**(5): p. 787-795.
57. Mittra, E.S., et al., *Pilot Pharmacokinetic and Dosimetric Studies of 18F-FPPRGD2: A PET Radiopharmaceutical Agent for Imaging αvβ3 Integrin Levels.* Radiology, 2011. **260**(1): p. 182-191.
58. Battle, M.R., et al., *Monitoring Tumor Response to Antiangiogenic Sunitinib Therapy with 18F-Fluciclatide, an 18F-Labeled αVβ3-Integrin and αVβ5-Integrin Imaging Agent.* Journal of Nuclear Medicine, 2011. **52**(3): p. 424-430.
59. Hong, H., et al., *Positron emission tomography imaging of CD105 expression during tumor angiogenesis.* European Journal of Nuclear Medicine and Molecular Imaging, 2011. **38**(7): p. 1335-1343.
60. Seaman, S., et al., *Genes that Distinguish Physiological and Pathological Angiogenesis.* Cancer Cell, 2007. **11**(6): p. 539-554.
61. Jeswani, T. and A.R. Padhani, *Imaging tumour angiogenesis.* Cancer Imaging, 2005. **5**: p. 131-8.
62. Tofts, P.S., et al., *Estimating kinetic parameters from dynamic contrast-enhanced T(1)-weighted MRI of a diffusable tracer: standardized quantities and symbols.* J Magn Reson Imaging, 1999. **10**(3): p. 223-32.

63. Turkbey, B., et al., *The role of dynamic contrast-enhanced MRI in cancer diagnosis and treatment.* Diagn Interv Radiol, 2010. **16**(3): p. 186-92.
64. Lankester, K.J., et al., *Dynamic MRI for imaging tumor microvasculature: Comparison of susceptibility and relaxivity techniques in pelvic tumors.* Journal of Magnetic Resonance Imaging, 2007. **25**(4): p. 796-805.
65. Lipnick, S., et al., *Combined DCE-MRI and single-voxel 2D MRS for differentiation between benign and malignant breast lesions.* NMR in Biomedicine, 2010. **23**(8): p. 922-930.
66. Kim, S., et al., *Prediction of Response to Chemoradiation Therapy in Squamous Cell Carcinomas of the Head and Neck Using Dynamic Contrast-Enhanced MR Imaging.* American Journal of Neuroradiology, 2010. **31**(2): p. 262-268.
67. Kummar, S., et al., *Phase I trial of vandetanib and bevacizumab evaluating the VEGF and EGF signal transduction pathways in adults with solid tumours and lymphomas.* European Journal of Cancer, 2011. **47**(7): p. 997-1005.
68. Li, S.P. and A.R. Padhani, *Tumor response assessments with diffusion and perfusion MRI.* Journal of Magnetic Resonance Imaging, 2012. **35**(4): p. 745-763.
69. Mehta, S., et al., *Assessing Early Therapeutic Response to Bevacizumab in Primary Breast Cancer Using Magnetic Resonance Imaging and Gene Expression Profiles.* JNCI Monographs, 2011. **2011**(43): p. 71-74.
70. Cao, Y., *The Promise of Dynamic Contrast-Enhanced Imaging in Radiation Therapy.* Seminars in Radiation Oncology, 2011. **21**(2): p. 147-156.
71. Drevs, J., et al., *Phase I Clinical Study of AZD2171, an Oral Vascular Endothelial Growth Factor Signaling Inhibitor, in Patients With Advanced Solid Tumors.* Journal of Clinical Oncology, 2007. **25**(21): p. 3045-3054.
72. Hahn, O.M., et al., *Dynamic Contrast-Enhanced Magnetic Resonance Imaging Pharmacodynamic Biomarker Study of Sorafenib in Metastatic Renal Carcinoma.* Journal of Clinical Oncology, 2008. **26**(28): p. 4572-4578.
73. Aboagye, E., et al., *Recommendations for measurement of tumour vascularity with positron emission tomography in early phase clinical trials.* European Radiology, 2012. **22**(7): p. 1465-1478.
74. Laking, G. and P. Price, *Radionuclide imaging of perfusion and hypoxia.* European Journal of Nuclear Medicine and Molecular Imaging, 2010. **37**(0): p. 20-29.
75. Anderson, H.L., et al., *Assessment of Pharmacodynamic Vascular Response in a Phase I Trial of Combretastatin A4 Phosphate.* Journal of Clinical Oncology, 2003. **21**(15): p. 2823-2830.
76. Ferrara, N., *VEGF and the quest for tumour angiogenesis factors.* Nat Rev Cancer, 2002. **2**(10): p. 795-803.
77. Hicklin, D.J. and L.M. Ellis, *Role of the Vascular Endothelial Growth Factor Pathway in Tumor Growth and Angiogenesis.* J Clin Oncol, 2005. **23**(5): p. 1011-1027.
78. Tischer, E., et al., *The human gene for vascular endothelial growth factor. Multiple protein forms are encoded through alternative exon splicing.* Journal of Biological Chemistry, 1991. **266**(18): p. 11947-11954.
79. Houck, K.A., et al., *The Vascular Endothelial Growth Factor Family: Identification of a Fourth Molecular Species and Characterization of Alternative Splicing of RNA.* Molecular Endocrinology, 1991. **5**(12): p. 1806-1814.
80. Park, J.E., G.A. Keller, and N. Ferrara, *The vascular endothelial growth factor (VEGF) isoforms: differential deposition into the subepithelial extracellular matrix and bioactivity of extracellular matrix-bound VEGF.* Molecular Biology of the Cell, 1993. **4**(12): p. 1317-26.
81. Rennel, E.S., et al., *Recombinant human VEGF165b protein is an effective anti-cancer agent in mice.* European Journal of Cancer, 2008. **44**(13): p. 1883-1894.

82. Shweiki, D., et al., *Vascular endothelial growth factor induced by hypoxia may mediate hypoxia-initiated angiogenesis.* Nature, 1992. **359**(6398): p. 843-5.
83. Rak, J., et al., *Oncogenes and angiogenesis: signaling three-dimensional tumor growth.* J Investig Dermatol Symp Proc, 2000. **5**(1): p. 24-33.
84. Semenza, G.L., *Hypoxia, Clonal Selection, and the Role of HIF-1 in Tumor Progression.* Critical Reviews in Biochemistry and Molecular Biology, 2000. **35**(2): p. 71-103.
85. Levy, A.P., N.S. Levy, and M.A. Goldberg, *Post-transcriptional Regulation of Vascular Endothelial Growth Factor by Hypoxia.* Journal of Biological Chemistry, 1996. **271**(5): p. 2746-2753.
86. Tran, J., et al., *Marked Induction of the IAP Family Antiapoptotic Proteins Survivin and XIAP by VEGF in Vascular Endothelial Cells.* Biochemical and Biophysical Research Communications, 1999. **264**(3): p. 781-788.
87. Unemori, E.N., et al., *Vascular endothelial growth factor induces interstitial collagenase expression in human endothelial cells.* Journal of Cellular Physiology, 1992. **153**(3): p. 557-562.
88. Gabrilovich, D.I., et al., *Production of vascular endothelial growth factor by human tumors inhibits the functional maturation of dendritic cells.* Nat Med, 1996. **2**(10): p. 1096-103.
89. Lichtenberger, B.M., et al., *Autocrine VEGF signaling synergizes with EGFR in tumor cells to promote epithelial cancer development.* Cell, 2010. **140**(2): p. 268-79.
90. Bellamy, W.T., et al., *Expression of vascular endothelial growth factor and its receptors in hematopoietic malignancies.* Cancer Res, 1999. **59**(3): p. 728-33.
91. Decaussin, M., et al., *Expression of vascular endothelial growth factor (VEGF) and its two receptors (VEGF-R1-Flt1 and VEGF-R2-Flk1/KDR) in non-small cell lung carcinomas (NSCLCs): correlation with angiogenesis and survival.* J Pathol, 1999. **188**(4): p. 369-77.
92. Masood, R., et al., *Vascular endothelial growth factor (VEGF) is an autocrine growth factor for VEGF receptor–positive human tumors.* Blood, 2001. **98**(6): p. 1904-1913.
93. Xue, Y., et al., *Anti-VEGF agents confer survival advantages to tumor-bearing mice by improving cancer-associated systemic syndrome.* Proc Natl Acad Sci U S A, 2008. **105**(47): p. 18513-8.
94. Jubb, A.M., et al., *Expression of vascular endothelial growth factor, hypoxia inducible factor 1alpha, and carbonic anhydrase IX in human tumours.* J Clin Pathol, 2004. **57**(5): p. 504-12.
95. Hyodo, I., et al., *Clinical significance of plasma vascular endothelial growth factor in gastrointestinal cancer.* European Journal of Cancer, 1998. **34**(13): p. 2041-2045.
96. Lee, J.C., et al., *Prognostic value of vascular endothelial growth factor expression in colorectal cancer patients.* European Journal of Cancer, 2000. **36**(6): p. 748-753.
97. Toi, M., et al., *Association of vascular endothelial growth factor expression with tumor angiogenesis and with early relapse in primary breast cancer.* Jpn J Cancer Res, 1994. **85**(10): p. 1045-9.
98. Jubb, A.M., et al., *Predicting benefit from anti-angiogenic agents in malignancy.* Nat Rev Cancer, 2006. **6**(8): p. 626-635.
99. Saharinen, P., et al., *VEGF and angiopoietin signaling in tumor angiogenesis and metastasis.* Trends in Molecular Medicine, 2011. **17**(7): p. 347-362.
100. Finley, S.D., et al., *Pharmacokinetics and pharmacodynamics of VEGF-neutralizing antibodies.* BMC Syst Biol, 2011. **5**: p. 193.
101. Matsubayashi, R., et al., *Breast Masses with Peripheral Rim Enhancement on Dynamic Contrast-enhanced MR Images: Correlation of MR Findings with Histologic Features and Expression of Growth Factors1.* Radiology, 2000. **217**(3): p. 841-848.
102. Hoang, B.H., et al., *VEGF expression in osteosarcoma correlates with vascular permeability by dynamic MRI.* Clin Orthop Relat Res, 2004(426): p. 32-8.

103. Bajpai, J., et al., *Noninvasive imaging surrogate of angiogenesis in osteosarcoma.* Pediatr Blood Cancer, 2010. **54**(4): p. 526-31.
104. Su, M.Y., et al., *Correlation of dynamic contrast enhancement MRI parameters with microvessel density and VEGF for assessment of angiogenesis in breast cancer.* J Magn Reson Imaging, 2003. **18**(4): p. 467-77.
105. Wang, B., Z.Q. Gao, and X. Yan, *Correlative study of angiogenesis and dynamic contrast-enhanced magnetic resonance imaging features of hepatocellular carcinoma.* Acta Radiol, 2005. **46**(4): p. 353-8.
106. Zhang, J.H., et al., *Correlation of CT Perfusion Images with VEGF Expression in Solitary Brain Metastases.* Asian Pac J Cancer Prev, 2012. **13**(4): p. 1575-8.
107. Yao, J., et al., *Gastric adenocarcinoma: can perfusion CT help to noninvasively evaluate tumor angiogenesis?* Abdom Imaging, 2011. **36**(1): p. 15-21.
108. Ma, S.H., et al., *Peripheral pulmonary nodules: relationship between multi-slice spiral CT perfusion imaging and tumor angiogenesis and VEGF expression.* BMC Cancer, 2008. **8**: p. 186.
109. Jiang, H.J., et al., *Quantification of angiogenesis by CT perfusion imaging in liver tumor of rabbit.* Hepatobiliary Pancreat Dis Int, 2009. **8**(2): p. 168-73.
110. Jayson, G.C., et al., *Molecular Imaging and Biological Evaluation of HuMV833 Anti-VEGF Antibody: Implications for Trial Design of Antiangiogenic Antibodies.* J. Natl. Cancer Inst., 2002. **94**(19): p. 1484-1493.
111. Foersch, S., et al., *Molecular imaging of VEGF in gastrointestinal cancer in vivo using confocal laser endomicroscopy.* Gut, 2010. **59**(8): p. 1046-55.
112. Hsieh, W.J., et al., *In vivo tumor targeting and imaging with anti-vascular endothelial growth factor antibody-conjugated dextran-coated iron oxide nanoparticles.* Int J Nanomedicine, 2012. **7**: p. 2833-42.
113. Liu, Y., et al., *Gadolinium-loaded polymeric nanoparticles modified with Anti-VEGF as multifunctional MRI contrast agents for the diagnosis of liver cancer.* Biomaterials, 2011. **32**(22): p. 5167-5176.
114. Chen, J., et al., *Using anti-VEGF McAb and magnetic nanoparticles as double-targeting vector for the radioimmunotherapy of liver cancer.* Cancer Letters, 2006. **231**(2): p. 169-175.
115. Presta, L.G., et al., *Humanization of an Anti-Vascular Endothelial Growth Factor Monoclonal Antibody for the Therapy of Solid Tumors and Other Disorders.* Cancer Res, 1997. **57**(20): p. 4593-4599.
116. Varey, A.H., et al., *VEGF 165 b, an antiangiogenic VEGF-A isoform, binds and inhibits bevacizumab treatment in experimental colorectal carcinoma: balance of pro- and antiangiogenic VEGF-A isoforms has implications for therapy.* Br J Cancer, 2008. **98**(8): p. 1366-79.
117. Liang, W.-C., et al., *Cross-species Vascular Endothelial Growth Factor (VEGF)-blocking Antibodies Completely Inhibit the Growth of Human Tumor Xenografts and Measure the Contribution of Stromal VEGF.* Journal of Biological Chemistry, 2006. **281**(2): p. 951-961.
118. Lin, Y.S., et al., *Preclinical pharmacokinetics, interspecies scaling, and tissue distribution of a humanized monoclonal antibody against vascular endothelial growth factor.* J Pharmacol Exp Ther, 1999. **288**(1): p. 371-8.
119. Lu, J.-F., et al., *Clinical pharmacokinetics of bevacizumab in patients with solid tumors.* Cancer Chemotherapy and Pharmacology, 2008. **62**(5): p. 779-786.
120. Gerber, H.-P. and N. Ferrara, *Pharmacology and Pharmacodynamics of Bevacizumab as Monotherapy or in Combination with Cytotoxic Therapy in Preclinical Studies.* Cancer Res, 2005. **65**(3): p. 671-680.
121. Shih, T. and C. Lindley, *Bevacizumab: An angiogenesis inhibitor for the treatment of solid malignancies.* Clinical Therapeutics, 2006. **28**(11): p. 1779-1802.

122. Jenab-Wolcott, J. and B.J. Giantonio, *Bevacizumab: current indications and future development for management of solid tumors.* Expert Opinion on Biological Therapy, 2009. **9**(4): p. 507-517.
123. Kim, K.J., et al., *Inhibition of vascular endothelial growth factor-induced angiogenesis suppresses tumour growth in vivo.* Nature, 1993. **362**(6423): p. 841-4.
124. Grothey, A., et al., *Bevacizumab beyond first progression is associated with prolonged overall survival in metastatic colorectal cancer: results from a large observational cohort study (BRiTE).* J Clin Oncol, 2008. **26**(33): p. 5326-34.
125. *FDA approval for bevacizumab*. 2011; Available from: http://www.cancer.gov/cancertopics/druginfo/fda-bevacizumab.
126. Terwisscha van Scheltinga, A.G.T., et al., *Intraoperative Near-Infrared Fluorescence Tumor Imaging with Vascular Endothelial Growth Factor and Human Epidermal Growth Factor Receptor 2 Targeting Antibodies.* Journal of Nuclear Medicine, 2011. **52**(11): p. 1778-1785.
127. Withrow, K.P., et al., *Assessment of bevacizumab conjugated to Cy5.5 for detection of head and neck cancer xenografts.* Technol Cancer Res Treat, 2008. **7**(1): p. 61-6.
128. Zhang, L., et al., *Multifunctional microbubbles for image-guided antivascular endothelial growth factor therapy.* J Biomed Opt, 2010. **15**(3): p. 030515.
129. Nagengast, W.B., et al., *89Zr-Bevacizumab PET of Early Antiangiogenic Tumor Response to Treatment with HSP90 Inhibitor NVP-AUY922.* J Nucl Med, 2010. **51**(5): p. 761-767.
130. Paudyal, B., et al., *Positron emission tomography imaging and biodistribution of vascular endothelial growth factor with 64Cu-labeled bevacizumab in colorectal cancer xenografts.* Cancer Sci, 2011. **102**(1): p. 117-21.
131. Nayak, T.K., et al., *PET imaging of tumor angiogenesis in mice with VEGF-A targeted (86)Y-CHX-A"-DTPA-bevacizumab.* International Journal of Cancer, 2010. **9999**(999A): p. NA.
132. Christoforidis, J.B., et al., *PET/CT Imaging of I-124–Radiolabeled Bevacizumab and Ranibizumab after Intravitreal Injection in a Rabbit Model.* Investigative Ophthalmology & Visual Science, 2011. **52**(8): p. 5899-5903.
133. Zhang, Y., et al., *Positron Emission Tomography and Near-Infrared Fluorescence Imaging of Vascular Endothelial Growth Factor with Dual-Labeled Bevacizumab.* Am J Nucl Med Mol Imaging, 2012. **2**(1): p. 1-13.
134. Gaykema, S.B.M., et al., *89Zr-Bevacizumab PET Imaging in Primary Breast Cancer.* Journal of Nuclear Medicine, 2013. **54**(7): p. 1014-1018.
135. Stollman, T.H., et al., *Specific imaging of VEGF-A expression with radiolabeled anti-VEGF monoclonal antibody.* International Journal of Cancer, 2008. **122**(10): p. 2310-2314.
136. Stollman, T.H., et al., *Tumor Accumulation of Radiolabeled Bevacizumab due to Targeting of Cell- and Matrix-Associated VEGF-A Isoforms.* Cancer Biotherapy & Radiopharmaceuticals, 2009. **24**(2): p. 195-200.
137. Scheer, M.G.W., et al., *Imaging liver metastases of colorectal cancer patients with radiolabelled bevacizumab: Lack of correlation with VEGF-A expression.* European Journal of Cancer, 2008. **44**(13): p. 1835-1840.
138. Nagengast, W.B., et al., *VEGF-SPECT with 111In-bevacizumab in stage III/IV melanoma patients.* European Journal of Cancer, 2011. **47**(10): p. 1595-1602.
139. Hnatowich, D.J., et al., *The preparation of DTPA-coupled antibodies radiolabeled with metallic radionuclides: an improved method.* Journal of Immunological Methods, 1983. **65**(1-2): p. 147-157.
140. Esteban, J.M., et al., *New Method for the Chelation of Indium-111 to Monoclonal Antibodies: Biodistribution and Imaging of Athymic Mice Bearing Human Colon Carcinoma Xenografts.* J Nucl Med, 1987. **28**(5): p. 861-870.

141. Mirzadeh, S., et al., *Radiometal labeling of immunoproteins: covalent linkage of 2-(4-isothiocyanatobenzyl)diethylenetriaminepentaacetic acid ligands to immunoglobulin.* Bioconjugate Chemistry, 1990. **1**(1): p. 59-65.
142. Hagan, P.L., et al., *Tumor Size: Effect on Monoclonal Antibody Uptake in Tumor Models.* Journal of Nuclear Medicine, 1986. **27**(3): p. 422-427.
143. Williams, L.E., et al., *Tumor Uptake as a Function of Tumor Mass: A Mathematic Model.* Journal of Nuclear Medicine, 1988. **29**(1): p. 103-109.
144. Haseman, M.K., S.A. Rosenthal, and T.J. Polascik, *Capromab Pendetide imaging of prostate cancer.* Cancer Biother Radiopharm, 2000. **15**(2): p. 131-40.
145. Desar, I.M.E., et al., *111In-Bevacizumab Imaging of Renal Cell Cancer and Evaluation of Neoadjuvant Treatment with the Vascular Endothelial Growth Factor Receptor Inhibitor Sorafenib.* Journal of Nuclear Medicine, 2010. **51**(11): p. 1707-1715.
146. Guo, W. and F.G. Giancotti, *Integrin signalling during tumour progression.* Nat Rev Mol Cell Biol, 2004. **5**(10): p. 816-826.
147. Lu, X., et al., *The role of integrins in cancer and the development of anti-integrin therapeutic agents for cancer therapy.* Perspect Medicin Chem, 2008. **2**: p. 57-73.
148. Horton, M.A., *The [alpha]v[beta]3 integrin "vitronectin receptor".* The International Journal of Biochemistry & Cell Biology, 1997. **29**(5): p. 721-725.
149. Friedlander, M., et al., *Definition of Two Angiogenic Pathways by Distinct alpha v integrins.* Science, 1995. **270**(5241): p. 1500-1502.
150. Eliceiri, B.P., et al., *Integrin αvβ3 Requirement for Sustained Mitogen-activated Protein Kinase Activity during Angiogenesis.* The Journal of Cell Biology, 1998. **140**(5): p. 1255-1263.
151. De, S., et al., *VEGF–integrin interplay controls tumor growth and vascularization.* Proceedings of the National Academy of Sciences of the United States of America, 2005. **102**(21): p. 7589-7594.
152. Robinson, S.D., et al., *Beta 3-Integrin Regulates Vascular Endothelial Growth Factor-A-Dependent Permeability.* Arterioscler Thromb Vasc Biol, 2004. **24**(11): p. 2108-2114.
153. Bello, L., et al., *[alpha]v[beta]3 and [alpha]v[beta]5 Integrin Expression in Glioma Periphery.* Neurosurgery, 2001. **49**(2): p. 380-390.
154. Albelda, S.M., et al., *Integrin Distribution in Malignant Melanoma: Association of the β3 Subunit with Tumor Progression.* Cancer Research, 1990. **50**(20): p. 6757-6764.
155. Rabb, H., et al., *Alpha-V/Beta-3 and Alpha-V/Beta-5 Integrin Distribution in Neoplastic Kidney.* American Journal of Nephrology, 1996. **16**(5): p. 402-408.
156. Felding-Habermann, B., et al., *Involvement of tumor cell integrin αvβ3 in hematogenous metastasis of human melanoma cells.* Clinical and Experimental Metastasis, 2002. **19**(5): p. 427-436.
157. Pierschbacher, M.D. and E. Ruoslahti, *Variants of the cell recognition site of fibronectin that retain attachment-promoting activity.* Proc Natl Acad Sci U S A, 1984. **81**(19): p. 5985-8.
158. Gould, R.J., et al., *Disintegrins: a family of integrin inhibitory proteins from viper venoms.* Proc Soc Exp Biol Med, 1990. **195**(2): p. 168-71.
159. Ruoslahti, E. and M.D. Pierschbacher, *Arg-Gly-Asp: a versatile cell recognition signal.* Cell, 1986. **44**(4): p. 517-8.
160. Mas-Moruno, C., F. Rechenmacher, and H. Kessler, *Cilengitide: the first anti-angiogenic small molecule drug candidate design, synthesis and clinical evaluation.* Anticancer Agents Med Chem, 2010. **10**(10): p. 753-68.
161. Aumailley, M., et al., *Arg-Gly-Asp constrained within cyclic pentapoptides Strong and selective inhibitors of cell adhesion to vitronectin and laminin fragment P1.* FEBS Letters, 1991. **291**(1): p. 50-54.

162. Haubner, R., et al., *[18F]Galacto-RGD: Synthesis, Radiolabeling, Metabolic Stability, and Radiation Dose Estimates.* Bioconjugate Chemistry, 2003. **15**(1): p. 61-69.
163. Haubner, R., et al., *Glycosylated RGD-containing peptides: tracer for tumor targeting and angiogenesis imaging with improved biokinetics.* J Nucl Med, 2001. **42**(2): p. 326-36.
164. Haubner, R., et al., *Noninvasive Imaging of αvβ3 Integrin Expression Using 18F-labeled RGD-containing Glycopeptide and Positron Emission Tomography.* Cancer Research, 2001. **61**(5): p. 1781-1785.
165. Beer, A.J., et al., *[18F]Galacto-RGD Positron Emission Tomography for Imaging of αvβ3 Expression on the Neovasculature in Patients with Squamous Cell Carcinoma of the Head and Neck.* Clinical Cancer Research, 2007. **13**(22): p. 6610-6616.
166. Schnell, O., et al., *Imaging of integrin alpha(v)beta(3) expression in patients with malignant glioma by [18F] Galacto-RGD positron emission tomography.* Neuro Oncol, 2009. **11**(6): p. 861-70.
167. Beer, A.J., et al., *Patterns of αvβ3 Expression in Primary and Metastatic Human Breast Cancer as Shown by 18F-Galacto-RGD PET.* Journal of Nuclear Medicine, 2008. **49**(2): p. 255-259.
168. Cho, H.J., et al., *First in human evaluation of a newly developed integrin binding PET tracer, 18F-RGD-K5 in patients with breast cancer: Comparison with 18F-FDG uptake pattern and microvessel density.* J NUCL MED MEETING ABSTRACTS, 2009. **50**(2_MeetingAbstracts): p. 1910-.
169. Indrevoll, B., et al., *NC-100717: A versatile RGD peptide scaffold for angiogenesis imaging.* Bioorganic & Medicinal Chemistry Letters, 2006. **16**(24): p. 6190-6193.
170. Roed, L., et al., *Metabolism in rats of NC100692, an RGD-peptide for imaging of angiogenesis.* Journal of Pharmaceutical and Biomedical Analysis, 2008. **47**(1): p. 164-169.
171. Lindsey, M.L., et al., *Matrix metalloproteinase-9 gene deletion facilitates angiogenesis after myocardial infarction.* Am J Physiol Heart Circ Physiol, 2006. **290**(1): p. H232-239.
172. Dobrucki, L.W., et al., *Analysis of angiogenesis induced by local IGF-1 expression after myocardial infarction using microSPECT-CT imaging.* Journal of Molecular and Cellular Cardiology, 2010. **48**(6): p. 1071-1079.
173. Hua, J., et al., *Noninvasive Imaging of Angiogenesis With a 99mTc-Labeled Peptide Targeted at $\alpha v\beta 3$ Integrin After Murine Hindlimb Ischemia.* Circulation, 2005. **111**(24): p. 3255-3260.
174. Bach-Gansmo, T., et al., *Integrin Receptor Imaging of Breast Cancer: A Proof-of-Concept Study to Evaluate 99mTc-NC100692.* J Nucl Med, 2006. **47**(9): p. 1434-1439.
175. Bach-Gansmo, T., T.V. Bogsrud, and A. Skretting, *Integrin scintimammography using a dedicated breast imaging, solid-state gamma-camera and (99m)Tc-labelled NC100692.* Clin Physiol Funct Imaging, 2008. **28**(4): p. 235-9.
176. Stewart, M., et al., *The angiogenic receptor KDR is widely distributed in human tissues and tumours and relocates intracellularly on phosphorylation. An immunohistochemical study.* Histopathology, 2003. **43**(1): p. 33-39.
177. Koukourakis, M.I., et al., *Vascular Endothelial Growth Factor/KDR Activated Microvessel Density versus CD31 Standard Microvessel Density in Non-Small Cell Lung Cancer.* Cancer Research, 2000. **60**(11): p. 3088-3095.
178. Giatromanolaki, A., E. Sivridis, and M.I. Koukourakis, *Tumour angiogenesis: vascular growth and survival.* APMIS, 2004. **112**(7-8): p. 431-440.
179. Giatromanolaki, A., et al., *Differential assessment of angiogenic activity and of vascular survival ability (VSA) in breast cancer.* Clinical and Experimental Metastasis, 2002. **19**(8): p. 673-679.
180. Giatromanolaki, A., et al., *Phosphorylated KDR expression in endometrial cancer cells relates to HIF1alpha/VEGF pathway and unfavourable prognosis.* Mod Pathol, 2006. **19**(5): p. 701-707.

181. Giatromanolaki, A., et al., *Phosphorylated VEGFR2/KDR receptors are widely expressed in B-cell non-Hodgkin's lymphomas and correlate with hypoxia inducible factor activation.* Hematological Oncology, 2008. **26**(4): p. 219-224.
182. Koukourakis, M.I., et al., *Serum VEGF levels and tissue activation of VEGFR2/KDR receptors in patients with breast and gynecologic cancer.* Cytokine, 2011. **53**(3): p. 370-375.
183. Therasse, P., et al., *New Guidelines to Evaluate the Response to Treatment in Solid Tumors.* Journal of the National Cancer Institute, 2000. **92**(3): p. 205-216.
184. Eisenhauer, E.A., et al., *New response evaluation criteria in solid tumours: Revised RECIST guideline (version 1.1).* European Journal of Cancer, 2009. **45**(2): p. 228-247.
185. Benjamin, R.S., et al., *We Should Desist Using RECIST, at Least in GIST.* Journal of Clinical Oncology, 2007. **25**(13): p. 1760-1764.
186. Forner, A., et al., *Evaluation of tumor response after locoregional therapies in hepatocellular carcinoma.* Cancer, 2009. **115**(3): p. 616-623.
187. Llovet, J.M., et al., *Sorafenib in advanced hepatocellular carcinoma.* N Engl J Med, 2008. **359**(4): p. 378-90.
188. Michaelis, L.C. and M.J. Ratain, *Measuring response in a post-RECIST world: from black and white to shades of grey.* Nat Rev Cancer, 2006. **6**(5): p. 409-414.
189. Oxnard, G.R., et al., *Variability of Lung Tumor Measurements on Repeat Computed Tomography Scans Taken Within 15 Minutes.* Journal of Clinical Oncology, 2011. **29**(23): p. 3114-3119.
190. Erasmus, J.J., et al., *Interobserver and Intraobserver Variability in Measurement of Non–Small-Cell Carcinoma Lung Lesions: Implications for Assessment of Tumor Response.* Journal of Clinical Oncology, 2003. **21**(13): p. 2574-2582.
191. Hopper KD, K.C., Van Slyke MA, Schwartz TA, TenHave TR, Jozefiak JA, *Analysis of interobserver and intraobserver variability in CT tumor measurements.* American Journal of Roentgenology, 1996. **167**(4): p. 851-854.
192. Karrison, T.G., et al., *Design of Phase II Cancer Trials Using a Continuous Endpoint of Change in Tumor Size: Application to a Study of Sorafenib and Erlotinib in Non–Small-Cell Lung Cancer.* Journal of the National Cancer Institute, 2007. **99**(19): p. 1455-1461.
193. Hutchings, M. and S.F. Barrington, *PET/CT for therapy response assessment in lymphoma.* J Nucl Med, 2009. **50 Suppl 1**: p. 21S-30S.
194. Hicks, R.J., *Role of 18F-FDG PET in assessment of response in non-small cell lung cancer.* J Nucl Med, 2009. **50 Suppl 1**: p. 31S-42S.
195. de Geus-Oei, L.F., et al., *Monitoring and predicting response to therapy with 18F-FDG PET in colorectal cancer: a systematic review.* J Nucl Med, 2009. **50 Suppl 1**: p. 43S-54S.
196. Avril, N., S. Sassen, and R. Roylance, *Response to therapy in breast cancer.* J Nucl Med, 2009. **50 Suppl 1**: p. 55S-63S.
197. Haberkorn, U., et al., *Glucose Uptake, Perfusion, and Cell Proliferation in Head and Neck Tumors: Relation of Positron Emission Tomography to Flow Cytometry.* Journal of Nuclear Medicine, 1991. **32**(8): p. 1548-1555.
198. Higashi, K., A.C. Clavo, and R.L. Wahl, *Does FDG Uptake Measure Proliferative Activity of Human Cancer Cells? In Vitro Comparison with DNA Flow Cytometry and Tritiated Thymidine Uptake.* Journal of Nuclear Medicine, 1993. **34**(3): p. 414-419.
199. Wahl, R.L., et al., *From RECIST to PERCIST: Evolving Considerations for PET Response Criteria in Solid Tumors.* J Nucl Med, 2009. **50**(Suppl_1): p. 122S-150.
200. Jahangiri, A. and M.K. Aghi, *Biomarkers predicting tumor response and evasion to anti-angiogenic therapy.* Biochimica et Biophysica Acta (BBA) - Reviews on Cancer, 2012. **1825**(1): p. 86-100.

201. Groves, A., et al., *^{18}F-FDG PET and biomarkers for tumour angiogenesis in early breast cancer.* European Journal of Nuclear Medicine and Molecular Imaging, 2011. **38**(1): p. 46-52.
202. Goh, V., et al., *The Flow–Metabolic Phenotype of Primary Colorectal Cancer: Assessment by Integrated 18F-FDG PET/Perfusion CT with Histopathologic Correlation.* Journal of Nuclear Medicine, 2012. **53**(5): p. 687-692.
203. Kaira, K., et al., *Correlation Between 18F-FDG Uptake on PET and Molecular Biology in Metastatic Pulmonary Tumors.* Journal of Nuclear Medicine, 2011. **52**(5): p. 705-711.
204. Nakamura, M., et al., *Increased glucose metabolism by FDG-PET correlates with reduced tumor angiogenesis in oral squamous cell carcinoma.* Odontology, 2012. **100**(1): p. 87-94.
205. Cochet, A., et al., *Evaluation of Breast Tumor Blood Flow with Dynamic First-Pass 18F-FDG PET/CT: Comparison with Angiogenesis Markers and Prognostic Factors.* Journal of Nuclear Medicine, 2012. **53**(4): p. 512-520.
206. Gu, J., et al., *Dynamic contrast-enhanced MRI of primary rectal cancer: quantitative correlation with positron emission tomography/computed tomography.* J Magn Reson Imaging, 2011. **33**(2): p. 340-7.
207. de Langen, A.J., et al., *Monitoring Response to Antiangiogenic Therapy in Non–Small Cell Lung Cancer Using Imaging Markers Derived from PET and Dynamic Contrast-Enhanced MRI.* Journal of Nuclear Medicine, 2011. **52**(1): p. 48-55.
208. Zhu, A.X., et al., *Efficacy and safety of gemcitabine, oxaliplatin, and bevacizumab in advanced biliary-tract cancers and correlation of changes in 18-fluorodeoxyglucose PET with clinical outcome: a phase 2 study.* The Lancet Oncology, 2010. **11**(1): p. 48-54.
209. Mitchell, C.L., et al., *A two-part phase II study of cediranib in patients with advanced solid tumours: the effect of food on single-dose pharmacokinetics and an evaluation of safety, efficacy and imaging pharmacodynamics.* Cancer Chemother Pharmacol, 2011. **68**(3): p. 631-41.
210. Kelly, R.J., et al., *Evaluation of KRAS mutations, angiogenic biomarkers, and DCE-MRI in patients with advanced non-small-cell lung cancer receiving sorafenib.* Clin Cancer Res, 2011. **17**(5): p. 1190-9.
211. O'Connor, J.P.B., et al., *Dynamic contrast-enhanced MRI in clinical trials of antivascular therapies.* Nat Rev Clin Oncol, 2012. **9**(3): p. 167-177.
212. Morgan, B., et al., *Dynamic Contrast-Enhanced Magnetic Resonance Imaging As a Biomarker for the Pharmacological Response of PTK787/ZK 222584, an Inhibitor of the Vascular Endothelial Growth Factor Receptor Tyrosine Kinases, in Patients With Advanced Colorectal Cancer and Liver Metastases: Results From Two Phase I Studies.* Journal of Clinical Oncology, 2003. **21**(21): p. 3955-3964.
213. Hecht, J.R., et al., *Randomized, Placebo-Controlled, Phase III Study of First-Line Oxaliplatin-Based Chemotherapy Plus PTK787/ZK 222584, an Oral Vascular Endothelial Growth Factor Receptor Inhibitor, in Patients With Metastatic Colorectal Adenocarcinoma.* Journal of Clinical Oncology, 2011. **29**(15): p. 1997-2003.
214. O'Connor, J.P.B., et al., *DCE-MRI biomarkers in the clinical evaluation of antiangiogenic and vascular disrupting agents.* Br J Cancer, 2007. **96**(2): p. 189-195.
215. Padhani, A.R., et al., *Prediction of clinicopathologic response of breast cancer to primary chemotherapy at contrast-enhanced MR imaging: initial clinical results.* Radiology, 2006. **239**(2): p. 361-74.
216. Zweifel, M. and A. Padhani, *Perfusion MRI in the early clinical development of antivascular drugs: decorations or decision making tools?* European Journal of Nuclear Medicine and Molecular Imaging, 2010. **37**(0): p. 164-182.
217. Overmoyer, B., et al., *Inflammatory breast cancer as a model disease to study tumor angiogenesis: results of a phase IB trial of combination SU5416 and doxorubicin.* Clin Cancer Res, 2007. **13**(19): p. 5862-8.

218. Hsu, C.-Y., et al., *Dynamic contrast-enhanced magnetic resonance imaging biomarkers predict survival and response in hepatocellular carcinoma patients treated with sorafenib and metronomic tegafur/uracil.* Journal of Hepatology, 2011. **55**(4): p. 858-865.
219. Goh, V., et al., *Can perfusion CT assessment of primary colorectal adenocarcinoma blood flow at staging predict for subsequent metastatic disease? A pilot study.* European Radiology, 2009. **19**(1): p. 79-89.
220. Fournier, L.S., et al., *Metastatic Renal Carcinoma: Evaluation of Antiangiogenic Therapy with Dynamic Contrast-enhanced CT.* Radiology, 2010. **256**(2): p. 511-518.
221. Ng, C.S., et al., *Perfusion CT Findings in Patients With Metastatic Carcinoid Tumors Undergoing Bevacizumab and Interferon Therapy.* American Journal of Roentgenology, 2011. **196**(3): p. 569-576.
222. Wang, J., et al., *Tumor Response in Patients With Advanced Non–Small Cell Lung Cancer: Perfusion CT Evaluation of Chemotherapy and Radiation Therapy.* American Journal of Roentgenology, 2009. **193**(4): p. 1090-1096.
223. Ng, Q.S. and V. Goh, *Angiogenesis in Non-small Cell Lung Cancer: Imaging With Perfusion Computed Tomography.* Journal of Thoracic Imaging, 2010. **25**(2): p. 142-150 10.1097/RTI.0b013e3181d29ccf.
224. Morrison, M.S., et al., *Use of a Novel Arg-Gly-Asp Radioligand, 18F-AH111585, to Determine Changes in Tumor Vascularity After Antitumor Therapy.* J Nucl Med, 2009. **50**(1): p. 116-122.
225. Jung, K.H., et al., *Favorable biokinetic and tumor-targeting properties of 99mTc-labeled glucosamino RGD and effect of paclitaxel therapy.* J Nucl Med, 2006. **47**(12): p. 2000-7.
226. Dumont, R.A., et al., *Noninvasive imaging of alphaVbeta3 function as a predictor of the antimigratory and antiproliferative effects of dasatinib.* Cancer Res, 2009. **69**(7): p. 3173-9.
227. Yang, M., et al., *PET imaging of early response to the tyrosine kinase inhibitor ZD4190.* Eur J Nucl Med Mol Imaging, 2011. **38**(7): p. 1237-47.
228. Blankenberg, F.G., et al., *Noninvasive assessment of tumor VEGF receptors in response to treatment with pazopanib: a molecular imaging study.* Transl Oncol, 2010. **3**(1): p. 56-64.
229. Levashova, Z., et al., *Molecular Imaging of Changes in the Prevalence of Vascular Endothelial Growth Factor Receptor in Sunitinib-Treated Murine Mammary Tumors.* Journal of Nuclear Medicine, 2010. **51**(6): p. 959-966.
230. Kerbel, R.S. and B.A. Kamen, *The anti-angiogenic basis of metronomic chemotherapy.* Nat Rev Cancer, 2004. **4**(6): p. 423-436.
231. Ali, M.M., et al., *Changes in Vascular Permeability and Expression of Different Angiogenic Factors Following Anti-Angiogenic Treatment in Rat Glioma.* PLoS ONE, 2010. **5**(1): p. e8727.
232. Palmowski, M., et al., *Molecular profiling of angiogenesis with targeted ultrasound imaging: early assessment of antiangiogenic therapy effects.* Molecular Cancer Therapeutics, 2008. **7**(1): p. 101-109.
233. Virostko, J., et al., *A molecular imaging paradigm to rapidly profile response to angiogenesis-directed therapy in small animals.* Mol Imaging Biol, 2009. **11**(3): p. 204-12.
234. Dixon, R.N. and C.J. Taylor, *Automated Asbestos Fiber Counting.* Machine Aided Image Analysis, Institute of Physics, London, 1979. **44**: p. 178-185.
235. Zwiggelaar, R., T.C. Parr, and C.J. Taylor, *Finding orientated line patterns in digital mammographic images.* Proc of 7th British Machine Vision Conference, 1996: p. 715-724.
236. Sonka, M., H. V., and B. R, *Image Processing, Analysis and Machine Vision.* Chapman and Hall, London, UK, 1993.
237. Huynh, H., et al., *Bevacizumab and rapamycin induce growth suppression in mouse models of hepatocellular carcinoma.* J Hepatol, 2008. **49**(1): p. 52-60.

238. Falcon, B.L., et al., *Reduced VEGF production, angiogenesis, and vascular regrowth contribute to the antitumor properties of dual mTORC1/mTORC2 inhibitors.* Cancer Res, 2011. **71**(5): p. 1573-83.
239. Shaw, R.J. and L.C. Cantley, *Ras, PI(3)K and mTOR signalling controls tumour cell growth.* Nature, 2006. **441**(7092): p. 424-430.
240. Jain, R.K., *Normalization of Tumor Vasculature: An Emerging Concept in Antiangiogenic Therapy.* Science, 2005. **307**(5706): p. 58-62.
241. Medici, D. and B.R. Olsen, *Rapamycin Inhibits Proliferation of Hemangioma Endothelial Cells by Reducing HIF-1-Dependent Expression of VEGF.* PLoS ONE, 2012. **7**(8): p. e42913.
242. Guba, M., et al., *Rapamycin inhibits primary and metastatic tumor growth by antiangiogenesis: involvement of vascular endothelial growth factor.* Nat Med, 2002. **8**(2): p. 128-35.
243. Reynolds, A.R., et al., *Elevated Flk1 (vascular endothelial growth factor receptor 2) signaling mediates enhanced angiogenesis in beta3-integrin-deficient mice.* Cancer Res, 2004. **64**(23): p. 8643-50.
244. Folkman, J., *Angiogenesis in cancer, vascular, rheumatoid and other disease.* Nat Med, 1995. **1**(1): p. 27-30.
245. Hanahan, D. and R.A. Weinberg, *The Hallmarks of Cancer.* Cell, 2000. **100**(1): p. 57-70.
246. Demetri, G.D., et al., *Efficacy and safety of sunitinib in patients with advanced gastrointestinal stromal tumour after failure of imatinib: a randomised controlled trial.* The Lancet, 2006. **368**(9544): p. 1329-1338.
247. Duda, D.G., R.K. Jain, and C.G. Willett, *Antiangiogenics: The Potential Role of Integrating This Novel Treatment Modality With Chemoradiation for Solid Cancers.* J Clin Oncol, 2007. **25**(26): p. 4033-4042.
248. Escudier, B., et al., *Sorafenib in advanced clear-cell renal-cell carcinoma.* N Engl J Med, 2007. **356**(2): p. 125-34.
249. Hurwitz, H., et al., *Bevacizumab plus Irinotecan, Fluorouracil, and Leucovorin for Metastatic Colorectal Cancer.* The New England Journal of Medicine, 2004. **350**(23): p. 2335-2342.
250. Motzer, R.J., et al., *Sunitinib versus Interferon Alfa in Metastatic Renal-Cell Carcinoma.* N Engl J Med, 2007. **356**(2): p. 115-124.
251. Sandler, A., et al., *Paclitaxel-Carboplatin Alone or with Bevacizumab for Non-Small-Cell Lung Cancer.* N Engl J Med, 2006. **355**(24): p. 2542-2550.
252. Shojaei, F. and N. Ferrara, *Role of the microenvironment in tumor growth and in refractoriness/resistance to anti-angiogenic therapies.* Drug Resist Updat, 2008. **11**(6): p. 219-30.
253. Jain, R.K., et al., *Lessons from phase III clinical trials on anti-VEGF therapy for cancer.* Nature clinical practice. Oncology, 2006. **3**(1): p. 24-40.
254. Burris, H., 3rd and C. Rocha-Lima, *New therapeutic directions for advanced pancreatic cancer: targeting the epidermal growth factor and vascular endothelial growth factor pathways.* Oncologist, 2008. **13**(3): p. 289-98.
255. Bergers, G. and D. Hanahan, *Modes of resistance to anti-angiogenic therapy.* Nat Rev Cancer, 2008. **8**(8): p. 592-603.
256. Kerbel, R.S., *Tumor angiogenesis.* N Engl J Med, 2008. **358**(19): p. 2039-49.
257. Banerjee, S., et al., *Mechanisms of disease: angiogenesis and the management of breast cancer.* Nature clinical practice. Oncology, 2007. **4**(9): p. 536-50.
258. Quesada, A.R., M.A. Medina, and E. Alba, *Playing only one instrument may be not enough: limitations and future of the antiangiogenic treatment of cancer.* Bioessays, 2007. **29**(11): p. 1159-68.
259. Stumpp, M.T., H.K. Binz, and P. Amstutz, *DARPins: A new generation of protein therapeutics.* Drug Discovery Today, 2008. **13**(15–16): p. 695-701.

260. Tolmachev, V., et al., *Affibody molecules: potential for in vivo imaging of molecular targets for cancer therapy.* Expert Opinion on Biological Therapy, 2007. **7**(4): p. 555-568.
261. Morrison, M.S., et al., *Use of a novel Arg-Gly-Asp radioligand, 18F-AH111585, to determine changes in tumor vascularity after antitumor therapy.* J Nucl Med, 2009. **50**(1): p. 116-22.
262. Ferrara, N. and T. Davis-Smyth, *The Biology of Vascular Endothelial Growth Factor.* Endocrine Reviews, 1997. **18**(1): p. 4-25.

Appendix B: Clinical Trials

Below are the synopses from the protocols of the clinical trials mentioned in the thesis.

5.5 Maraciclatide Trial Protocol

The full clinical trial protocol, patient information sheet and clinical trial protocol can be found on the attached CD.

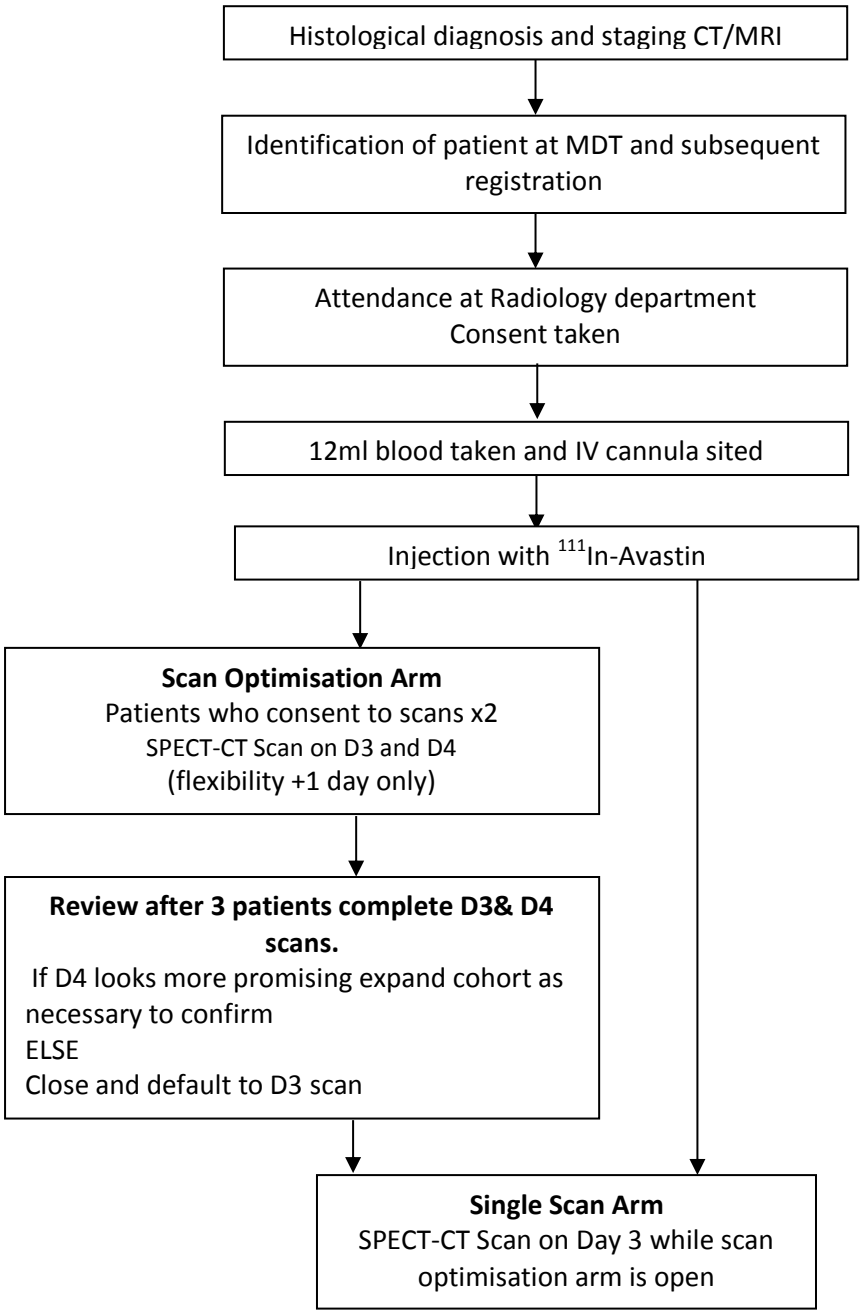
Title of study:	A Comparative Study of Quantifying Angiogenesis in Solid Tumour by Immuno-histochemical analysis, DCE-MRI and SPECT.
Short Title	Imaging of angiogenesis in cancer
Principal Investigator	Professor Fergus Gleeson
Sponsor	Oxford University Hospitals NHS Trust
REC number	08/H0606/57
Scientific rationale	The $\alpha_v\beta_3$ integrin is expressed preferentially by proliferating endothelial cells. The SPECT-CT ligand specific for $\alpha_v\beta_3$ should therefore highlight those areas of the undergoing active angiogenesis. There should be correlation between angiogenic tumour tissue as seen on the SPECT image and the tissue markers of angiogenesis on immunohistochemical analysis. The SPECT results should also correlate with our presently used imaging technique for angiogenesis (DCE-MRI).
Clinical rationale	SPECT-CT with radio-labelled RGD ligand with specificity for $\alpha_v\beta_3$ integrin could be used as an indirect method of measuring tumour angiogenesis. This may allow us to select patients who will most benefit from anti-angiogenic agents and also to act as an early tool for assessment of response.
Primary endpoint	To determine whether an imaging technique, SPECT–CT with a radioisotope marker which binds to the activated endothelial cells characteristic of tumour associated angiogenesis, correlates with immunohistochemical markers of angiogenesis.
Secondary endpoint	To compare SPECT-CT with a radio-isotope marker to dynamic contrast enhanced MRI, which is the current imaging modality used to assess tumour microvasculature
Study design	This is a single centre, open label, single arm pilot study.
Patient numbers	Approximately 60.
Target population	Approximately 60 patients with early or late stage colorectal cancer or early stage renal cancer or breast cancer who are due to undergo a substantial resection of their tumour or have a core biopsy
Main eligibility/ exclusion criteria	Patients Age >18 years, who are able to give informed consent and have no contraindications to the scanning methods used
Trial treatment, dose and administration	Patients will have a DCE-MRI and a SPECT-CT using a ligand against $\alpha_v\beta_3$ integrin prior to surgery. Resected specimens will be analysed for

	microvessel density as a direct histopathological measure of angiogenesis and against other immunohistochemical and serum markers involved in the angiogenic process.
Additional procedures	Patients' treatment will be according to our standard protocols. The additional procedures are the two scans
Patient care post-study	Routine standard of care as clinically indicated.
Statistical methods	Correlation between DCE-MRI and the RGD-SPECT-CT will be assessed using Cohen's kappa coefficient. Continuous data will be summarised as median and range, and categorical data described by counts and frequencies.
Number of centres	This is a single centre trial. All patients will be recruited via the Medical Oncology department, Oxford University Hospitals NHS Trust, UK
Duration of study	Recruitment into the trial is expected to take 12 months, accruing approximately 4 patients per month. Analysis of data will take place following this and is anticipated to take a further 18 months.
End of study	First anniversary of the Last Patient Last Visit to allow completion of laboratory assays.

5.6 VEGF Imaging with ^{111}In-bnDTPA-Bevacizumab

Study Title	Evaluation of Radiolabelled Bevacizumab to Assess VEGF Expression in Primary and Secondary Deposits of Cancer
Short Title	VEGF Imaging
Principal Investigator	Professor Adrian L Harris
Sponsor	R&D Department, Oxford University Hospitals NHS Trust
Scientific Rationale	Tumour angiogenesis is dependent on the production and effects of vascular endothelial growth factor (VEGF). Bevacizumab is a monoclonal antibody that specifically binds and inhibits the function of VEGF. Radiolabelling bevacizumab with ^{111}Indium should allow visualisation of regions of VEGF production and tumour angiogenesis using single-photon emission computed tomography (SPECT).
Clinical Rationale	If radiolabelled bevacizumab is shown to successfully localise areas of tumour VEGF expression it may be used as a method of patient stratification and monitoring of therapy in trials of drugs that modulate VEGF signalling and expression, to help with therapeutic decisions in the future. It may allow the selection of patients most likely to benefit from anti-angiogenic agents and also to act as a tool for assessment of induction of VEGF in hypoxia or suppression by signalling blockers e.g. mTOR inhibitors. Such a tool is important to develop to optimise use of antiangiogenic therapies
Primary Objectives	Assess the ability to visualise tumour primary site and metastases by comparison with CT and MRI detected lesions
Secondary Objective	To determine the optimum time point for VEGF imaging
Exploratory Objectives	Comparison of uptake on scan with plasma markers of angiogenesis
Study Design	Single centre, open-label, single arm pilot study
Target Population	Patients diagnosed with at least 1 solid primary or metastatic tumour including (but not limited to) lung cancer, renal cancer, melanoma and breast cancers

Number of Participants	25-30
Planned Study Period	6 months
Inclusion Criteria	Primary or metastatic solid cancer Tumour lesions ≥ 2cm demonstrable by CT or MRI scan Aged ≥18 years ECOG performance status ≤ 2 Adequate renal (creatinine <1.25x ULN), liver (bilirubin <2 x ULN; transaminases <5 x ULN) and haematological (neutrophils ≥1.5x10^9/L; haemoglobin ≥ 9 g/dL; platelets ≥ 150x10^9/L) function Normal cardiac function clinically Competency and willingness to give informed consent Ability to comply with study protocol and follow-up schedule The patient has undergone/will undergo a diagnostic CT or MRI within 2 weeks of the VEGF imaging scan without intervening therapy



5.7 Fluciclatide, Pre and Post Therapy Study

Title of study:	Prospective study of 18F-RGD PET in assessment of response to antiangiogenic treatment in patients with renal cancer and comparison with perfusion CT
Short Title	RGD-PET in RCC therapy
Chief Investigator	Professor Fergus Gleeson
Sponsor	Oxford University Hospitals NHS Trust
Scientific rationale	The $\alpha_v\beta_3$ integrin is expressed preferentially by proliferating endothelial cells within angiogenesis. The PET-CT ligand fluciclatide (a fluorinated RGD molecule) binds to $\alpha_v\beta_3$ integrin thus is an imaging agent capable of demonstrating regions of active angiogenesis. Using PET-CT scanning, uptake of the tracer within tumours and organs can be quantified and therefore be used as a measure of angiogenesis
Clinical rationale	If changes in uptake correlate with the response of tumours to anti-angiogenic agents, then it would allow better patient selection for such therapies and provide a tool for assessment of response. In addition quantification of angiogenesis via such agents may allow: • Titration of dosage, and determination of length of chemotherapeutic regimen. • Monitor drug effects – surrogate end-points for phase I and II trials • Identifying resistance to therapy • Translational research
Primary objective	To evaluate whether changes of uptake on ^{18}F-RGD PET post anti-angiogenic therapy are associated with tumour response in patients with cancer
Secondary objective	Assess the safety profile of fluciclatide in this patient population To evaluate whether changes of perfusion CT parameters are associated with response To see if changes in perfusion CT parameters correlate with changes on ^{18}F-RGD PET Evaluation of whether changes of uptake on ^{18}F-RGD PET post anti-angiogenic therapy are associated with tumour response between individual lesions Evaluation of whether changes of uptake on ^{18}F-RGD PET post anti-angiogenic therapy are associated with clinical outcome
Study design	This is an open label study
Patient numbers	40-50 in total
Target population	Patients with a histological confirmed diagnosis of advanced RCC deemed suitable for anti-angiogenic treatment.
Inclusion criteria	Patients with advanced or metastatic RCC confirmed by histological diagnosis Patient considered suitable for TKI therapy Measurable tumour according to RECIST v1.1 criteria Standard staging CT scan performed within 28 days prior to registration The patient has not received chemotherapy, radiotherapy, surgery or any other treatment against cancer within 4 weeks prior to first research scan. Age ≥18 years Adequate renal function (creatinine <1.25xULN)

	Patient is able to tolerate and comply with scanning procedure Patient is not lactating or pregnant Absence of any psychological, familial, sociological or geographical condition which in the opinion of the Investigator may potentially hamper compliance with the study protocol and follow-up schedule; those conditions should be discussed with the patient before registration in the trial Able and willing to provide informed consent
Trial interventions	Patients will have a 18F-RGD-PET-CT and a perfusion-CT prior to antiangiogenic therapy. They will have a repeat set of scans after 4 weeks of therapy. A further 18F-RDG-PET-CT and perfusion-CT will be performed at the time of the second routine staging CT.
Patient care post-trial:	Standard of care
Duration on study:	Patients will be followed for progression free and overall survival for 12 months after their final study visit for the second set of research scans. Hence duration on study will be approximately 16 months.
End of study	Last Patient Off Study
Statistical methods	Correlation between change in uptake and response will be assessed using a Pearson's correlation coefficient.